Dielectric metasurfaces for light management in photovoltaics

Ph. D. Thesis, University of Amsterdam, March 2021
Dielectric metasurfaces for light management in photovoltaics
Verena Neder

Cover: Schematic of spectral splitting by metasurface as descriped in chapter 8

ISBN 978-94-92323-50-7

The work described in this thesis was performed at AMOLF,
Science Park 104, 1098 XG Amsterdam, The Netherlands.

This work is part of the Dutch Research Council (NWO).

A digital version of this thesis can be downloaded from
`https://ir.amolf.nl/`.

Dielectric metasurfaces for light management in photovoltaics

ACADEMISCH PROEFSCHRIFT

ter verkrijging van de graad van doctor
aan de Universiteit van Amsterdam
op gezag van de Rector Magnificus
prof. dr. ir. K.I.J. Maex
ten overstaan van een door het College voor Promoties ingestelde commissie,
in het openbaar te verdedigen in de Agnietenkapel
op donderdag 25 maart 2021, te 13.00 uur

door Verena Neder

geboren te Schweinfurt

Promotiecommissie

Promotores:	prof. dr. A. Polman	Universiteit van Amsterdam
	prof. dr. A. Alù	The City University of New York
Overige leden:	prof. dr. P. Schall	Universiteit van Amsterdam
	dr. K. Newell	Universiteit van Amsterdam
	prof. dr. W. C. Sinke	Universiteit van Amsterdam
	dr. E. Alarcón Lladó	AMOLF
	prof. dr. A. W. Weeber	Technische Universiteit Delft

Faculteit der Natuurwetenschappen, Wiskunde en Informatica

Contents

1

Introduction

Wie viel Seiten hat ein unbeschriebenes Blatt?
Um wie viel Ecken muss man denken, damit das was man vorhat klappt?

Dort wo du wohnst – Clueso

1.1. Future goals for photovoltaics

As part of reaching the goals of the Paris agreement the European Union (EU) has guaranteed to reduce its greenhouse gas (GHG) emissions into the atmosphere by at least 40% by 2030 and 80% by 2050 compared to 1990 levels [1]. One important step in the planning towards this goal is the stepwise change to renewable energy sources for electricity production, with photovoltaics (PV) being one of the main technology options. To reach the goal of 100% carbon-free electricity production the installed PV capacity in the EU must grow from 117 GW_p in 2019 to at least 630 GW_p by 2025 and 1.94 TW_p by 2050 [2]. The future electricity demand is an important factor and uncertainty in these numbers. Figure 1.1 shows the actual and estimated installed PV power between 2010 and 2030 for different scenarios of the EUs long-term strategy on reducing GHG. If the growth in electricity demand is just 10% above the expectations in the EU scenarios the demand for installed PV power in 2030 would more than double to around 1.2 TW_p [3].

One challenge encountered in the expansion of PV capacity is the demand for area to install the solar panels on. It is important to develop strategies to increase PV capacity while balancing the need for land for nature and agriculture, for avoiding conflicts between the demand of area and societal acceptance of growth of PV capacity. Great effort is being made to find innovative ways of integrating PV into existing infrastructure as buildings, urban environments, roads, in agriculture or on vehicles [4]. For example in the Netherlands and Germany, 400 km^2 and 2.800 km^2 area of rooftops are potentially usable for photovoltaics. Those areas have a capacity of 66 GW_p and 500 GW_p respectively and can already provide for a big part of the required area for future PV installations [5, 6]. A key aspect of integrating PV into buildings, roads and vehicles is the design aspect of photovoltaics. Specifically, the color appearance of PV is an important parameter

1

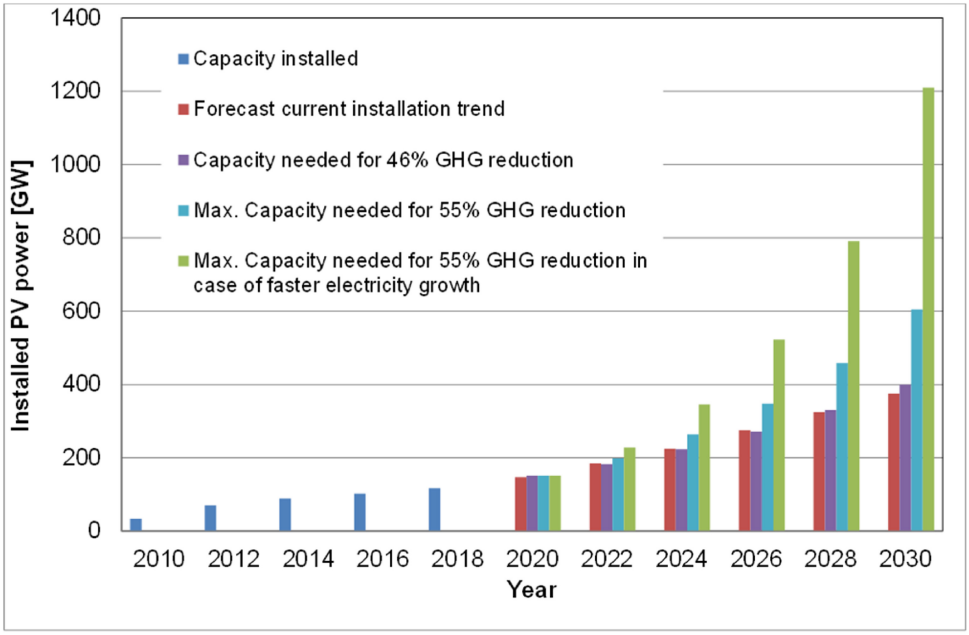

Figure 1.1: Installed and predicted installed PV power capacity in the EU from 2010 to 2030 for different scenarios of the EU's long-term strategies for 46% and 55% GHG reduction, as well as 55% GHG reduction with a faster electricity growth than expected (figure taken from [3]). (Installed PV power in GW_p; W_p is the power generated by a photovoltaic system under standardized illumination conditions.)

for designing building-integrated PV (BIPV). On the other hand a key goal in PV technology is increasing the efficiency of solar cells as that can reduce the cost per installed power. Also, higher-efficiency solar panels require less land area. To bring an example here, for the areas mentioned above for the Netherlands and Germany an increase in solar panel efficiency from 17% to 20% would save a land area of 60 km^2 in the Netherlands (size of Maastricht) and 300 km^2 in Germany (size of Munich). Therefore, increasing efficiency is one of the most followed research and development goals in PV. For Si solar cells the current efficiency record, while writing this thesis, of 26.7% [7] is already pretty close to the theoretical efficiency limit of 29.4% [8]. The technology of tandem solar cells that combine different absorber materials in one cell is a highly attractive approach to go well beyond the single-junction Si cell limit. In the past, tandem cell technologies were mostly based in III-V semiconductors that are quite expensive and were used in solar concentrator cells or for space applications [9]. In recent years perovskite solar cells have created major breakthroughs in PV research, with single-junction efficiencies now approaching those of Si solar cells. The most recent record at the time of writing this thesis for perovskite/ silicon tandem solar cells is 29.52% [10] and perovskite/silicon tandem cell efficiencies above 30% now appear well possible [11].

1.2. What nanophotonics can do for PV

The challenges mentioned in the last section require further advanced control over the management of light in the solar cells. Nanophotonic structures present an alternative technology beyond the conventional optical designs in PV, offering a strongly enhanced control over the harvesting of light [12, 13]. A key element in the application of nanophotonics in photovoltaics is the use of resonantly scattering metallic or dielectric nanoparticles with sizes in the order of the optical wavelength. Those particles can exhibit strong plasmonic or Mie resonances that are tunable by size and can therefore offer strong control over the scattering of light. Initially, the benefits of including such particles in solar cells were exploited by applying plasmonic particles for enhanced absorption in (thin film) cells [12]. Next, the benefit of dielectric particles which exhibit lower optical losses has been realized and was employed for light trapping and the creating of broadband anti-reflection coatings [14–16]. More recently, the nanophotovoltaics field evolved to the use of (periodic) arrangement of (non) resonant scatterers into metasurfaces. Those ultrathin photonic structures tailor the profile of the scattered light field so that it is optimally coupled, trapped and guided in the solar cell. Such metasurfaces are ultrathin, in the order of 100 nm, and light-weight, and can thus be easily integrated with existing solar cell designs.

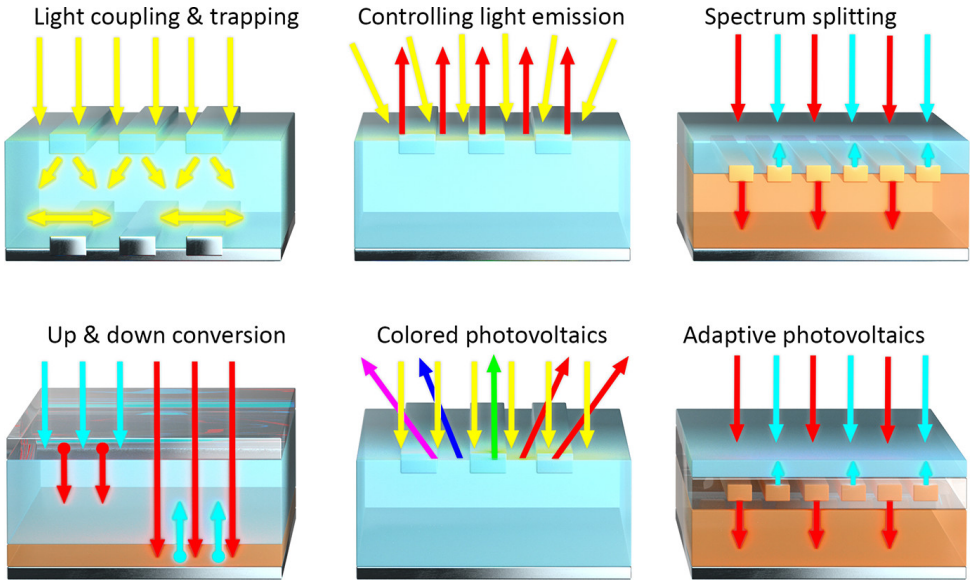

Figure 1.2: Schematics of possible functionalities of light scattering photonic structures and metasurfaces in solar cells. (Figure taken from [17])

Photonic structures have many different application possibilities in conventional single-junction cells, tandem cells, bifacial solar cells, luminescent solar concentrators and down and up conversion layers. As illustrated in Figure 1.2, they can enhance light trapping, control light emission, split the spectrum, support up and down conversion, can be used to color photovoltaics, and enable adaption of photovoltaics to e.g. the

daylight spectrum [17]. In the next two paragraphs, we will explain in more detail how nanophotonic structures can be beneficial for two specific applications: colored photovoltaics, and high-efficiency tandem solar cells.

1.3. Dielectric nanoparticles for colored PV

As mentioned above BIPV can account for a big part of the required PV capacity, but their aesthetics is a crucial factor to blend PV into building materials and rooftops. Creating colorful PV will by definition introduce losses, as light has to be deliberately reflected or emitted for creating the colorful appearance. Many different methods have been used in the past to create colorful PV. We review some of them here and compare their advantages and disadvantages in table 1.1.

We compare multilayer interference coatings, distributed Bragg reflectors, resonant plasmonic structures as well as resonant dielectric nanoscatterers for the creation of colorful PV. Table 1.1 lists the most important factors that will be discussed in the following.

Method	Color range	Optical Losses	Angular behavior	Color quality	Comments on fabrication	Reference
Multilayer interference coatings	Pure colors, but not all mixed colors	low	Strongly angle dependent	Intermediate, strong dependence on number of layers	Expensive vacuum technologies	[18]–[21]
Distributed Bragg reflectors	Pure and mixed colors	low	Relatively independent	Good, intense colors in distinct wavelength range	Expensive vacuum technology	[22], [23]
Resonant dielectric nanoscatterers	Pure and mixed colors	low	Can be controlled, specular, Lambertian or specific angle range	Good, intense colors in distinct resonance	Soft imprint technology not demonstrated at large scale; potential for low-cost solution-based process	[24]–[26]
Resonant plasmonic structures	Pure (mixed colors possible but not demonstrated)	high	stable	Good, very intense colors in distinct resonance	Sputtering and annealing, potential for low-cost solution-based process	[27]

Table 1.1: Comparison of different technologies for coloration of solar cells. Positive features are marked in green, neutral features in yellow, and negative features in orange.

The first aspect is the freedom in the choice of coloration to be able to fill the entire color space, choosing between pure colors (single wavelength band, e.g. blue, green, yellow, red) as well as being able to mix the colors (combine different wavelength bands to create e.g. pink or white) is essential. This is possible for distributed Bragg reflectors by combining several layers on top of each other as they are optically independent. In the case of resonant dielectric particles the color mixing can by tailored in a single layer by mixing nanoparticles of different size.

Next, the optical losses which directly impact the efficiency of the solar cell are an important factor but are quite difficult to compare. All techniques can be tuned to lower reflectance which will always result in lower color intensity. It is important to avoid any

unnecessary absorption, meaning that techniques based on dielectric materials are preferred over using metallic particles which suffer from parasitic absorption. Another option to avoid optical losses is to reduce the reflectance of colorful light to only the angular range that is of interest for an observer.

Another element to consider is the angular performance, describing if colors are stable under angled illumination and observation, and if the angular behavior can be designed at will. The Bragg reflectors as well as the particle-based techniques show angular stable coloration. None of the conventional techniques can control the angular behavior of the colored light that, as mentioned, would help to reduce the optical losses, and can add extra functionalities to the colored PV.

Furthermore, the quality of color depends mainly on how strong and clean a peak in reflectance can be tuned. Bragg reflectors are known for their sharp reflectance peaks. The color of multilayer coatings strongly depends on the number of layers and higher-order reflectance peaks can affect the quality of the color. The scattering spectrum of nanoparticles can be controlled to some extent to show distinct peaks.

Finally, to evaluate the fabrication procedure the cost and potential for large-scale fabrication should be discussed. The fabrication of interference coatings and Bragg reflectors is based on multiple-layer evaporation in high vacuum which is expensive, but is possible on a large-area industrial scale. For the dielectric particle based reflectors, so far lab-scale substrate conformal imprint lithography (SCIL) printing was done that may become industrially feasible for large-area fabrication for PV. Also, solution-based processes using spray coating of nanoparticles might lead to a route of inexpensive fabrication. It should be mentioned that the comparison of all technologies here is rather qualitatively because different papers use different figures of merit to describe the functionality of the respective technology. In future, a common ground to estimate the performance should be used in this field of research [28].

In summary, existing solutions to efficiently color PV still have some drawbacks . First, there is no control over the angular range, that the light is reflected to. The arrangement of dielectric nanoscatterers in metasurfaces can add this extra angle control to the colored PV. This has the advantage that the module can be applied in a very specific way, for example as rooftop PV with red light only scattering towards an observer on the street. Second, another challenge is the fabrication of structures with high-quality colors in an inexpensive, industry-compatible way. Coatings made of dielectric nanoparticles can be imprinted on the solar panel module glass, using soft conformal imprint lithography stamps in the lab, and have the potential to be fabricated with large-scale role-to-role imprint technology. In the first part of this thesis we exploit the light scattering from dielectric nanoparticles to create colorful photovoltaics and with tailored angular distribution beyond what has been realized so far.

1.4. Light management in tandem cells

Tandem solar cells have the potential to reach efficiencies well above 30%. In the two-terminal (2T) tandem geometry the two subcells are connected electrically and share the same current, while in the four-terminal (4T) case the tandem is composed of two independent cells with independent current collection circuits that are mechanically stacked on top of each other. Both configurations have their advantages and disadvantages. For

2T tandem cells the main advantage is the compact geometry that allows integration into existing module technology. The main disadvantage is that the fabrication of the cells can be quite challenging because the subcells have to be fabricated as a single stack, where subsequent fabrication steps can negatively affect the earlier-deposited layers by the use of high temperature, reactive solvents, or etching processes that introduce defects. Also, the current matching condition in 2T cells sets a restriction on the design and allows only combination of certain range of bandgaps for the top and bottom cells. In contrast, for 4T cells current matching is not required, which relaxes the flexibility and bandgap combination of top and bottom cells. In a 4T geometry the two subcells can be fabricated and optimized independently. However, the main disadvantage is that the two independent cells cannot be integrated in existing module technology and more complex wiring circuitry is needed to harvest the current in a module composed of 4T tandem cells.

In the following and overview is given of the different optical losses in 2T and 4T perovskite/silicon tandem cells and how nanophotonic concepts can be used to reduce them. Finally, we will give an outlook how such solutions are addressed in this thesis.

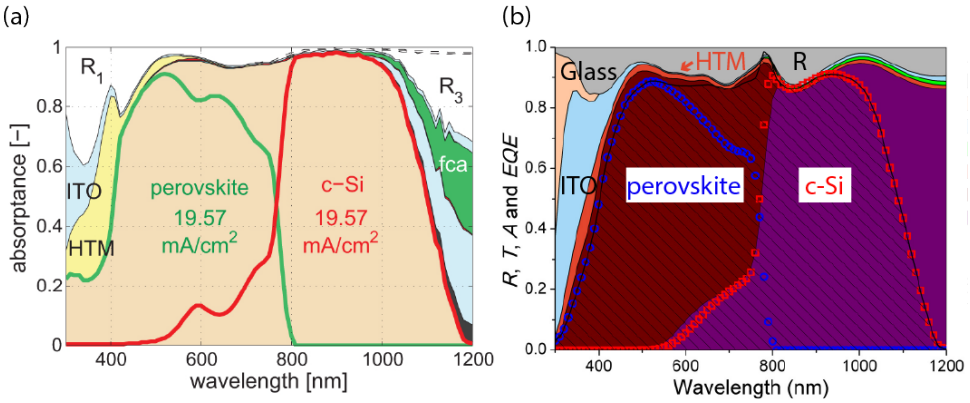

Figure 1.3: Loss analysis in 2T (left) and 4T (right) perovskite-silicon tandem solar cells, showing absorption in the sub cells with the perovskite and Si contributions indicated by the green and red curves (2T) and by the blue and red dotted curves (4T). Losses from reflectance and parasitic absorption in inactive layers of the cell are also indicated (ITO: indium-tin-oxide transparent contacts, HTM: hole/electron transport layers; FCA: free carrier absorption; R,$R_{1,3}$: reflection from perovskite and Si cell. From Refs. [29, 30]; additional labels added in (b).

For both 2T and 4T perovskite-silicon tandem cells proper light management is a critical factor to optimize the efficiency. The main optical losses are reflectance, parasitic absorption in inactive layers of the cell and non-ideal redistribution of spectral bands between the subcells [31, 32]. As an example, Figure 1.3 shows an analysis of the optical losses in a simulated 2T perovskite-silicon tandem cell [29] (J_{sc} = 39.1 mA/cm^2) and an experimental high-efficiency 4T tandem cell (η = 25.7%, J_{sc} = 36.5 mA/cm^2) [30]. In both cases, the perovskite top cells are flat and the silicon bottom cells have a textured front. Both images show the absorption in the tandem sub cells.

For both cells the same trends can be observed. First, reflectance induces losses of

several mA/cm^2. Reflection of light occurs at the perovskite top surface, the interlayers and the silicon back surface. For the perovskite top cell, usually, a thin-film anti-reflection (AR) coating is applied. This could be replaced by a nanostructure layer that further reduces reflectance and couples light into the perovskite cell [15, 33, 34]. Texturing of the perovskite by applying perovskite directly on top of the textured silicon is still quite challenging (but has been recently demonstrated [35]). In the 2T example of Figure 1.3a, a barrier layer to planarize the silicon before applying the perovskite cell is modelled. In both 2T and 4T designs an interlayer in between the cells can be used to reduce reflectance from this part of the cell. In the 2T cell this requires integration with the intermediate carrier-selective contacts; in the 4T cell there is more room to design an optimized geometry between the two subcells. Applying nanostructures should optimize both optical impedance matching and carrier collection and conduction.

For the parasitic absorption in the other layers, mostly the transparent oxide (ITO in light blue in both figures) is responsible, next to the hole/electron transport layers and the glass top substrate. The perovskite material of the 2T geometry, shows free-carrier absorption (green area) which is not taken into account in the 4T structure. For the transparent intermediate and front contacts, metallic nanostructures as for example Ag nanowires could be an interesting consideration, as they can show lower absorption compared to ITO as shown in previous studies [36, 37].

Finally, in both cell geometries, a significant fraction of light with wavelengths closely below the bandgap of perovskite is transmitted to the underlying silicon cell instead of being absorbed in the perovskite cell. In the case of the 2T tandem cell current matching is required and for this the absorption of the top cell has to be tuned to an optimized value that depends on the bandgap. For 4T tandem cells, the top cell ideally fully absorbs all light above the bandgap, as a higher voltage can be gained there. Nanophotonic interlayers can therefore be beneficial to help reducing optical losses in 2T and 4T tandem cells, and are very flexible in application for the different cell geometries as well as different absorber materials.

In this thesis, we introduce spectral splitters for optimized redistribution of spectral bands between the subcells in 2T and 4T tandem solar cells. We take advantage of metasurface light scattering insights developed in the first part of the thesis to create colored PV. We provide a theoretical outlook for the potential of spectrum splitters in 2T perovskite/silicon tandem cells and present an experimental metasurface solution for 4T tandem cells that combines the functionality of spectral splitting, light trapping and reflectivity control in one metasurface structure.

1.5. From lab scale to large scale

This thesis demonstrates novel concepts to improve photovoltaics that are based on state-of-the-art cleanroom nanofabrication technologies, such as spincoating, electron-beam lithography, plasma etching and electron beam evaporation. All techniques used have the potential to be used to fabricate large-area structures at an industrial scale. Plasma-enhanced chemical vapor deposition (PECVD) is already widely used in PV industry to deposit thin-film anti-reflection and passivation layers. Substrate-conformal imprint lithography (SCIL) has already been developed into a large-scale fabrication technique using cassette-based multi-wafer handling [38]. The metasurfaces fabricated

in this thesis, are partly based on patterns created by electron-beam lithography, but all of those could be transferred with SCIL.

To illustrate the potential of scaling up the structures proposed in this thesis, there are several companies already realizing tools for nanoimprint roll-to-roll processes. For example Morphotonics and Stensborg offer roll-to-roll nanoimprint methods. The plasma etchings step that is used in many fabrication routines of the thesis to transfer a nanopattern from the imprinting mask into the underlying material, could be replaced on large scales by wet etching processes. Alternatively, the metasurfaces could be imprinted directly, if a liquid sol-gel of the desired material is developed [16]. Recent advancements in the development of TiO_2 sol-gel are promising in this respect. Alternatively, the nanopatterns developed here inspire the use of spray coating of high index colloids, potentially in combination with self-assembly techniques, as it is already done widely for color coatings in the car industry. In summary, we think the designs and geometries presented in this thesis to improve PV have a realistic potential to be upscaled on industrial level and to be integrated into real-world devices.

1.6. Outline of this thesis

In this thesis we present the application of dielectric nanostructure for the improvement of photovoltaics. We design layers composed of scattering dielectric nanoparticles, arranged in metasurfaces and metagratings, that control the scattering of light in a tailored way. In the first part of the thesis we present the improvement of coloration of photovoltaics, from color creation through spectral control to more advanced directional control. In the second part of the thesis, we concentrate on improving the efficiency of perovskite/silicon tandem solar cells, applying spectral splitting metasurfaces.

Chapter 2 describes the coloration of silicon minimodules by an integrated scattering layer based on silicon Mie resonators. By tailoring the scattering particle size and shape we control the interference of electric and magnetic dipole modes of the nanoparticles to create resonant backscattering over a narrow spectral band. We show that a strong green coloration can be created that is only weakly dependent of the angle of incidence. The layer of Mie resonators is created by SCIL, describing a promising route for future large-scale fabrication. The structure shows low optical losses resulting in a drop of only 10% in the short-circut current of the silicon cell.

Chapter 3 further expands on the techniques introduce in Chapter 2. We show how the color space is increased and that multiple colors can be created. We extend the coloration to a technique in which we combine pixels of different colors, and experimentally demonstrate mixed colors and an example of a white coloration of a solar cell. Here the photocurrent losses are only ~19%, due to the fact that only a small desired spectral band of the light is reflected. The route of mixing colors by pixels shows a great flexibility in choosing colors by choice.

Chapter 4 is addressing the fact that the geometries in Chapter 2 and 3 are showing specular reflection behavior rather than scattering over a large angular band. This makes the coloration seem shiny and not matt as is preferred for some applications. To solve this issue, we create a reflecting Lambertian scattering metasurface, composed of individual metagratings that together result in reflectance at the resonant wavelength over a broad angular range, while at the same time cancelling the specular reflectance. We

fabricate an array of amorphous silicon particles on top of a Ag mirror that is protected by a thin dielectric, using electron beam lithography. We characterize the angular reflectance profile and show a scattering efficiency of 90%. We also show that we can use a combination of differently designed metagratings to create resonant angular reflectance distributions at will.

In Chapter 5 we further expand on the technique introduced in Chapter 4 by designing a (semi-) transparent metasurface that reflects light on resonance in a determined angular range. With this, we enable coloration of rooftop photovoltaic only towards one half space to an observer on the street. This approach allows very efficient coloration with minimal losses as less light reflection is needed for a smaller angular range. By tailoring the interference between the light scattering modes of the nanoparticles we control the metasurface scattering spectrum on a transparent substrate and control the directivity by arranging the particles into gratings with different pitch. We use the combined metagratings approach of Chapter 4, adjusting the design to show very high diffraction efficiencies on a transparent substrate. We experimentally demonstrate a solar cell with angled colored distribution with a reduction of only 13% in short-circuit current.

Chapter 6 shows the theory, design and experimental realization of a broadband back reflector metasurface based on the Huygens-Fresnel principles. Using a phase gradient approach we design a theoretical metasurface with unity efficiency for back reflection. We then present an experimental realization in which the calculated phase gradient is discretized and TiO_2 nanowires of different height build up a unit cell on a Ag mirror. We show that the metagrating exhibits back reflection for a broad range of wavelengths from λ = 490-940 nm with an efficiency above 85%.

In Chapter 7 we theoretically study the benefits of a spectral splitter integrated into a perovskite/silicon 2T tandem solar cell. Based on detailed-balance calculations we first show that the absorption in the perovskite top cell is very sensitive to choosing the right thickness to match the currents of the sub-cells. We describe how a spectral splitter can enhance absorption in the perovskite top cell to achieve optimum voltage harvesting for the tandem. We calculate that a Lambertian spectral splitter in between the sub cells, in the thermodynamic limit, can lead to a 6% (absolute) efficiency enhancement for high-energy bandgap top cells.

Finally, Chapter 8 addresses spectral splitting in 4T tandem cells. We design a metasurface light trapping spectral splitter for a perovskite-silicon tandem cell. This metagrating has the property to efficiently reflect light with energies above the bandgap of perovskite back to the perovskite and introduce light trapping of the reflected light. At the same time, the spectral splitter reduces reflection in the infrared and therefore enhances current collection in the silicon sub cell. We build the metasurface using SCIL and integrate it in a tandem cell, showing a current increase in the top cell of at least 3%. We describe potential further enhancements for this novel spectrum splitter design and estimate that an efficiency enhancement of 0.40% (absolute) can be achieved in a realistic perovskite/silicon 4T geometry using a properly designed metasurface spectral splitter

In summary, this thesis provides key insights into the use of dielectric scattering particles and metagratings for the improvement of solar cells. We introduce the use of reso-

nant metasurfaces and metagratings to control the color and angular scattering behavior of solar cells. Our work paves the way for potential large-scale application of these new concepts. We study the potential of spectral splitters in 2T tandem cells. Building on the metasurface and metagrating scattering concepts we introduce a new spectral splitter concept for 4T tandem solar cells that enhances current and voltage harvesting from the subcells. We present options for further improvements of the designs, and how they could potentially find applications in a wide range of tandem solar cell geometries.

2

Efficient colored silicon solar modules using integrated resonant dielectric nanoscatterers

The sunshine fills my hair
And dreams hang in the air

Wonderful Life - Black

We demonstrate photovoltaic modules with a bright green color based on silicon heterojunction solar cells integrated with arrays of light scattering dielectric nanoscatterers. Dense arrays of crystalline silicon nanocylinders, 100-120 nm wide, 240 nm tall, 325 nm pitch, are made onto module cover slides using substrate-conformal soft-imprint lithography. Strong electric and magnetic dipolar Mie resonances with a narrow linewidth (Q~30) cause strong (35-40%) specular light scattering on resonance (~540 nm). The green color is observed over a wide range of angles (8-75°). As the resonant nanoscatterers are transparent for the major fraction of the incident solar spectrum the relative loss in short-circuit current is only 10-11%. The soft-imprinted nanopatterns can be applied on full-size solar modules, and integrated with conventional module encapsulation. The dielectric Mie resonances can be controlled by geometry, opening up a road for designing efficient colorful or white building-integrated photovoltaics.

2.1. Introduction

Photovoltaics (PV) can make a major contribution to the generation of renewable energy at a very large scale. In the past decades, PV research has focused on the development of PV materials and solar cell architectures with the aim to raise PV conversion efficiency and reduce manufacturing costs. For PV to be applied on a very large scale it is essential that PV panels are well integrated into our built environment and landscape. A key property in this respect is the perceived color of PV panels. Typically, PV panels have a black or dark blue appearance that results from the textured surface of the solar cells in combination with a dielectric antireflection (AR) coating, designed to optimize the absorption of sunlight in the solar cell. However, for building-integrated applications it would be beneficial to have PV panels in a variety of well-defined colors, while maintaining a high PV conversion efficiency.

So far, limited examples of colorful PV applications have been presented in the literature. Multilayer interference coatings can be applied to tailor the reflection spectrum, but are expensive to make and show strong angle-dependent reflectivity, unless a large number of layers is used [18, 19, 21]. Colored encapsulation of semitransparent thin-film silicon solar cells has been used to create solar panels with a red appearance for rooftop applications [39]. However, this leads to a reduced efficiency due to light absorption by the polymer encapsulant. Similarly, assembled Ag nanostructures have recently been used to create colored solar panels due to the excitation surface plasmon resonances, but at the price of Ohmic dissipation in the metal nanoparticles [27]. Furthermore, the development of white solar panels was recently reported using an undisclosed geometry, resulting in a 40% loss in efficiency [40]. So far, practical solutions for wide-angle colorful PV panels with high efficiency are scarce. Dielectric nanostructures are known to have bright scattering colors due to the excitation of Mie resonances. The resonant spectrum can be tailored by particle shape and refractive index [41]. If made from low-loss dielectrics the Mie resonance can have a relatively narrow linewidth, resulting in a bright scattering spectrum with -depending on the used dielectric- negligible absorption losses. The angular distribution of the Mie scattered light can be tuned by tailoring the interplay of the electric and magnetic dipole and higher order modes [42]. Several authors have demonstrated colorful examples of light scattering from arrays of Mie scatterers made on planar substrates [43–47]. So far, the use of Mie scattering to create colorful PV panels has not been explored. Dielectric Mie scatterers have been applied onto the surface of solar cells as forward scattering geometries that enhance the light incoupling [15, 48]. Furthermore, Mie scatterers embedded in thin-film solar cells have been demonstrated to serve as light trapping geometries [14]. Here, we introduce the use of dielectric Mie scatterers, integrated with the top cover layer of a solar panel, to selectively scatter a narrow band of the solar spectrum resulting in a bright green color. The unscattered blue and red/infrared spectral ranges are efficiently coupled into the solar cell leading to a reduction in short circuit current density of only 10% (relative) compared to the uncolored reference.

2.2. Integrated Mie scatterers for green solar modules

Figure 2.1 shows the integrated Mie scattering designs that we developed. In Fig. 2.1(a) the dielectric scatterers are placed on top of a thin 1.2×1.2 cm^2 sapphire cover slide that is placed on top of a textured crystalline Si (c-Si) solar cell using index matching oil in between. In a second geometry (Fig. 2.1(b)), the Mie scatterers are placed on the bottom of the sapphire slide, facing the cell. The nanopatterned sapphire cover slides were placed on a front- and back-contacted Si heterojunction solar cell using index-matching fluid (Fluka 10976, n = 1.52). The silicon heterojunction cells were made on 6" n-type single-crystalline Si wafers and subsequently laser-scribed to obtain 2×2 cm^2 cells. The surface of the cell was textured using alkaline chemical etching, leading to a random pyramidal texture (base width ~5 µm) and covered with an indium tin oxide (ITO) transparent conductor with an optimized thickness of 80 nm to act as an efficient AR coating (n = 2.05 at 630 nm). The use of index-matching oil enabled a flexible geometry to systematically compare the mini-modules (laminates) with and without the light scattering top layers. Sapphire was used to enable the use of crystalline Si Mie scatterers as crystalline silicon-on-sapphire substrates are commercially available. In practice, a similar geometry as proposed in Fig. 2.1 can be realized in a large-area solar panel by using a nanopatterned silica glass cover plate and an EVA lamination layer, as commonly used in solar panels.

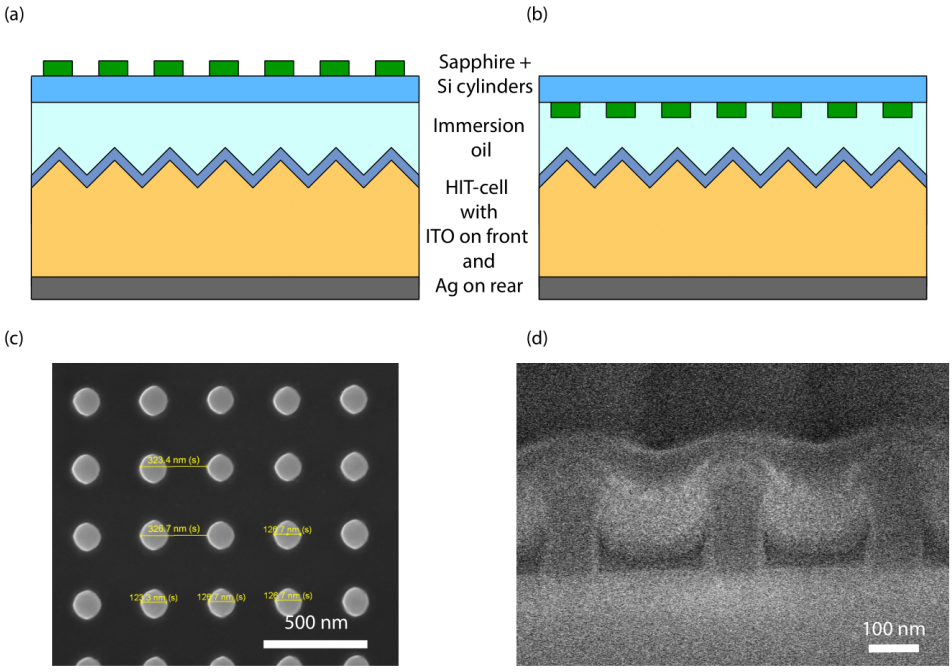

Figure 2.1: Integrated Mie scattering designs for colored solar panels. (a,b) Schematic of silicon nanoscatterer arrays on top (a) and bottom (b) of a sapphire cover slide, integrated into a silicon heterojunction solar module using immersion oil. The sapphire slide and the immersion oil mimic commonly used module glass and EVA. (c) Top-view SEM image of a square array of silicon nanoscatterers on a sapphire cover slide, made by SCIL. (d) SEM image of a cross section of the silicon nanoscatterers on sapphire made using focused ion beam milling.

2.3. Experiments

2.3.1. Fabrication

Silicon-on-sapphire substrates (500 nm Si on 0.46 mm sapphire, MTI Corporation) were etched down to a thickness of 200 nm using reactive ion etching (RIE) in a HBr_2 (25 sccm) and O_2 (2 sccm) plasma. Next, we used substrate conformal imprint lithography (SCIL) [49] to fabricate arrays of silicon cylinders. A 45-nm-thick silica sol-gel film was spin-coated and patterned using a SCIL stamp that was made from a pre-patterned silicon master, fabricated by electron-beam lithography. Two subsequent RIE etch steps were performed, first to break through the sol-gel pattern using CHF_3 (25 sccm) and Ar (25 sccm), and second, to transfer the pattern into the silicon layer using HBr_2/O_2. The square array of silicon nanocylinders with a pitch of 325 nm is seen in the top-view scanning electron microscopy (SEM) image in Fig. 2.1(c). A cross-section of the structure is shown in Fig. 2.1(d). It shows the particle diameter is slightly varying with height in the range 100-120 nm; the particle height is 240 nm. The size of the individual scatterers was chosen in order to create a visible reflection in the green. By changing the size of the particles, the resonance can be shifted and different colors can be reflected [46, 47].

2.3.2. Optical characterization

Figure 2.2 (insets) depicts the light scattering spectra for the two geometries in Fig. 2.1. Measurements were performed with an integrating sphere in reflection configuration. A collimated beam from a supercontinuum light source was coupled in at an incidence angle of 8°. In this setup, all light that is scattered/reflected from the sample in the upper halfsphere is collected and sent to a spectrometer. In the insets, reference measurements for a bare Si heterojunction solar cell and the unpatterned module are also shown. The bare cell shows low reflection due to the combination of texture and optimized AR coating (interference minimum at ~630 nm). The unpatterned module has a reflectivity of 7-12% as expected given the refractive index for sapphire. At long wavelengths the nanopatterned module in (a) shows a lower reflectivity than the unpatterned reference due to an (effective-index) AR coating effect of the Si particles on top of the sapphire. The scattering spectra of both integrated Mie scattering designs show a clear resonance (peak amplitude 35-40%), due to the magnetic (550 nm) and electric (528 nm) dipole resonances [50, 51]. The resonance in Fig. 2.2(a) is slightly red-shifted compared to that in Fig. 2.2(b) due to the higher index of the matching fluid. The linewidth of the scattering resonances (quality factor Q~30) is mostly determined by (desired) radiation losses, in combination with small absorption losses. The main panels in Fig. 2.2(a,b) show the angle dependence of the specular reflectivity, measured at the peak of the electric dipole resonance. In both cases the reflectance is strongly enhanced over the entire angular range from 8-75°, when compared to the unpatterned module. This behavior is quite different than what is observed for simple multilayer interference coatings of which the reflectivity is determined by Fabry-Perot interference which is strongly angle dependent at a given wavelength. In contrast, the localized nature of the Mie resonances used here enables strong light scattering within a narrow spectral band over a broad angular range. The insets in Fig. 2.2 also show that for off-resonant wavelengths the reflectivity does not deviate much from the reflectivity of the non-patterned reference. Figure 2.2 (c,d) shows

photographs of an unpatterned module and the nanopatterned module (bottom configuration), taken under diffuse daylight; a clear green color is observed. The visual color calculated from the measured reflection spectra (following the concept in Ref. [52], using the average midday light spectrum in Western Europe (D65) as illumination source) is shown in Fig. 2.2(e); it corresponds well to the color in the photograph of Fig. 2.2(d).

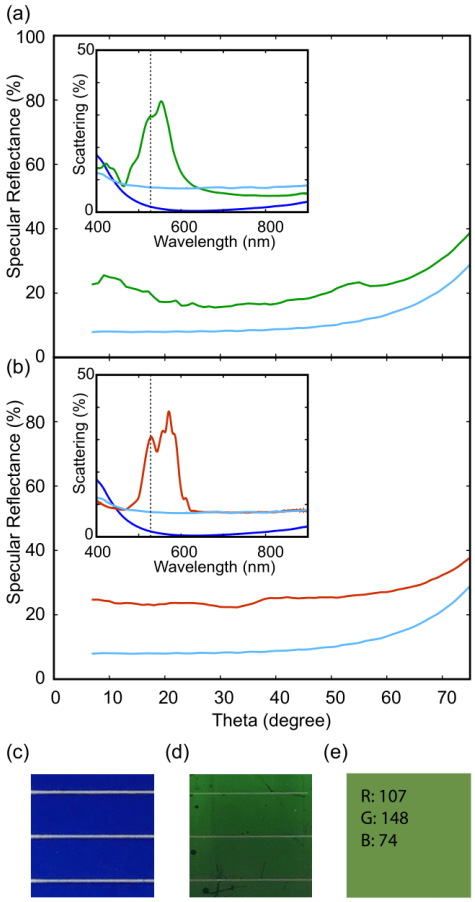

Figure 2.2: Optical reflectance of nanopatterned Si heterojunction solar modules. Measured angle-dependent specular reflectance (averaging data for s- and p-polarized light) at the electric dipole resonance (λ = 528 nm) of integrated design with nanoscatterers on top ((a), green) and bottom ((b), red) of the sapphire slide. Data for an unpatterned module are shown for reference (light blue). Insets: measured scattering efficiency of integrated design for top (a) and bottom (b) configurations. Data for an unpatterned module (light blue) and the bare Si heterojunction solar cell (dark blue) are also shown. Vertical black dashed lines at λ = 528 nm mark the electrical dipole resonance. Photographs (0.5x0.5 cm^2) of unpatterned modules (c) and nanopatterned module (d, bottom configuration), and (e) calculated visual color with the respective RGB values for the nanopatterned module.

2.3.3. Electrical characterization

Figure 2.3(a) compares the measured external quantum efficiency (EQE) of the two nanopatterned modules, the unpatterned reference, and the bare Si solar cell. The active-area EQE spectrum was measured using slightly focused light (2 mm diameter) under normal incidence from a Xenon light source sent through a monochromator. The EQE of the bare Si heterojunction cell approaches 100% in the 600-900 nm spectral range. For the unpatterned geometry the EQE is reduced by 7-12% (relative) in agreement with the higher reflectivity observed in Fig. 2.3. The corresponding integrated short circuit current density J_{sc}, derived from the EQE spectra, decreases from 39.5 mA/cm^2 to 36.8 mA/cm^2. The EQE spectra for both integrated designs show strong dips (25-30%) at the resonant wavelengths, resulting from light scattering and absorption by the Si nanoscatterers. For the top configuration the EQE is enhanced between 600 and 1000 nm in accordance with the reduced reflectivity (inset in Fig. 2.3(a)). For both top and bottom configurations the EQE is significantly reduced for wavelengths below the resonance, due to light absorption in the Si nanoscatterers. Correspondingly, the J_{sc} drops to 33.2 mA/cm^2 (top configuration) and 32.7 mA/cm^2 (bottom configuration). This corresponds to a reduction of 16% and 17% (relative) compared to the bare Si heterojunction cell and 10% and 11% (relative) compared to the unpatterned module. The inset in Fig. 2.3(a) shows the current-voltage ($I-V$) characteristics for the two patterned module configurations and the unpatterned reference. The $I-V$ curves were measured using a AM1.5G solar simulator (Newport Oriel Sol2A Class ABA), using a shadow mask to match the illuminated area to the size of the regular fabricated nanoparticle array (0.7×0.7 cm^2). The data are in full agreement with the trends observed in the EQE spectra, with the short-circuit current reduced due to the reduced light incoupling in the cells, and the bottom configuration showing slightly better performance than the top one. The V_{oc} values obtained from the $I-V$ measurements are strongly affected by the fact that the unmasked measurement area is much smaller than the cell area, creating an additional dark-current due to the unirradiated cell area (full-area 6" cells from the same batch had a V_{oc} of 724 mV). Obviously, the light incoupling effect of the nanopatterned geometry is best probed by changes in J_{sc} as these are a direct measure of changes in the light absorption. The conversion efficiency determined from the $I-V$ curves is 17.0% for the bare Si heterojunction cell, 15.9% for the unpatterned module and 13.7% and 12.9% for the nanopatterned modules in front and bottom configuration, respectively. These efficiencies for the colored Si heterojunction solar modules correspond to a relative reduction in efficiency, compared to the unpatterned modules, of 14% and 19%, respectively. The lowest efficiency loss is thus achieved for the front patterned configuration, which is due to the (effective-index) AR coating effect of the front-nanopattern, as described above.

Finally, Fig. 2.3(b) shows the "effective" solar spectrum impinging on the Si heterojunction cell, taking into account the effect of the nanoscatterers. The standard AM1.5G solar spectrum is modified taking into account the transmission spectrum measured using an integrating sphere on a nanoparticle array on a bare sapphire slide (front configuration, inset in Fig. 2.3(b)). The nanoscatterer array reduces the total integrated power from 1000 W/m² to 776 W/m^2. The Shockley-Queisser efficiency limit for a Si solar cell calculated using the modified spectrum is 32.8%. The maximum power output for the nanopatterned cell derived from Fig. 2.3(b) is reduced by 24%. This reduction is larger

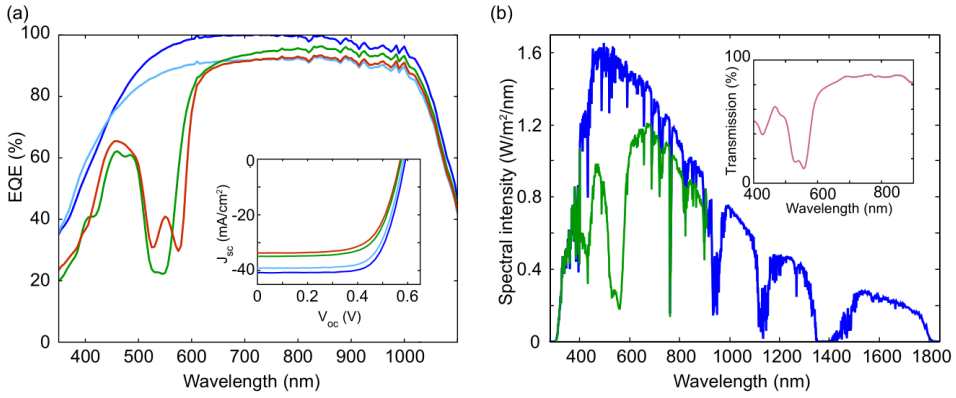

Figure 2.3: Electrical measurements and solar spectrum. (a) Measured EQE of bare silicon heterojunction solar cell (dark blue), unpatterned module (light blue), and nanopatterned module in top (green) and bottom (red) configuration. Inset: $I-V$ curves for the same cells. (b) AM1.5G solar spectrum (dark blue) and calculated modified spectrum after correction using the measured transmission spectrum (inset) of a nanopatterned sapphire slide (front configuration, green).

than that derived from the EQE data in Fig. 2.3(a) (16-17%). We ascribe this difference to the fact that in the transmission measurements light is reflected from two sapphire interfaces while for the module cell geometry one sapphire interface is nearly index matched.

2.4. Conclusion

Our work has several advantages over earlier work on colored photovoltaics using plasmonic scattering [27]. First of all, dielectric scattering is characterized by low absorption loss compared to the strong Ohmic dissipation in plasmonics scattering, as demonstrated by the relatively low loss in short-circuit current observed above. Furthermore, when compared to the plasmonic resonances, geometric Mie resonances can be tuned over a larger spectral range while maintaining low loss, enabling a larger practical range of colors. The narrow linewidth observed for the Mie resonances also presents an advantage over colored photovoltaics based on absorbing dyes, that typically shows broadband absorption into the UV. The choice of the dielectric material for the resonators is determined by the need of a high index low-loss material. In this work, crystalline silicon was used because of its high dielectric constant and well known nano-fabrication parameters. Finally, we discuss the angular behavior of the integrated Mie scattering solar panel design presented here for practical applications. As shown in Fig. 2.2, the strong specular reflection at the resonance wavelength creates a clear green appearance of the cell for a broad range of incident angles. A further advanced design would scatter light from a single incident angle to a broad range of outgoing angles. Future work will focus on designing such surfaces. In conclusion, we demonstrated efficient colored photovoltaic modules by the integration of dielectric nanoscatterer arrays in the front module layer using soft-nanoimprint technology. The nanoscatterers show characteristic Mie resonances that create a well-defined scattering color. We present two designs, with Si

nanoscatterers either on the top or the bottom of the front module cover layer. A clear green appearance is observed over a wide range of angles for both configurations, with only 10-11% loss in short circuit current and efficiency. The low-wavelength absorbance losses in the Si nanoscatterers used here can be avoided by using non-absorbing dielectrics such as TiO_2 [45, 53]. The green solar modules presented here can find applications in building- and landscape-integrated photovoltaics of many different kinds. The SCIL nano-imprint technique used is applicable to full-area (15×15 cm^2) solar cell patterning [38], and can be readily scaled up to a roll-to-roll process that is applicable to full-size solar panels. The solar panel color can be changed by tuning the geometry of the dielectric nanoscatterers, which is readily done by adjusting the soft-imprint stamp. Furthermore, by using a combination of differently shaped Mie scatterers photovoltaic modules with a white appearance can be designed as well.

3

Colored solar modules using integrated pixelated resonant dielectric nanoscatterer arrays

Don't confuse your speed with the turning of the earth

You're a Runner – Me and My Drummer

Green colored photovoltaic modules based on silicon heterojunction solar cells integrated with periodic arrays of light scattering Si nanoscatterers were made. Here, we expand this concept to multiple colors and color combinations. We show that random arrays of silicon nanoarrays can be combined to pixels to create the desired color. By adjusting the coverage of pixels composed of different nanoparticle arrays different colors can be designed and the calculated chromaticity values can be obtained from the fabricated sample. The pixelated nanoscattering concept was used to realize a solar mini-module with a scattering spectrum close to white. The calculated relative loss in short-circuit current is only 19%. The nanoparticle pixel arrays can be made using soft imprint lithography opening up an alternative route for designing low loss colored PV modules.

3.1. Introduction

For photovoltaics (PV) to be applied on a very large scale it is essential that PV panels are well integrated into our built environment and landscape. Typically, PV panels have a black or dark blue appearance that results from the textured surface of the solar cells in combination with a dielectric antireflection (AR) coating, designed to optimize the absorption of sunlight in the solar cell. However, for building- and landscape-integrated applications it would be beneficial to have PV panels in a variety of well-defined colors, while maintaining a high PV conversion efficiency. Recently, we have reported a new method to create a green colored solar module using resonant light scattering from silicon nanoparticles with optical Mie resonances [24]. We exploited the use of dielectric Mie scatterers, integrated with the top cover layer of a solar panel, to selectively scatter a narrow band of the solar spectrum resulting in a bright green color. In the present paper, this concept is expanded in order to achieve a broad range of colors; and to create white solar mini-modules. The reduction in short circuit current densities is only 11% for the green colored mini-modules and 19% for the white colored mini-module.

3.2. Dielectric scatterers for coloration

Dielectric nanostructures are known to have bright scattering colors due to the excitation of Mie resonances. The resonant spectrum can be tailored by particle shape and refractive index [41]. If made from low-loss dielectrics the Mie resonance can have a relatively narrow linewidth, resulting in a bright scattering spectrum with -depending on the used dielectric- negligible absorption losses. Several authors have demonstrated colorful examples of light scattering from arrays of Mie scatterers made on planar substrates [43–47].

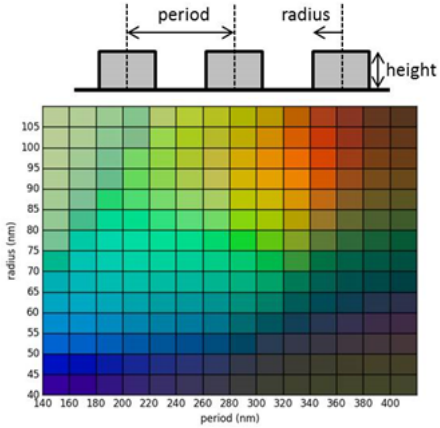

Figure 3.1: Color of reflection of periodic array of silicon Mie cylinders of a height of 100 nm on a sapphire substrate for different radius and period. Numerical simulations of reflection spectra were done using Lumerical FDTD and are transformed to visible color. A schematic of the geometry of the structure is shown above.

Figure 3.1 shows the result of numerical finite-difference-time-domain (FDTD) simulations (Lumerical) of the reflected color of square arrays of silicon nanocylinders (height

100 nm) on a semi-infinite sapphire substrate. The visual colors were obtained using the concept described in [52], using the average midday light spectrum in Western Europe (D65) as illumination source. By varying the radius and period of the Si cylinders, the Mie resonance spectrum is controlled and the color can be tuned over the entire color spectrum visible by the human eye. In Fig. 3.2 a photograph of a sample with six fields of silicon nanocylinder arrays of different radius and period (height 105-110 nm) on top of sapphire is shown. The fabrication was done by electron beam lithography and reactive ion etching of a planar silicon-on-sapphire substrate. The measured scattering spectra of the fields in Fig. 3.2a are plotted in Fig. 3.2b and show that with increasing radius and period the Mie resonances are shifting to larger wavelengths. The simulated reflectance spectra (height 105 nm) plotted in the same figure match well with the experiment. The scattering bandwidth is determined by the scattering rate and absorption losses in the nanoparticles and varies over the shown spectral range.

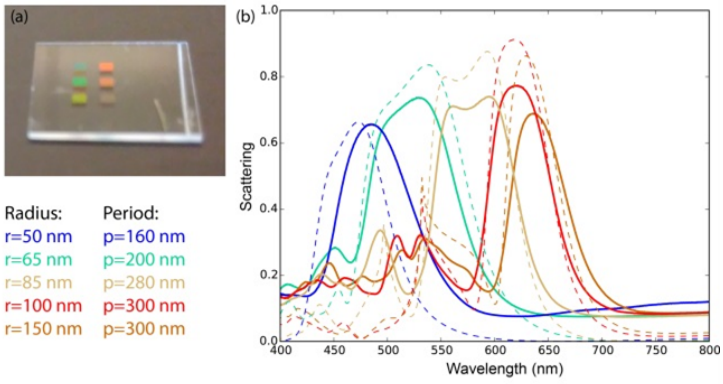

Figure 3.2: (a) Photograph of 6 fields of periodic arrays of silicon cylinders on top of a sapphire substrate with different radius and period (height 105-110 nm). Radius and periods of the simulated arrays are indicated. They match with ±10 nm the fabricated dimensions. (b) Measured (solid lines) and simulated (dashed lines) scattering spectra of 5 colored fields.

3.3. Printed single-colored cell

To integrate the Mie scattering effect into a solar module, the nanopatterned sapphire cover slides with periodic arrays of Si cyinders (diameter 100-120 nm; height 240 nm) on the bottom, were placed on a front- and back-contacted Si heterojunction solar cell using index matching fluid. The integrated design is shown in Fig. 3.3. The nanoscatterer array was fabricated by substrate conformal imprint lithography (SCIL).

Figure 3.4 (taken from [24]) shows the measured scattering spectrum of the integrated Mie scattering design. A clear resonance (peak amplitude 35-40%), due to the magnetic (550 nm) and electric (528 nm) dipole resonances is observed [50, 51]. Reference measurements for a bare Si heterojunction solar cell and the unpatterned module are also shown. The bare cell shows low reflection due to the combination of texture and optimized AR coating (interference minimum at 630 nm). The unpatterned module has

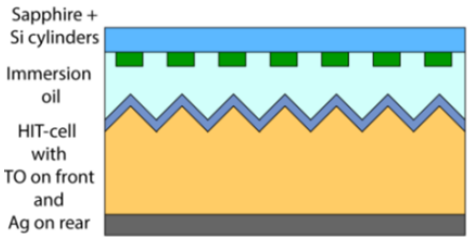

Figure 3.3: Schematic of silicon nanoscatterer arrays on bottom of a sapphire cover slide, integrated into a silicon heterojunction solar mini-module using immersion oil. The sapphire slide and the immersion oil mimic commonly used module glass and EVA.

a reflectivity of 7-12% as expected given the refractive index for sapphire. The inset in Fig. 3.4 shows a photograph of the 12x12 mm^2 sapphire slide with the green reflecting Mie scattering design on top of the HIT solar cell. The green scattering intensity is quite insensitive to variation in incoming angle. For more details, see [24].

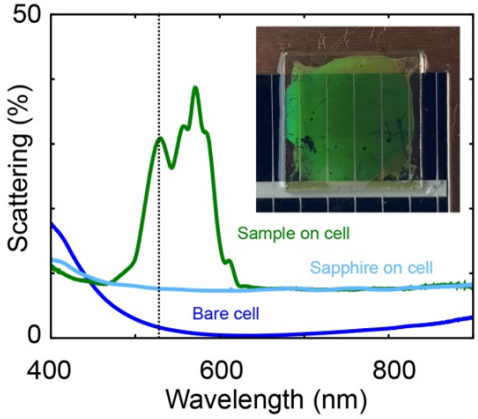

Figure 3.4: Measured scattering efficiency (green) of integrated design. Data for an unpatterned mini-module (light blue) and the bare Si heterojunction solar cell (dark blue) are also shown. Vertical black dashed line at λ=528 nm marks the electrical dipole resonance. Inset: Photograph of nanopatterned module shows bright green reflectance. Sapphire sample is 12x12 mm^2.

3.4. Mixed color pixels

As described in Section 3.2, by variation of the size and density of the nanocylinders, the reflected color can be tuned to the desired spectral color range. To achieve mixed colors or white, we combine pixels of different colors, with each pixel composed of 50x50 μm^2 nanocylinder arrays. Figure 3.5 shows SEM images of the blue (radius 50 nm) and red (radius 90 nm) scattering random nanocylinder arrays. A random geometry was implemented to avoid diffraction effects for large scattering angles.

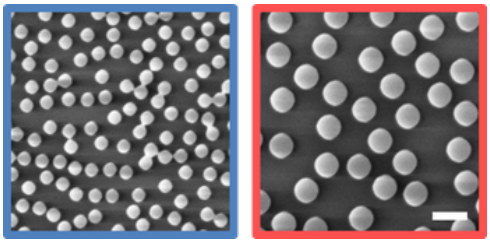

Figure 3.5: SEM top image of random Si nanocylinder arrays on sapphire, scattering in blue (left) and red (right). Scale bar is 500 nm.

In Figure 3.6, the measured scattering spectra of the blue and the red fields are shown (blue and red solid lines). The blue spectrum shows a weak resonance around 500 nm, the red spectrum shows strong first order resonances (electric and magnetic) around 800 nm and higher order resonances at 480 and 580 nm. The chromaticity values in the CIE 1931 xyY color space of the blue and red fields were determined by the concept described in Section 3.2 (see caption of Fig. 3.6). In order to obtain a chromaticity close to white by combining red (r) and blue (b) pixels, the ratio of the red and blue pixel coverage r:b was chosen so that the xy values match the white point of the CIE 1931 color space of D65 (x_{White}=0.3127, y_{White}=0.3290). The chromaticity values x_n and y_n of the combined color can be determined by:

$$(x_n, y_n) = (x_b, y_b)\frac{bB_b}{B_n} + (x_r, y_r)\frac{rB_r}{B_n} \tag{3.1}$$

with the brightness of the blue array $B_b = X_b + Y_b + Z_b$, the red array $B_r = X_r + Y_r + Z_r$ and the combined brightness of the mixed fields $B_n = B_b + B_r$ [54]. Using the xyY values determined for the reflection spectra, we find that a pixel coverage ratio of r:b=1:3 leads to chromaticity values of x_n=0.3181 and y_n=0.3283, close to the white point.

Combining the two reflectance spectra in the ratio 1:3, and applying the method to determine the CIE color space values gives the dashed calculated line in Fig. 3.6. Next, the fields are combined experimentally in pixels of 50x50 μm^2 (see microscope image in inset of Fig. 3.6). The measured scattering spectrum (solid grey line in Fig. 3.6) of this combined field matches well the calculated scattering curve; resonance peaks are matching well over the entire spectral range. The reflected scattering spectrum of the mixed pattern has an average intensity of 22% over the visible spectral range (450-800 nm)

3.5. Towards a white solar cell

Using the same approach as described in Section 3.4, a white colored solar mini-module was created. In these experiments the height of the nanocylinders was slightly smaller. Red to blue pixels had the optimized ratio r:b=1:9, and are shown in the microscope image in the inset of Fig. 3.7. The scattering spectra of the white integrated design, shown in Fig. 3.7, shows an average intensity of 20% over the visible spectral range. The chromaticity values obtained from the scattering measurement of the nanopatterned

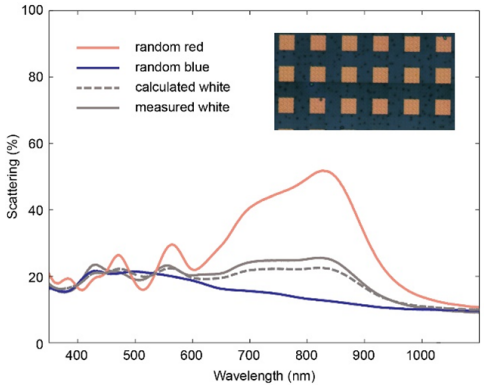

Figure 3.6: Measured scattering efficiency of blue and red reflecting random nanoarrays (blue and red solid lines). Spectra for calculated combined field (dashed grey line) and measured combined field (solid grey line) with ratio r:b=1:3. The chromaticity values of the plotted scattering curves are (x_r=0.3868, y_r=0.3573, Y_r=0.3160) for the red spectrum, (x_b=0.2813, y_b=0.3128, Y_b=0.1718) for the blue spectrum, (x_{cw}=0.3181, y_{cw}=0.3283, Y_{cw}=0.2078) for the calculated combined spectrum and (x_{mw}=0.3281, y_{mw}=0.3323, Y_{mw}=0.2221) for the combined measured spectrum. Inset: Optical microscope image of combined field. One red pixel and three blue pixels build a unit cell. Pixel is 50x50 μm^2

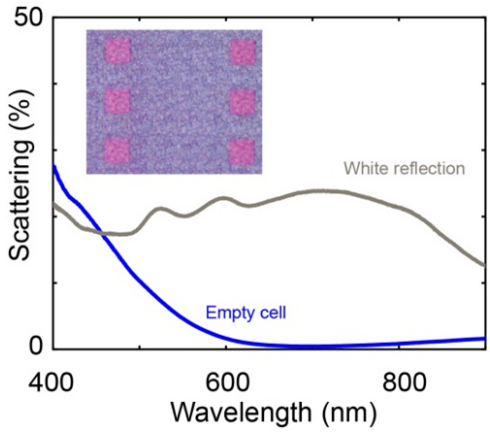

Figure 3.7: Measured scattering efficiency (grey) of integrated design of white field composed red and blue pixels. A spectrum for the bare Si heterojunction solar cell (dark blue) is also shown. Inset: Optical microscope image of combined field. One red pixel and 9 blue pixels are building a unit cell. Pixel is 50x50 μm^2.

module with combined red and blue fields are (x=0.3320, y=0.3491, Y=0.2152) and are close to the white point.

Figure 3.8 shows the measured external quantum efficiency (EQE) of the nanopatterned mini-module and the bare Si solar cell. The EQE spectrum for the integrated design shows a reduction (15%-40%) over the entire visible spectrum up to 800 nm, resulting from light scattering and absorption by the Si nanoscatterers. The reduction observed above 800 nm is due to the reflection off the sapphire substrate. Correspondingly, the calculated J_{sc} is reduced by 25% (relative) from 40.8 to 30.7 mA/cm^2 compared to

the bare Si heterojunction cell. Compared to the unpatterned module this would mean a relative reduction by 19%, taking into account 7% reflection from the sapphire slide. One way to decrease the losses in this configuration is to tune the resonance of the red field, in order to have less reflection above 700 nm, as any reflection in that spectral range cannot contribute to the color perception, but reduces the short circuit current. A photograph of the white sample is depicted in the inset of Fig. 3.8. The color appearance is grey, which matches the measured spectra, as grey has the same chromaticity as white but is less luminescent. The brightness of the structure could be increased by increasing the scattering intensity of the pixels respectively.

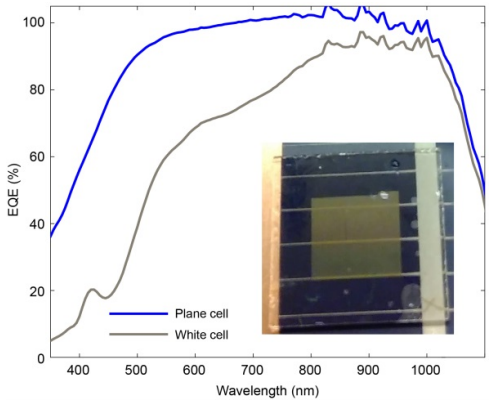

Figure 3.8: Measured EQE of bare silicon heterojunction solar cell (dark blue) and nanopatterned module with combined red and blue fields (grey). Inset: Photograph of nanopatterned module shows grey reflection. Sapphire sample is 12x12 mm^2.

3.6. Conclusion

In this chapter, we expanded the technology to create efficient bright green colored solar mini-modules to additional colors and white. We demonstrated the colored fabricated solar mini-module with a white scattering surface using pixels of integrated random nanoarrays. The concept can be widened to any desired color. The colored solar modules presented here can find applications in building- and landscape-integrated photovoltaics of many different kinds.

3.7. Methods

3.7.1. Fabrication - Electron beam lithography

Silicon-on-sapphire substrates (500 nm Si on 0.46 mm sapphire, MTI Corporation) were etched down to a thickness of 200 nm using reactive ion etching (RIE) in a HBr_2 (25 sccm) and O_2 (2 sccm) plasma. For this, a 50 nm thick layer of HSQ was spincoated on top of a silicon-on-sapphire wafer and patterned with a dose of 3400 $\mu C/cm^2$ in a Raith Voyager e-beam system. The samples were developed in TMAH (25%) for 60 seconds. Two subsequent RIE etch steps were performed, first to break through the sol-gel pattern using

CHF_3 (25 sccm) and Ar (25 sccm), and second, to transfer the pattern into the silicon layer using HBr_2/O_2.

3.7.2. Fabrication – SCIL

The silicon-on-sapphire substrates were etched down in the way described in the previous section. Next, we used substrate conformal imprint lithography (SCIL) to fabricate arrays of silicon cylinders. A 45-nm-thick silica sol-gel film was spin-coated and patterned using a SCIL stamp that was made from a pre-patterned silicon master, fabricated by electron-beam lithography. To transfer the pattern in the Si, the same etching steps as described in section 3.7.1 were performed

3.7.3. Reflectance measurements

Measurements were performed with an integrating sphere in reflection configuration. A collimated beam from a supercontinuum light source was coupled in at an incidence angle of 8°. In this setup, all light that is scattered/reflected from the sample in the upper halfsphere is collected and sent to a spectrometer.

3.7.4. EQE measurements

The active-area EQE spectrum was measured using slightly focused light (2 mm diameter) under normal incidence from a Xenon light source sent through a monochromator. The EQE of the bare Si heterojunction cell approaches 100% in the 600-900 nm spectral range.

4

Combined metagratings for efficient broad-angle scattering metasurface

Ich will einen Sommer lang nur tanzen

Einen Sommer lang nur tanzen – Fiva

Spectrally controlled diffusion and reflection of light are key operations for light management in many optical devices. Integration of this operation in complex nanophotonic devices requires a 2D interface that provides tailored spectrum and directivity control. Here, we present a metagrating superstructure that realizes a resonant light reflector with tailored angular scattering profile. Millimeter-sized metasurfaces are built from arrays of combined supercells of 20-50 μm, composed of 5-7 differently pitched metagratings that tailor at will and with large efficiency the angular response. Each supercell is composed of one or more Si Mie resonators, arranged in a periodic array above a Ag back plane and tailored to resonantly scatter light at 650 nm into only the ±1 diffraction orders with very high efficiency. By varying the pitch and supercell design, we can tailor the overall metasurface reflection profile with large flexibility, realizing a broad-angle Lambertian-type scattering metasurface, as well as a large-angle (35-75°) scattering metasurface, both with resonant optical scattering efficiencies above 70%. These ultra-thin structures, fabricated using thin-film deposition, electron beam lithography and reactive ion etching, can find applications for light trapping and spectrum splitting in solar cells and other devices.

4.1. Introduction

Materials to control light diffusion are traditionally composed of randomly packed high-index particles that support multi-wavelength scattering. These materials are typically based on multiple random scattering events, and therefore need to have thicknesses much larger than the optical wavelength. The properties of random media used for light scattering in solar cells [55, 56], random lasing [57, 58] and investigation of Anderson localization [59, 60] have been intensively studied. Random media often used in these studies consist of various types of "white paint"[55–57]. Artificially made random media for light diffusion such as photonic glass [58] and Mie glass,[61] have also been demonstrated.

For various applications, it is important to have randomly scattering devices with a much smaller thickness. In recent years, the metasurface literature has offered different solutions for flat two-dimensional surfaces providing diffuse scattering. So far, these solutions have been based on phase-coded metasurfaces, engineered by distributing a limited number of inclusions in a random-like fashion to locally manipulate the phase, amplitude and polarization of light, and thereby the shape of the scattered wavefront. Some work has been done on phase-coded metasurfaces for diffuse-like scattering with quasi-random phase coding in the microwave and infrared regime[62–64]. Metasurface diffusers at optical wavelengths were also studied, and their far-field response and performance for speckle-free imaging was studied[65–67]. However, graded metasurfaces composed of passive scattering surfaces have a fundamentally limited beam bending efficiency[68–70].

In this work, we demonstrate efficient broad-angle and large-angle light scattering from metagratings formed by locally periodic arrays of carefully tailored inclusions above a reflecting backplane, applying and extending a rigorous analytical theory that was introduced by Ra'di et al.[71]. In the optical spectral range, a metagrating is composed of resonantly scattering plasmonic or Mie particles placed in a periodic array above a metal reflector, supporting a discrete set of grating orders. For a well-chosen scattering cross section and spacing between scatterers and reflector, the specular reflection at resonance is fully cancelled by destructive interference of reflection from the back mirror and the zeroth order Floquet scattering mode[71]. In addition, the resonant scatterer geometry can be designed to only allow scattering power in one desired diffraction order, and to completely suppress scattering into all other allowed orders. Metagratings can be designed to operate around a resonant wavelength, with a tailored angular scattering profile, and an efficiency that is fundamentally limited only by absorption in the involved materials[71]. They can operate using either magnetic[71] or electric resonant modes[72]. Freeform inverse designs and fully analytical schemes to design metagratings employing diffraction gratings have been investigated[73–75]. This concept has also been employed to tailor wavefront control in transmission and reflection[76–78] using optimized scatterers with a shaped emission profile, without a direct link with theory.

Here we design a metasurface that combines multiple metagratings with different periodicities placed side by side in a supercell to create a reflector with precisely-engineered scattering profile. We extend the metagrating theory[71] and use numerical optimization to create a design based on magnetic Mie modes, experimentally demonstrating the functionality of the combined metagratings. A key feature of the proposed metasur-

face design is that it relies on a well-defined and precisely-engineered scattering profile, in contrast to most random light scattering geometries based on multiple scattering.

The reflecting metasurface presented here is composed of five characteristic length scales, designed based on the following steps (see Figure 4.1): (a) Si nanoparticles are designed to have a magnetic Mie resonance in the red spectral range; (b) the unit cells are composed of one or, in part of the structure, multiple scatterers to tailor angular scattering; (c) these unit cells are then placed in periodic arrays above a Ag backplane to form a metagrating that scatters light to a single diffraction order; (d) multiple metagratings are arranged into a supercell composed of 7 differently pitched metagratings to create a supercell with tailored angular scattering distribution; (e) a full-scale metasurface sample is then built up from randomly placed supercells.

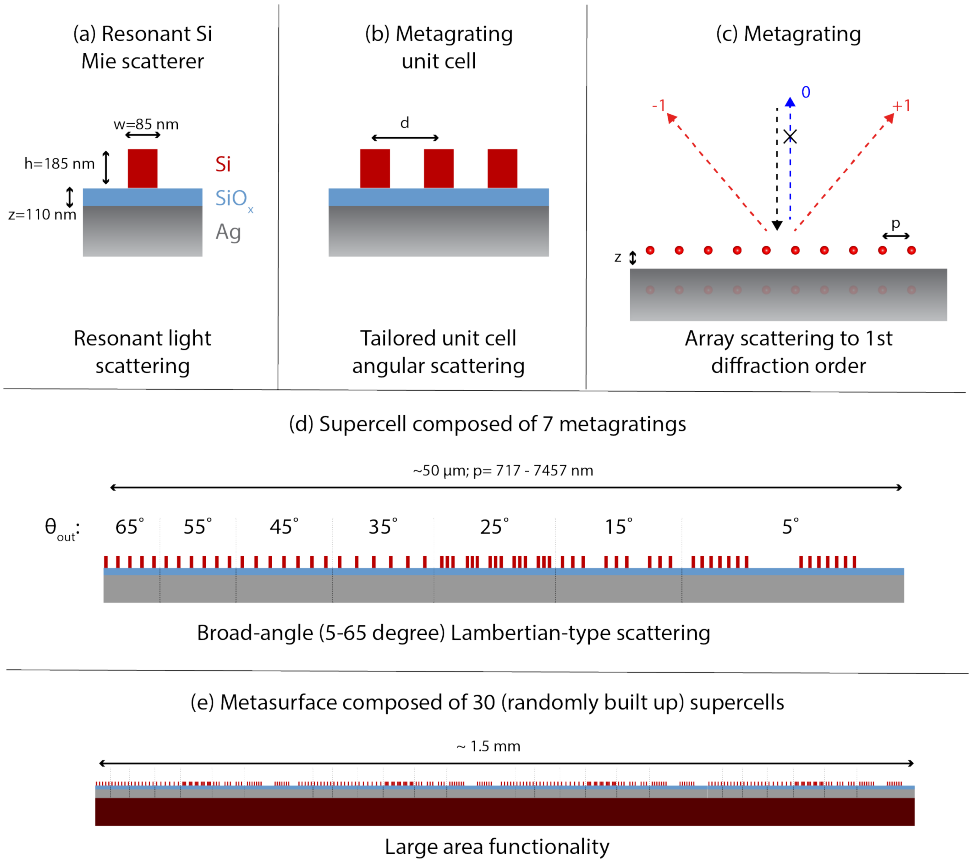

Figure 4.1: Metasurface design and length scales. Unit cells composed of one or more Si Mie resonators are arranged in a periodic array placed above a metal back plane to form a metagrating that scatters into only the ±1 diffraction orders. A supercell of metagratings creates a tailored angular response, and an array of supercells forms the large-area macroscopic metasurface.

Resonant broad-angle scattering profiles with well-defined angular distribution can find applications as diffusors, approaching a Lambertian scatterer. For example, reso-

nant diffusers can enable the creation of a matt appearance effectively creating "nanostructured paint", which has applications in e.g. colored solar cells [24, 25]. Creating structural color using dielectric nanoparticles[44–46] has been demonstrated before, focusing on spectral control rather than spectral and directivity control. To demonstrate the versatility of the metagrating design, we also demonstrate a functional surface with tailored large-angle scattering profile. This structure overcomes the typical inefficiencies faced by structures designed to scatter energy towards very large angles and can improve light trapping and spectrum splitting in (tandem) solar cells.

4.2. Theory and design

Following the work of Ra'di et al.[71], we first design a metasurface composed of an array of horizontally oriented magnetic dipoles located at a distance h above a perfect electrical conductor [see schematic in Figure 4.2 (a)]. Here, we consider normally incident light and set the periodicity in order to support two symmetric diffraction orders (i.e., ±1). The distance h can be controlled so that the fields in the specular direction are fully cancelled by destructive interference of light reflected from the mirror and the resonantly scattered zeroth-order Floquet grating mode. In this geometry all light can be redirected to a single desired diffraction order (+1 or -1) by choosing the resonant scatterer geometry, in such a way that scattering into the other diffraction order is nullified. Here since we aim at a symmetric angular scattering profile, we will design the metagrating to equally scatter into symmetrically-directed +1 and -1 channels.

Throughout the chapter, we limit the calculation and experiments to 2D functionality under normal incidence, however the same concepts can be readily extended to 3D and to any incoming illumination angle. The magnetic dipoles, induced by the incoming transverse magnetic (TM) plane wave $E_{inc} = E_0 \mathbf{y} e^{-ik_0 z}$ with amplitude E_0 and free-space wave number k_0, form a magnetic current $I_m^x = -i\omega\alpha_m H_{ext}^x$ where ω is the angular frequency, H_{ext}^x is the local magnetic field at the location of the particle, sum of the incident field and the reaction from the array, and α_m is the effective magnetic polarizability, including the array coupling. As shown earlier [71] (see also the analytical derivation in the Supplementary Material), α_m satisfies the generalized passivity condition

$$Im\left(\frac{1}{\alpha_m}\right) = \frac{\omega}{\eta_0 d}\sum_{n=-\infty}^{n=+\infty}\frac{1}{\cos\theta_n}\cos^2(k_0 h\cos(\theta_n)) \tag{4.1}$$

with η_0 being the free-space wave impedance, d the periodicity in the y direction and θ_n the diffraction angle(s) given by the grating equation. For normal-incident light, the zeroth order Floquet mode of the radiated field is $\boldsymbol{E_0} = Q_0 \boldsymbol{y} e^{-ik_0 z}$, where $Q_0 = \frac{1}{d} I_m^x \cos(k_0 h)$. The direct reflection from the ground plane can be cancelled by the Floquet mode if $Q_0 = E_0$. This leads to the following condition:

$$\frac{1}{\alpha_m} = \frac{2i\omega}{\eta_0 d}\cos^2(k_0 h) \tag{4.2}$$

For a grating with ±1 grating orders, equation 4.1 and 4.2 lead to the design equation for the cancellation of specular reflection:

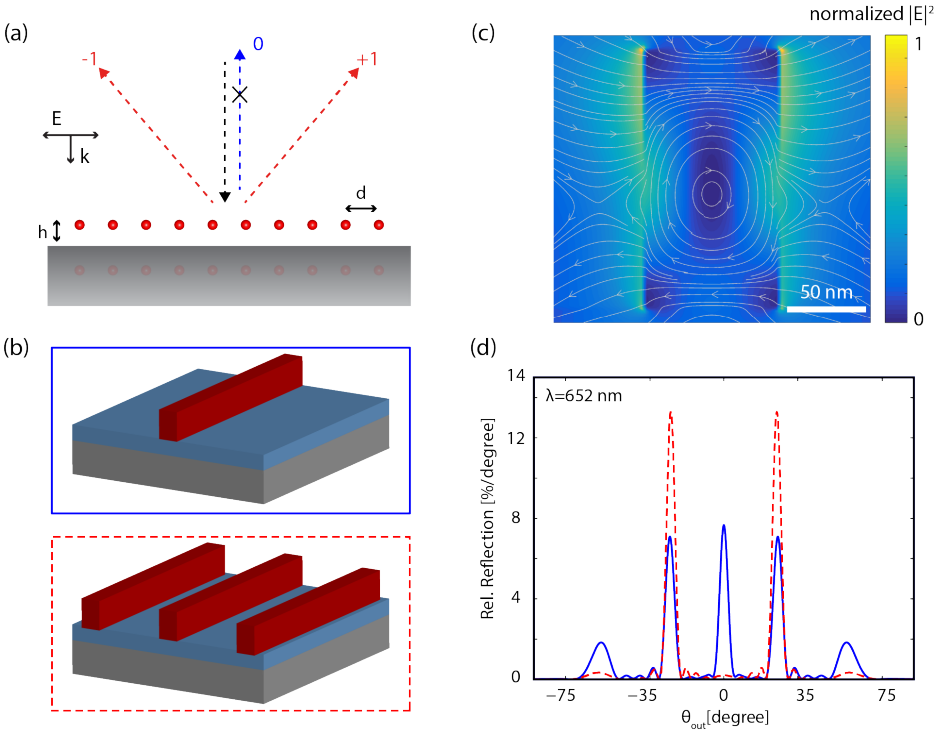

Figure 4.2: Magnetic dipole resonances in a 1D metagrating array (a) Periodic array of magnetic dipoles arranged over a ground plane. (b) Schematic of unit cells with one or three silicon bars on a silica spacer layer on top of a silver mirror. (c) Normalized electric field intensity $|E|^2$ and electric field lines (grey) in vertical crosscuts through an 85 nm wide and 180 nm tall Si bar on 110 nm SiO_x spacer layer on top of a silver mirror, parallel to the electric driving field. (d) Simulated angular scattering at λ = 652 nm in the far field for a finite metagrating with just 5 periods with pitch of 1538 nm. Unit cells are composed of a single silicon bar (solid blue line) or three silicon bars (spaced by 230 nm; dashed red line) placed above a Ag ground plane with a 110 nm silica spacer. Light coupling to the specular reflection and second order diffraction is suppressed for the three-particle unit cell.

$$\cos^2(k_0 h) = \frac{2}{\cos(\theta_1)} \cos^2(k_0 h \cos(\theta_1)) \tag{4.3}$$

Next, we create a metasurface that is composed by a distribution of metagratings, each designed to create a symmetric scattering profile over a different angular range. Given the limited size, each of them does not offer large directivity, but this is not an issue since the overall goal is to tailor the scattering over a broad angular range. By combining several of them placed next to each other, the overall scattering distribution can be tailored with large flexibility. In our design, we choose angles in a step size of 10°, to fill a major part of the scattering profile while maintaining the lateral dimension of the metasurface supercell below 100 µm.

4.3. Broad-angle scattering metasurface

4.3.1. Numerical simulations

2D Finite-Difference Time Domain (FDTD) simulations were performed to design a broad-angle scattering metasurface with engineered scattering profile. The unit cells in each metagrating are composed of one or more silicon rods placed on top of a silver mirror with a silica spacing layer, surrounded by air, see Figure 4.2(b). Each Si rod has a width of 85 nm, a height of 180 nm and the silica spacing layer has a thickness of 110 nm. The parameters of the rod are kept constant in all parts of the structure as the performance does not improve substantially for the different metagratings with changing parameters. Details of the numerical optimization can be found in the Supplementary Information. The structure is excited by TM-polarized light at normal incidence. The normalized electrical field distribution for a single scatterer on the silica-covered silver mirror at the resonance wavelength λ = 665 nm is plotted in 4.2(c) and the field lines show the typical electrical field loop corresponding to a magnetic dipole [50]. A single supercell of the structure is composed of an array of metagratings that are each composed of 2 to 7 periodically placed unit cells, to steer light efficiently towards the desired angular range. The number of unit cells for each metagrating is indicated in the schematic of 4.1(c) and the dimensions of all parameters are listed in Table 1. Side-by-side metagratings are spaced by the distance of one of the periodicities. We aim the broad-angle metasurface to operate in the 0-65° angular range, with metagratings scattering from 5-65°. The scattering towards 0° is provided by the residual of the specular reflection, so no extra supercells are needed to cover this portion of the scattering spectrum.

To address angles below 30°, we could utilize conventional gradient metasurfaces that perform well for small angles [68]. Here, instead, to cover this angular range we extend the metagrating concept and design a surface that not only eliminates scattering into the specular direction, but also has zero scatterings into higher orders modes other than ±1, leaving only scattering into the first diffraction orders (i.e., ±1). To do so, we compose the metagrating unit cell (that needs a single scatterer in the case of large-angle deflection, as in the design described above) of either 3 or 6 of identical scatterers, with their lateral distance tuned to achieve a scattering angular distribution that mainly couples to the first-order diffraction angle. This new approach has two advantages compared to conventional gradient metasurfaces: first, by maintaining the symmetry in the unit cell, the scattering effect remains angularly symmetric, which is ideal for our operation, but not typical for gradient metasurfaces; second, the higher scattering cross section of the composite unit cell helps balance the reflection from the mirror with the resonant scattering, thereby suppressing more efficiently the specular reflection. 4.2(d) shows the simulated angular scattering in the far field at λ = 652 nm for a finite metagrating with 5 periods and a pitch of 1538 nm (see schematic in 4.2(b)), composed of Si cylinders with dimensions described above. Clearly the three-particle design reduces the specular reflection, as well as higher-order diffraction in the metagrating geometry. This extension of the metagrating design, in which multi-particle resonant scattering and grating diffraction are combined, creates a tailored angular scattering distribution over a broad angular range that covers both small and large angles. According to Eqn 4.3, the optimum spacing h to cancel specular reflection increases for larger grating pitch. For the ease of fabrication, the silica spacing layer was kept constant for all metagratings

and optimized for diffraction towards 35°.

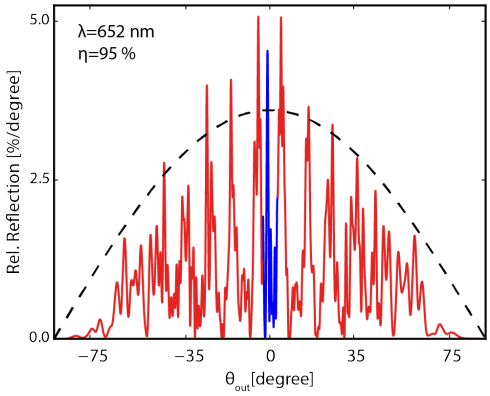

Figure 4.3: Broad-angle metasurface. Simulated angular scattering at $\lambda = 652$ nm in the far field for the broad-angle metasurface illuminated at normal incidence composed of diffracted (red) and specularly reflected (blue) light. The dashed black line shows the angular profile of a perfect Lambertian diffusor.

4.3 shows FDTD simulations of the far-field intensity of light reflected off our optimized design for a broad-angle metasurface at an operational wavelength of $\lambda = 652$ nm. Detailed dimension of all elements in the full metasurface design are given in Table 4.1. The metasurface supercell is composed of 7 metagratings with unit cells composed of either 1, 3, or 6 Si bars placed side by side (see 4.1). The number of unit cells in each metagrating was chosen such that the scattering intensity follows a Lambertian cosine distribution. In Figure 4.3 the effect of the distinct metagratings is seen in the discrete peaks in the scattering profile, and the overall shape follows the trend of a Lambertian profile that is overlaid for reference. We find that in this design the specular reflection is nearly fully eliminated, higher-order modes are effectively suppressed, and 95% of the incident light is scattered into the desired angular range. We note that in our simulations the scattered distribution is composed of discrete peaks. These are expected to be readily smeared out to create a smooth distribution by expanding the metagrating size and tailoring the range of metagrating pitches. In practical applications in photovoltaics the maximum number of metagratings in a unit cell is determined by the coherence length of sunlight. Importantly, the angular distribution will smoothen out when a broader spectral bandwidth of excitation is considered.

4.3.2. Experiment

Thin layers of silver (200 nm), SiO_x (110 nm) and silicon (185 nm) were deposited successively on a Si substrate by electron-beam thin-film deposition (Polyteknik Flextura Evaporator). After deposition, a 40 nm layer of HSQ was spin-coated on top of the silicon (Suss Microtec Delta 80 spincoater), patterned by electron beam lithography (Raith Voyager 50 kV electron beam lithography system) and developed in TMAH at 50 °C for 1 minute. After development, the rod geometry was transferred from the HSQ mask into the silicon using reactive ion etching (RIE) in a HBr_2 (48.5 sccm) and O_2 (1.5 sccm) plasma (Oxford PlasmaPro100 Cobra). The SiOx layer serves as an effective etch stop. The surface was

Parameter	Symbol	Broad-angle metasurface	Large-angle metasurface
Si Mie scatterer width	w	85 nm	85 nm
Si Mie scatterer height	z	180 nm	180 nm
Silica spacer layer thickness	t	110 nm	110 nm
Spacing between Mie scatterers and Ag mirror	h	200 nm	200 nm
Number of Mie resonators/ spacing in unit cell	n/d	6 /230 nm (5°) 3 /470 nm (15°) 3 /550 nm (25°) 1 (>25°)	1
Grating pitch in metasurface	p	720 nm (65°)- 7500 nm (5°)	670 nm (75°)- 1130 nm (35°)
Number of metagratings in supercell	-	5	7
Size of supercell	-	50 mm	20 mm
Spacing between supercells	-	720 nm - 7500 nm	670 nm - 1130 nm
Total metasurface size	-	1.5×1.5 mm2	1.5×1.5 mm2

Table 4.1: Overview of design parameters for broad-sngle and large-angle metasurfaces

fabricated in a 1.5×1.5 mm^2 field. Figure 4.4 shows a cross-section secondary electron microscopy (SEM) image of a single Si rod and a top-view SEM image of the supercell composed of 7 different metagratings. To circumvent diffraction effects each supercell of the metasurface is composed of a different arrangement of the same 7 metagratings. The distance between the supercells is varied from 720 nm - 7500 nm. The exact parameters of the structure for the broad-angle metasurface is listed in Table 4.1.

Optical reflection spectra were measured using an integrating sphere setup with the sample tilted 8° relative to the incoming collimated beam from a broad-band light source, to capture all scattered and specularly reflected light from the surface in the integrating sphere. Additional scattering measurements were made capturing only scattering into the grating orders (i.e., without specular reflection). In this case, the sample was placed without tilt at the back side of the integrating sphere, so that specularly reflected light was reflected out through the entrance opening of the integrating sphere. Figure 4.4(b) shows the measured total reflection and scattering spectra of the broad-angle reflecting surface. A clear scattering peak is observed around 636 nm, demonstrating the Mie-resonant nature of the metagrating geometry. The total reflectivity of the surface in the measured spectral range is 60-80%, with the remainder of impinging light being absorbed in the Ag back reflector and in the Si bars. This expectation is confirmed by the resonant dip in the total reflectivity at resonance.

The measurement setup for the angle-resolved reflection measurement is shown in Figure 4.4(c). A collimated, p-polarized beam of 636 nm light is incident on the sample surface. A detector (collection solid angle 0.0015 sr) positioned on a rotating stage around the sample allows angle-resolved measurements. In order to measure the spec-

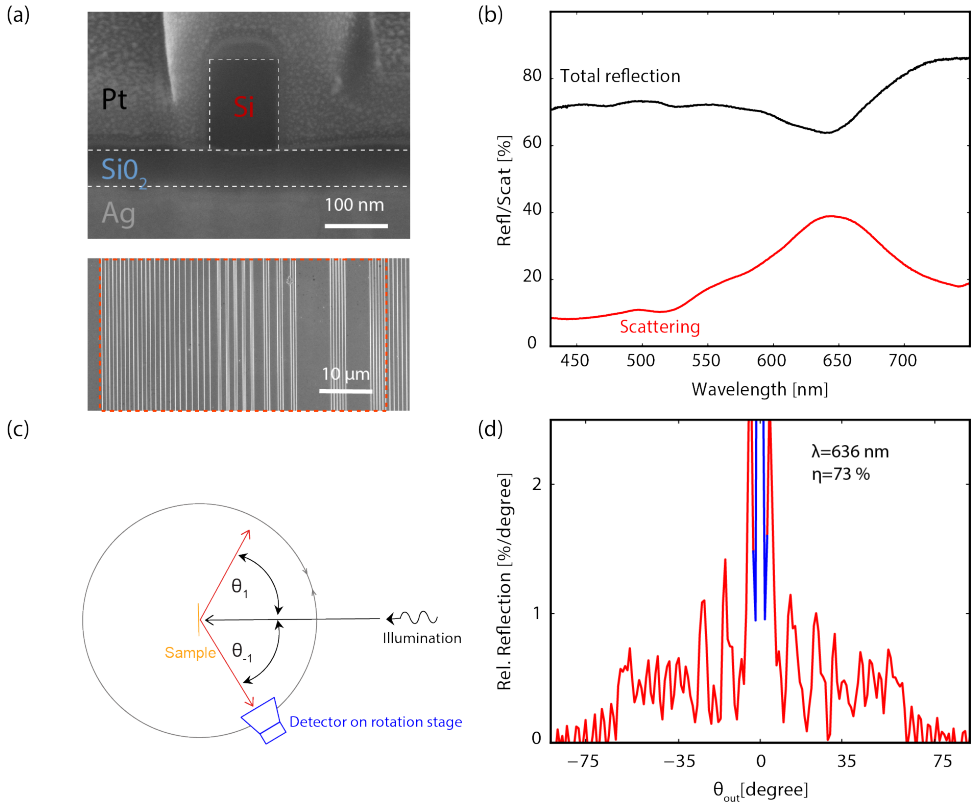

Figure 4.4: Fabricated broad-angle metasurface and optical measurements (a) top: Cross-section SEM image of a silicon bar on a SiO_x layer on Ag. To create image contrast the sample was covered with platinum before performing the FIB cross-section. Bottom: Top-view SEM image. The red dashed box represents a supercell composed of 7 differently pitched metagratings. (b) Total reflection (black) and scattering excluding specular reflection (red). (c) Schematic of angular scattering setup. The sample in the center of a rotating stage is illuminated with a vertical tilt of 10° by a collimated p-polarized light beam (spectral bandwidth 2.5-5 nm). The detector on the rotating stage with a vertical tilt of -10° collects the reflected power at a given horizontal angle θ_{out}. (d) Measured angular reflection on resonance (λ = 636 nm). The red data indicate the diffracted scattering, the blue data specular reflection.

ular reflection into the 0th order, the beam is incident under a vertical angle tilt of 10° above the sample and the detector is 10° below the sample. The angle-resolved measurement at the resonance wavelength [636 nm, bandwidth 2.5-5 nm, Fig. 4.4(d)] shows an overall spectral shape similar to simulations. In the experiment, 73% of the total reflected power is scattered into the 5-65° angular range. We attribute the remaining specular reflectivity (27%) to the fact that a fixed SiO_x thickness was used for all grating periods (while the optimum thickness decreases with pitch) and small fabrication inhomo-

geneities. The overall Lambertian shape can be approximated in experiments, but the specular reflection as well as small angle diffraction at 5 degrees does not follow exactly the calculated trend. These limitations can be attenuated by using an advanced metagrating fabrication procedure, to fully cancel the specular component. As mentioned earlier, the metagrating approach leads to a resonant behavior of the structure. Off-resonance, the metasurface shows very limited broad-angle scattering as is described below.

4.4. Large-angle reflector metasurface

4.4.1. Numerical simulation and experimental results

To illustrate the versatility of the metagrating design introduced here, which enables tailoring the angular scattering profile with large flexibility, we designed, fabricated and measured a scattering metasurface that only scatters into a predefined range of large angles. Such functionality is highly beneficial, for example, in light trapping applications in solar cells, where incident sunlight must be coupled to the in-plane waveguide modes of the solar cell [48, 79]. The large-angle scattering metasurface is composed of 5 metagratings that steer light into the 35-75° angular range, with each metagrating composed of 5 unit cells including a single silicon rod. Figure 4.5(a) shows the numerical simulation of the far-field angular scattering distribution of a single supercell [see Figure 4.5(b)] near the Mie-resonant wavelength at 660 nm. In this design, more than 90% of the incident power is scattered towards the ± 1 diffraction orders. An SEM top view of the fabricated large-angle metasurface is shown in Figure 4.5(c). The measured angular reflection [Figure 4.5(d)], shows the same trend as in simulations; 84% of the light is scattered into large-angle diffraction orders at resonance. The total reflection and scattering measurement data are shown in Figure 4.5(e), and clearly prove the resonant scattering nature of the large-angle metasurface.

4.4.2. Off-resonance optical performance of metasurfaces

As mentioned earlier, the metagrating design is based on resonant scattering from the building blocks. Figure 4.6 shows off-resonance (λ = 500 nm) reflection measurements of the broad-angle reflector and the large-angle reflector, overlaid with the resonant data presented above, i.e., Figures 4.4(d) and 4.5(d), respectively. The integrated off-resonance scattering efficiencies towards the grating orders are only 11% and 18% for two respective designs. This clearly shows that the proposed metagrating works on the principle of resonant scatterers. The existing off-resonance non-specular scattering of the structure can be explained by the broad linewidth of the magnetic dipole resonance of the silicon rods, as well as the existence of higher order modes that were not considered in the design.

A demonstration of the metagrating working as a “nanostructured paint” can be seen in Figure 4.7, which shows two photographs of the same sample, with 4 fields of broad-angle scattering metasurfaces in the left row and 4 fields of large angle scattering metasurfaces in the right row, respectively. The dimensions between the fields vary slightly due to a different choice of electron dose in the electron beam lithography writing. The SEM images and optical measurements of the two lowest fields are shown in this manuscript.

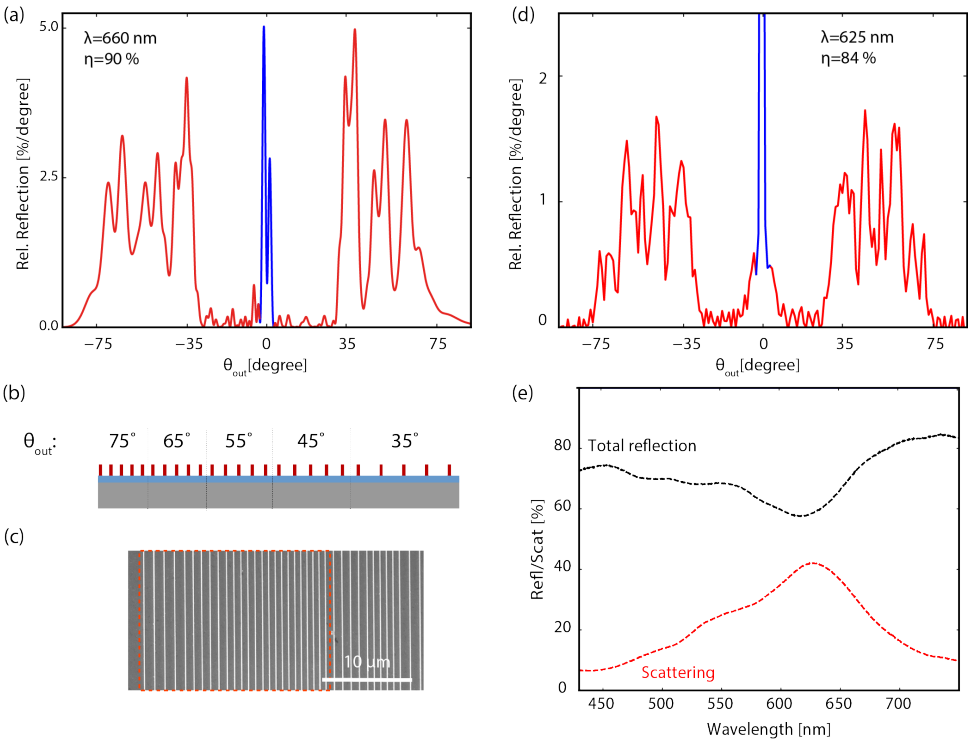

Figure 4.5: Large-angle reflector metasurface. (a) Numerical simulations of the angular reflection in far field for a single supercell of the large-angle reflector. (b) Schematic of the supercell. (c) SEM top view of the fabricated metasurface, the orange dashed box indicates a single supercell. (d) Angular reflection on resonance (λ = 625 nm). The red data indicate the diffracted scattering, the blue data specular reflection. (e) Total reflection (black) and scattering without specular reflection (red) of the large-angle reflector.

In both photos unpolarized white light is incident from the top, perpendicular to the sample. On the first photo, the specular reflection is captured by taking a photo from the top, in the second photo the scattering created by the metagratings is captured under an angle (around 45°). The color change visible in the photos indicates that only the color around the resonance (orange) is scattered sideways, and the rest of the spectrum (blueish, due to removed orange part of the spectrum) is reflected specularly.

4.5. Discussion and conclusions

In this work we demonstrated metasurfaces composed of combined metagratings with tailored angular scattering profiles. Based on a theoretical dipole scattering model, we

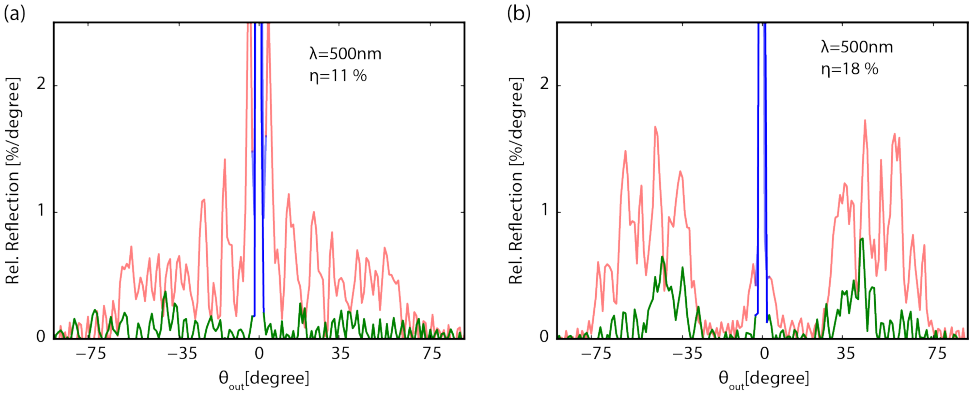

Figure 4.6: Measured angular reflection of the broad-angle reflector (a) and the large-angle reflector (b), off-resonance at λ = 500 nm. Diffracted scattering (green) and specular reflection (blue) contributions are shown. Data for resonant excitation (λ = 650 nm, same as Figure 4.4(d),4.5(d)) are overlaid for reference (red).

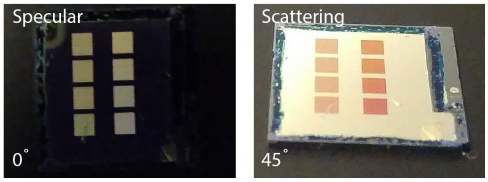

Figure 4.7: Photograph of sample with broad-angle scattering metasurfaces (left row) and large angle scattering metasurfaces (right row) illuminated by unpolarized white light under normal incidence. Photo taken under 0° (left) and 45° (right).

designed these ultrathin surfaces to realize broad-angle and large-angle scattering profiles. Using nanofabrication, we created Si Mie resonators on a Ag backplane and arranged the differently pitched metagratings in a supercell geometry to scatter light over the desired broad angular range. Combining multiple scatterers within a metagrating unit cell allows further control of the angular response, suppressing higher-order diffraction modes. Specular reflection is strongly suppressed, with 73% and 84% of the incident light scattered into the defined set of angles on resonance, for the broad-angle and large-angle geometries, respectively. Based on the same principles introduced here, extension of the design to 3D functionality and dual polarization can be readily explored. For example, 3D cylinders as scattering units have polarization independent resonance behavior and they could be placed in hexagonal grids to enable functionality on 3 axes. A further natural step for this work is to realize transparent resonant metagratings by controlling the interaction between suitable stacked Mie resonators, to replace the reflective back plane, in applications where transparency in the off-resonant spectral band is required.

Due to their high scattering efficiency and resonant operation, metagratings can

be used in a wide range of applications. The ultrathin resonant metastructures effectively create the functionality of "nanostructured paint", which can find applications in photovoltaics with colored appearance, a topic of great interest recently. By combining metasurfaces with different resonance wavelengths, multiple colored pixels may be envisioned, as well as diffuse surfaces with a white appearance [25]. Similarly, due to the spectral sensitivity, the presented metasurfaces can serve as spectrum splitting architectures in tandem solar cells. Furthermore, the large-angle scattering design can serve to enhance light trapping in thin-film solar cells, improving the effectiveness of coupling to in-plane waveguide modes. Many other applications in geometries that require a tailored (colored) scattering apperance come to mind as well, for example in controlling emission profiles in solid-state lighting and signaling where the spectral and directional control of light is important. The metagrating geometry introduced here, with many different length scales, can be readily fabricated in larger volumes using substrate conformal soft imprint lithography (SCIL)[38]. A full metagrating master pattern is then first made in a silicon wafer using electron beam lithography, from which a soft imprint stamp is then made that can transfers the pattern into a silica sol gel that serves as a mask for metasurface etching. Similarly, light scattering metagratings may be directly patterned using SCIL in a suitable high-index sol-gel layer.

4.6. Supplementary

4.6.1. Derivation of the design equations

We use the metagrating theory [71] for a periodic array of horizontally oriented magnetic dipoles. The structure is illuminated with a TM-polarized plane wave propagating in the yz plane:

$$\boldsymbol{E}_{inc} = E_0 \left(\boldsymbol{y} \cos(\theta_{inc}) + \boldsymbol{z} \sin(\theta_{inc}) \right) e^{-ik_0(\sin(\theta_{inc})y - \cos(\theta_{inc})z))} \tag{4.4}$$

with E_0 the amplitude, k_0 the free-space wave number and θ_{inc} the angle of incidence. The magnetic dipoles, induced by the incoming wave have each a magnetic current:

$$I_m^x = -i\omega\alpha_m H_{ext}^x \tag{4.5}$$

with H_{ext}^x the impinging magnetic field and α_m the effective magnetic particle polarizability. The dipoles are ordered in a periodic array (m×n) with periodicity d_x and d_y in x and y directions, respectively, and are located at a distance h above a ground plane. The magnetic surface current density $\boldsymbol{J_m}$ is the sum of the currents generated by the discrete magnetic dipole moments:

$$\boldsymbol{J_m}(x,y,z) = \boldsymbol{x} I_m^x \delta(z-h) \sum_{m=-\infty}^{+\infty} \sum_{n=-\infty}^{+\infty} \delta(x - md_x)\delta(y - nd_y) e^{-ik_0 \sin(\theta_{inc}) n d_y} \tag{4.6}$$

The Floquet modes into which the array redirects light are the diffraction orders of the given grating condition. To avoid scattering into higher order modes, we first consider the case of 1D periodicity in the y direction and grating geometries with only three

Floquet modes n=0, ±1 (first-order diffraction above 30°). The radiated field for Floquet mode n is given by:

$$\boldsymbol{E}_n = \left(\boldsymbol{y} - \boldsymbol{z}\frac{k_0\sin(\theta_n)}{k_0\cos(\theta_n)}\right) Q_n \exp(-i\,k_0\sin(\theta_n)\,y - i\,k_0\cos(\theta_n)z) \tag{4.7}$$

with

$$Q_n = \frac{1}{S} I_m^x \cos(k_0\cos(\theta_n)h) \tag{4.8}$$

S is the area of the unit cells ($S = d_y$ for 1D surface). As energy is conserved and no Ohmic dissipation is considered, the extinction power P_{ext} equals the power re-radiated in all Floquet modes:

$$P_{ext} = \frac{1}{2S} Re\{J_m \cdot H_a\} = P_{rad} = \frac{1}{2\eta_0} \sum_{n=-\infty}^{n=+\infty} \frac{1}{\cos\theta_n} |Q_n|^2 \tag{4.9}$$

Employing equation 4.5 and 4.8, 4.9 can be rewritten as:

$$Im\left(\frac{1}{\alpha_m}\right) = \frac{\omega}{\eta_0 d} \sum_{n=-\infty}^{n=+\infty} \frac{1}{\cos\theta_n} \cos^2(k_0 h\cos(\theta_n)) \tag{4.10}$$

In the radiated fields, the field of the n=0 Floquet mode is:

$$\boldsymbol{E}_0 = \left(\boldsymbol{y} - \boldsymbol{z}\frac{k_0\sin(\theta_0)}{k_0\cos(\theta_0)}\right) Q_0 e^{-i\,k_0(\sin(\theta_0)\,y - \cos(\theta_0)\,z)} \tag{4.11}$$

with $Q_0 = \frac{1}{S} I_m^x \cos(k_0 h)$. To cancel the specular reflection of the incident field from the ground plane with the n=0 Floquet mode the condition $E_0 = Q_0$ has to be fulfilled. Combining this condition with the form of the magnetic current from Equation 4.5 gives the condition:

$$\frac{1}{\alpha_m} = \frac{2i\omega}{\eta_0 d} \cos^2(k_0 h) \tag{4.12}$$

Now, we assume that only the 0,-1 and +1 grating orders can carry energy. Comparing equation 4.10 and 4.12 then leads to the design equation for the cancellation of the specular reflection:

$$\cos^2(k_0 h) = \frac{2}{\cos(\theta_1)} \cos^2(k_0 h\cos(\theta_1)) \tag{4.13}$$

This design equation describes which height h of the magnetic dipoles has to be chosen above the ground plane to fully redirect light at normal incidence to the ±1 diffraction orders.

4.6.2. Analytical antenna theory

To implement the metagrating theory into an analytical design structure, we use a method common in antenna theory, and derive the radiation of the total array of magnetic dipoles by summing up the far fields of all individual dipoles. Here, interaction of the dipoles is not taken into account. The far-field radiation by antennas for a magnetic dipole pointing in x direction is given by [80]:

$$E_\theta = i\omega\eta\frac{\epsilon m_x}{4\pi r}e^{-ikr}sin(\varphi) \tag{4.14}$$

$$E_\varphi = i\omega\eta\frac{\epsilon m_x}{4\pi r}e^{-ikr}cos(\theta)cos(\varphi) \tag{4.15}$$

with φ and θ the azimuthal and zenithal angles, respectively. If we consider a 1D geometry (dipoles in a line), $\varphi = \pi/2$, and the electrical field is described by:

$$E_\theta = i\omega\eta\frac{\epsilon m_x}{4\pi r}e^{-ikr} \tag{4.16}$$

Here, ω is the angular frequency, ϵ the permittivity, and μ the permeability ($k_0 = \omega\eta\epsilon$) and m_x is the magnetic moment which takes the form $m_x = \frac{1}{i\omega}SE_0$ due to the condition $E_0 = Q_0$. If the dipole is located above a ground plane with distance h, image theory can be used to describe the far field:

$$E_\theta = E_\theta^+ + E_\theta^- = ik_0 m_x(\frac{1}{4\pi r^+}e^{-ikr^+} + \frac{1}{4\pi r^-}e^{-ikr^-}) \tag{4.17}$$

with r^+ and r^- describing the distance to the dipole located above the ground plane and the image dipole below the ground plane. To calculate the fields in cartesian coordinates r^+ and r^- can be expressed as $r^+ = \sqrt{(y^2 + (z-h)^2)}$ and $r^+ = \sqrt{(y^2 + (z+h)^2)}$. The far field radiation of N_1 dipoles located next to each other at a distance d_1 (on the y axis) is then given by the sum of all individual dipoles and their image dipole:

$$E_{\theta,N_1} = \sum_{n=0}^{n=N_1} E_\theta^+(y - nd_1, z - h_1) + E_\theta^-(y - nd_1, z + h_1) \tag{4.18}$$

Continuing summing of radiated far fields, results in a total far field of all dipoles:

$$E_{tot,N} = \sum_{n=0}^{i=N} E_{\theta,N_i} \tag{4.19}$$

of $N = N_1 + N_2 + ... + N_m$ dipoles with N_1 dipoles with the distance d_1, N_2 dipoles with the distance d_2 and so on.

Based on this derivation, not taking into account the interaction between particles, a design of the far-field scattering of arrays of magnetic dipoles can be made. It should be noted that the scattering towards 0 degree cannot be cancelled mathematically, as here we are considering a finite array, while the design equation 4.13 is based on an infinite plane wave. For this reason, the analytical calculation gives us information about the overall shape of the angular scattering distribution, but not about its efficiency. Figure 4.8 shows the analytically calculated far field for the large-angle reflector metasurface, consisting of 5 magnetic dipoles per metagrating, with optimum height derived from the design equation.

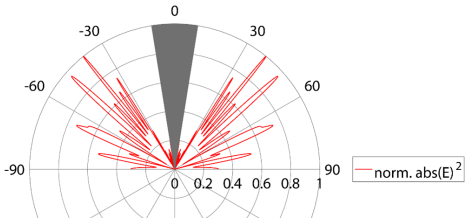

Figure 4.8: Angular profile of far-field intensity analytically calculated from the sum of 25 point dipoles (5 dipoles per angle, 35-75°) and their image dipoles with their respective distances z each obtained from the design equation. The zeroth order scattering contribution is removed (grey zone).

4.6.3. Optimization of structure by simulations

In the following steps, it is shown how we designed the final structure for fabrication. In all steps FDTD Lumerical is used. In all simulations for optimization, periodic boundary conditions were used and metagratings with one fixed period were studies. The structure was illuminated with a plane wave and the power to different grating orders was determined using the grating projection functionality of FDTD Lumerical. We choose to optimize the structure for an operational wavelength of λ = 650 nm, normally incident on a 1D array of Si pillars placed on a Ag substrate with a silica spacing layer. The array has a period of 919 nm (θ_{diff} = 45°). We fix the height z of the pillar to 180 nm. Now, by varying the width w and the distance h between Ag substrate and center of the pillar, we find that at for h = 200 nm and w = 85 nm, almost 50% of the reflected light is scattered towards the +1st order, which given the symmetry, translates to almost 100% diffraction efficiency into the n=±1 modes (Figure 4.9).

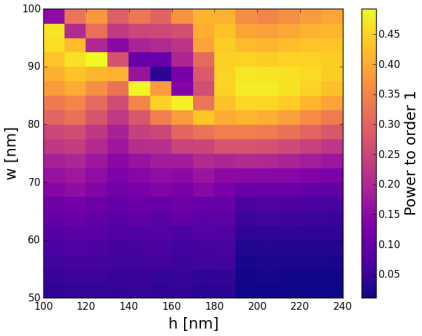

Figure 4.9: Diffraction efficiency into the 1st diffraction order as a function of distance h from particle to the Ag mirror and particle width w.

For ease of fabrication, the distance h was kept constant for all combined metagratings. To investigate the metagrating performance for λ = 650 with periodicities different from 919 nm, we vary the period p as well as the distance h (Figure 4.10). We find that for h = 200 nm for the smaller and bigger periods, up to a pitch of p = 1300 nm (above which the second diffraction order appears) the grating efficiency can be designed to be

above 35% (70% for both n=±1 orders).

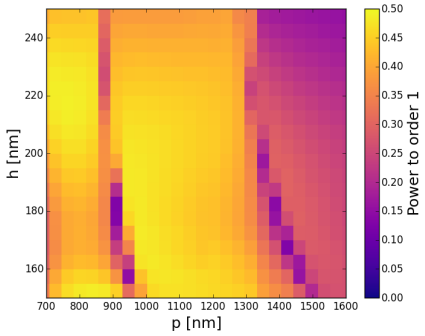

Figure 4.10: Diffraction efficiency into the first diffraction order as a function of array period p and distance h from particle to the Ag mirror.

In fabrication, the width of the individual metagratings can be easily tailored. We investigate how the width of the individual particles affects the performance for different periodicities and find that w = 85 nm gives the best result for all periods (Figure 4.11).

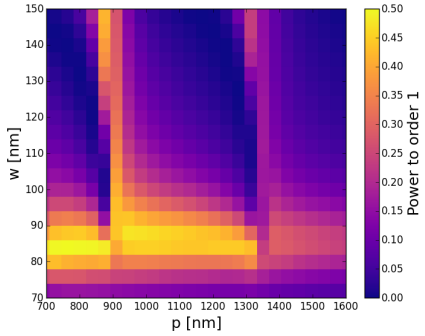

Figure 4.11: Diffraction efficiency into the first diffraction order as a function of array period p and particle width w.

With the chosen parameters (w = 85 nm, z = 180 nm, h = 200 nm), we investigate the effect of varying the array period for the 500-1200 nm spectral range (Figure 4.12). The resonant scattering effect around 650 nm is clearly seen for all periods, and a high coupling efficiency is observed for the bandwidth of the magnetic Mie mode, peaking near 100% on resonance.

As described in the main text, for first-order scattering angles $\theta_{diff} < 30°$ higher-order diffraction complicates the design, that focus on optimizing only the ±1 Floquet modes. As mentioned, we address this problem by modifying the unit cell to contain a number of identical scatterers (3 or 6, depending on the grating pitch) such that their scattering radiation profiles remain within the angular range below 30°. We tune the dis-

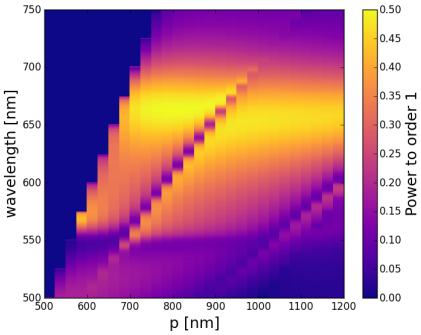

Figure 4.12: Diffraction efficiency into the 1st diffraction order as a function of array period p and wavelength, showing resonant behavior around 650 nm. No diffraction is observed in the dark blue region.

tance between the scatterers to optimize the scattering profile for the highest coupling efficiency towards the first diffraction order. For coupling to the 5°, 15° and 25° angles, we reach efficiencies between 38% and 48% (76% and 96% for both orders) by choosing optimized inter-particle distances of d = 550 nm, 470 nm and 230 nm, respectively (Figure 4.13).

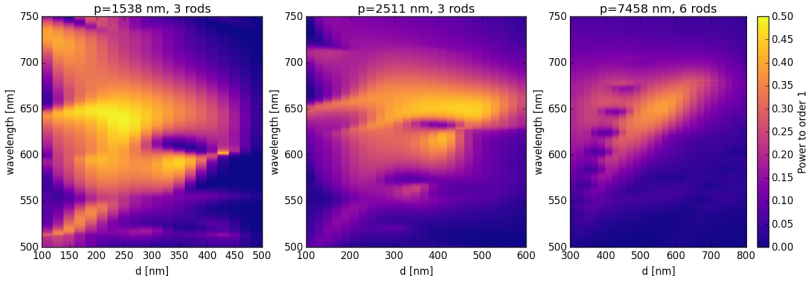

Figure 4.13: Diffraction efficiency into the 1st diffraction order as a function of Si pillar distance d and wavelength for (a) 3 pillars for θ=25° (b) 3 pillars for θ=15° (c) 6 pillars for θ=5°.

5

Resonant metagratings for spectral and angular control of light for colored rooftop photovoltaics

Open your eyes, look up to the skies and see

Bohemian Rhapsody – Queen

We design semi-transparent metagrating supercells that enable control over the spectrum and directivity of incident light for applications in photovoltaics with tailored angular appearance. The building block of the supercells is a 110-120 nm wide and 175 nm tall silicon nanowire that shows a strong Mie resonances around λ = 650 nm. By arranging the resonant Mie scatterers into metagratings of increasing pitch (675-1300 nm) we create a Lambertian-like scattering distribution over an angular range of choice. The millimeter-sized metasurfaces were fabricated using electron beam lithography and reactive ion etching. The fabricated metasurface nearly fully suppresses specular reflection on resonance while 10% of the incoming light around the resonance is scattered into the angular range between 30-75°, creating a bright red appearance over this specific range of angles. Off-resonant light in the blue, green and near-infrared is efficiently transmitted through the metasurface and absorbed in the underlying photovoltaic cell. The implemented silicon heterojunction solar cells with integrated metagrating supercells show a reduction in external quantum efficiency matching the resonant scattering spectral range. The short circuit current is reduced by 13% due to the combined effects of resonant scattering, reflection from the high-index substrate and absorption in the Si nanowires. In addition, to efficient colorful photovoltaics with tailored angular appearance, the metagrating concept can find application in many other light management designs for photovoltaics and other opto-electronic devices.

5.1. Introduction

New solar power conversion architectures are increasingly important to achieve large-scale sustainable power generation to sustain the growing energy needs of our society. Integration of photovoltaics (PV) into the local architecture, buildings and urban terrains is a rapidly growing research and technology area and will be crucial to meet the requirements set by the Paris agreement in the coming years [81]. Current commercial solar cells and modules typically have a blue or black color that does not always fit within the urban design. Modules with tailored color are necessary to integrate PV into residential and modern city building architecture, where aesthetics plays a key role. In order to achieve both functional beauty and high power conversion efficiency, it is essential to develop innovative PV solutions to create colored solar cells while maintaining high efficiencies.

Over the last decades, research has shown different approaches to achieve colored PV. Interference coatings and Bragg reflectors have been used to modify the reflected spectrum, but do not offer control over the angular scattering [18, 19, 21, 82, 83]. Colored optical coatings, based on polymer or luminescent materials have been applied on the front module glass of cells [84–87], but are often limited by absorption in the coating material. Other solutions, specifically for solar roof tiles, have been offered to control the field of view with louver films that shade the cells on a rooftop for observers from the ground [88]. This simple approach shows esthetical results; however, the performance of the solar cell is highly restricted if the sun shines at a low angle, because the louver film also shades the sunlight. Scattering from plasmonic nanostructures has been applied in colorful solar cells, but suffers from fundamental optical losses in the metal [27, 89]. Similarly, resonant dielectric nanoparticles have been used for spectrally controlled light scattering with minimal optical losses [43–47]. Recently, these nanostructures have been employed for the creation of colorful solar cells, with the advantage of very little losses and scalable fabrication possibilities [24, 25, 90].

So far, none of the proposed designs for colored PV exhibits both angular and spectral control on the reflected light. The possibility of designing the scattering angular profile at will is particularly appealing in colored PV applications for two main reasons: first, for a colored surface to appear matte its angular reflectance has to follow the Lambertian cosine law (i.e., the apparent brightness of the scattered light should be the same for an observer from every angle). Second, it is important to reflect the color to a specific field of view of choice in order to minimize the losses as much as possible. The most obvious example is the application of directional colored solar cells on rooftops, where a red color appearance should be seen only from an observer near the building, while reflection upwards is undesired.

The use of scattering dielectric nanoparticles allows controlling not only the spectrum, by exciting Mie resonances, but also the directivity by smartly arranging the scatterers into a metasurface. In previous studies, different metasurfaces, specifically metagratings, have been introduced to allow directional control of resonant reflection [71, 72, 74–78, 91]. In this work we demonstrate how the geometry of an array of dielectric Mie-scatterers arranged in a grating structure can be tailored such that light in a narrow spectral band is scattered over a well-defined angular range. To this end, we design a supercell of multiple metagratings consisting of dielectric nanoparticles that shows

Lambertian resonant scattering while the non-resonant spectral bands are effectively transmitted. We demonstrate these concepts in a one-dimensional geometry employing Mie resonances in subwavelength silicon nanowires (NWs) that allow us to gain spectral control over the reflected light for one polarization direction; the design can be readily expanded to two dimensions. The scattering resonances are tuned by optimizing the shape and spatial dimensions of the nanowires such that the scattering profile matches the desired scattering spectrum. We demonstrate resonant scattering around λ = 650 nm, yielding a red scattering profile. Next, the NWs are placed in multiple gratings on a transparent substrate that scatter light with a tailored distribution over the first diffraction orders. We apply the metasurface onto a Si solar cell and demonstrate that effective light scattering in a narrow spectral and angular band is combined with high external quantum efficiency of the solar cell.

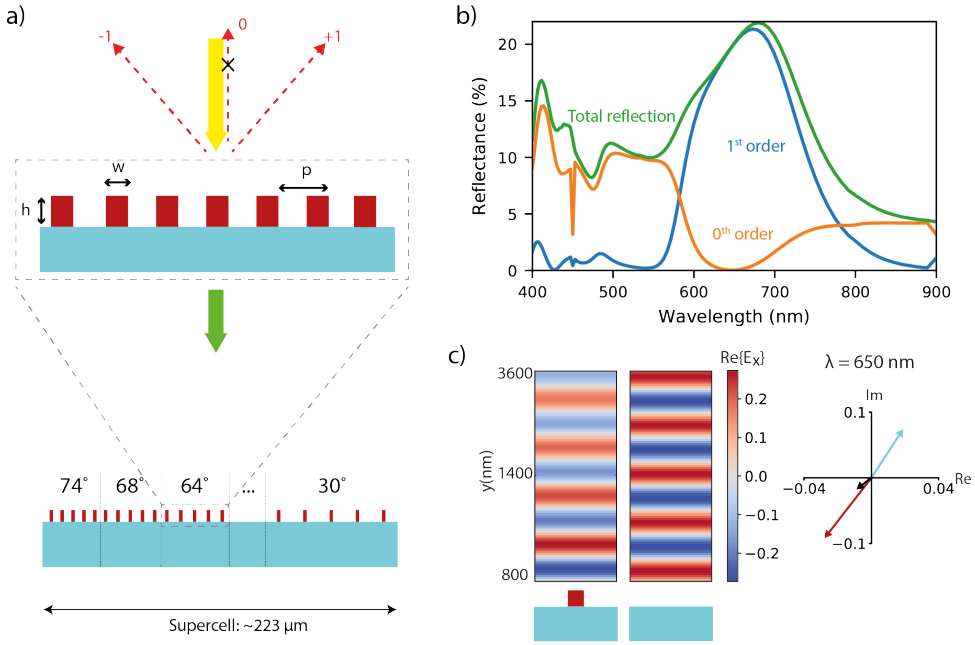

Figure 5.1: Principle of transparent metagrating. a) Top: Schematic overview of a transparent metagrating. Mie silicon nanowire resonators are placed periodically on top of a transparent substrate. The light around the resonance is scattered into diffraction orders. Bottom: Schematic overview of the complete supercell design. 25 metagratings are placed next to each other to form a supercell that reflects light around the resonance wavelength towards an angle range of 30°-75° b) Simulated reflectance of a metagrating of silicon resonators (w = 110 nm, h = 175 nm, p = 900 nm). The total reflectance (green line), specular reflectance (orange line) and diffraction into the first (+1 and -1) order (blue line) are plotted. c) Scattered E field radiated upwards from the single nanowire (left) and field reflected off the sapphire substrate (right) at the wavelength of cancellation λ = 650 nm. Phasor representation of the scattered E field from the nanowire array (red arrow) and the substrate (light blue arrow), and their sum (black arrow).

5.2. Theory and design

In this section, we introduce the concept of a Mie-resonant metagrating and outline how to leverage its properties to tailor at will the spectral and angular response of the metasurface. Specifically, for rooftop PV applications, we design the response to correspond to a Lambertian angular profile spectrally peaked in the red portion of the visible spectrum. Different from previous approaches [91], the Mie-resonators are placed on a transparent substrate such that only the resonant portion of the spectrum is reflected, while the transmitted light can be conveniently collected by a solar cell (see Figure 5.1). Upon excitation of Mie resonances, high-index dielectric nano-antennas can strongly scatter the incoming light [41, 44, 51]. In particular, here we exploit the modes sustained by NWs made of silicon, taking advantage of its high refractive index. The scattering unit cells of the metasurface are composed of Si NWs of height h = 175 nm and width between w = 100-120 nm on a sapphire substrate. The resonant wavelength of modes supported by such a high index scatterer can easily be tuned by changing the size of the scatterer, thus enabling spectral control. Details about the scattering cross section of the single Si NW are given in the SI. In this work the metasurface is designed to scatter light within a narrow bandwidth around λ = 650 nm.

Next, the Mie scatterers are placed into an array with periodicity p, such that first-order diffraction in air occurs while the second order is still evanescent. This is the case for periodicities in the range 650 nm < p < 1300 nm, according to the grating equation for normally incident light $p\sin(\theta_m) = m\lambda$, where θ_m is the angle at which light is diffracted, m is an integer denoting the order of diffraction and λ is the wavelength of the incident light. In this work, as light is normally incident on the grating, two symmetric 1^{st} (+1 and -1) diffraction orders exist that we refer to as 1^{st} orders from now on. Figure 5.1b shows the simulated [92, 93] reflectance spectrum of a single grating with pitch p = 900 nm, where the unit cell is composed of a single Si NW (w = 110 nm, h = 175 nm) on sapphire and it is illuminated at normal incidence by a plane wave polarized perpendicular to the NW (TE polarized). The reflectance into the 0^{th} and the $\pm1^{st}$ diffraction orders (θ_1=±46.2° at λ = 650 nm) reveals three important features. First, a clear peak around the design resonance λ = 650 nm (~20%) is observed due to resonant excitation of the modes of the Si NWs around this wavelength. Second, another peak around λ = 410 nm is observed (~15%), originating from a higher-order mode excitation. Third, a significant portion of the green and blue spectral range is directly reflected off the sapphire substrate to the 0^{th} order (~10%). It is important to note that most of the reflected light around the resonance is scattered into the 1^{st} orders (20%), while reflection back to the 0^{th} order is suppressed (~2%).

In order to investigate the physical mechanism behind the suppression of specular reflection we use the Total Field Scattered Field method [94]. In fact, light resonantly scattered by the NWs is interfering destructivelylight reflected off the bare sapphire substrate, hence resulting in a suppressed reflection to the 0^{th} order. In detail, for destructive interference to appear the amplitude of the scatteredreflected light from the substrate and theat scattered by the NWs is designed to be equal, while the phase is shifted by π. This cancellation phenomenon is expounded in Figure 5.1c by investigating the scattered fields of the two scenarios. The field scattered by a single NW (left) and that reflected by the sapphire substrate (right) is shown, when illuminated at normal inci-

dence by a plane wave at λ = 650 nm (TE). In the first case, the total field scattered filed approach allows to only look at the scattering contribution of the NW, and not of the substrate. Importantly, only the upward scattering in specular direction is shown here. The outgoing specular reflected field from the bare sapphire substrate shows a clear phase shift compared to the scattered field of the NW. In addition, the phasor representation at a position in the backward scattering direction of the scattered (NWs) and reflected (bare sapphire) fields is shown for λ= 650 nm. In the complex plane the electric field of the scattered light is depicted for both scenarios and allows precise comparison of the amplitude (length of arrow) and phase (angle in complex plane). In detail, for the NW scenario the amplitude was taken from the scattered wavefront of an array of NWs (pitch p = 900 nm), as the amplitude of a single NW is decreasing radially. The phase of the scattered field in backward direction is equal for a single NW or a NW array. Notably, it can be seen that the phase shift is almost π while the amplitude is close to equal at the wavelength of cancellation. The sum of the two vectors (black vector) shows that the cancellation is close to ideal. The reflection from the substrate is thus fundamental to achieve the cancellation in specular direction as discussed in more detail in the Supporting Info (5.4) and also explained in [91].

By considering different pitches, each targeting a different outgoing angle of diffraction, and suitably combining them into a larger supercell, it is possible to design a prescribed overall angular response. A schematic overview of the design, resulting in a supercell that scatters from 30-75° for λ = 650 nm (pitch: 675 – 1300 nm), is presented in the bottom of Figure 5.1a.

In colored PV applications, it is important that a Lambertian reflected angular profile is achieved to perceive a matte appearance [25]. However, in rooftop PV applications this requirement can be relaxed since the metasurface should appear Lambertian red only from an observer on the street. Hence, assuming that the sun is incident normal to the solar cells on a rooftop, we can disregard small diffracted angles in the design. Since common house roofs have an angle of ~40°, the desired angular span of the designed angular response lies in the range 30-75°. Indeed, sunlight that hits the panel perpendicular is scattered towards the field of view of pedestrians on the street. Ideally, the scattering should happen asymmetrically only towards the ground, not towards the sky. This could be realized by employing asymmetric scattering unit cells [76, 95], but has not been center of research in this work. As mentioned before, the overall structure is realized by placing multiple metagratings next to each other, creating a "supercell" array of silicon nanowires with varying periodicities (see Figure 5.1a). Within this procedure, it is also important to take into account the relative area of each metagrating (adjusted by their own efficiencies) in order to properly reproduce the Lambertian intensity distribution in reflection. The total area of the supercell is the sum of all grating areas, and adds up to 223 µm. The specific values of p, w, the total reflection and reflection to the 1^{st} order for individual metagratings and the number of unit cells used in each of the metagratings composing the supercell are summarized in Table 5.1.

5.3. Experiments

In order to experimentally demonstrate the possibility of gaining angular and spectral control via transparent metagratings we fabricated the structure described above and

characterized it optically. Next, we compare the measured data to numerical simulations, and assess the performance of a solar cell with the optimized metasurface integrated into its structure.

5.3.1. Fabrication

The metagratings were fabricated using Electron Beam Lithography (EBL), as described in the following. First, silicon-on-sapphire substrates (500 nm c-Si on 0.46 mm R-plane sapphire, MTI Corporation) were cleaned in base piranha. The silicon layer is etched down to a thickness of 175 nm using Reactive Ion Etching (RIE) using a CHF_3 (15 sccm) - SF_6 (10 sccm) - O_2 (3 sccm) plasma etch. Next, a 50-60 nm HSQ high-resolution negative resist layer was spin-coated on the sample, and baked for 150 seconds at 180 °C. For better conductivity, Electra 92 (AR-PC-5091) was spin-coated on the sample. The substrate was then exposed using a Raith Voyager lithography system (dose of 2.400 μC/cm^2). To obtain a sample that is large enough for optical measurements, the supercell of 223 μm described above is replicated 6 times next to each other, resulting in a 1.35 mm wide field. After e-beam writing, the sample was developed in TMAH for 75 seconds at 50°C. The patterned HSQ is then used as a hard mask to structure the underlying Si layer using two subsequent RIE etching steps. First, the native oxide of the silicon is etched using Cl_2 (60 sccm), then the silicon is etched in a HBr (48.6 sccm) and O_2 (1.4 sccm) plasma at 60°C.

The result of the described fabrication is shown in Figure 5.2. The sample consists of silicon NWs with a remaining HSQ layer on top, on a sapphire substrate. A single NW is depicted in Figure 5.2a and b, showing that the side walls are etched perpendicular to the substrate. The HSQ on top of the nanowire is not removed as this process involves chemical reactions that also react with the sapphire substrate. For better resolution, a layer of Electra 92 (AR-PC-5091) was spin-coated on the sample before imaging. An overview SEM image of the total supercell is shown in Figure 5.2c. The pitch between the wires is decreasing from left (p = 1300 nm) to right (p = 675 nm) and for the complete area of the supercell a good uniformity was achieved. On the right side of the supercell, the beginning of the next identical supercell is visible.

5.3.2. Optical characterization

To distinguish light reflected specularly (0^{th} order) from light reflected at an angle (1^{st} orders), we use an integrating sphere. We measure both the sample's total reflectance and the total reflectance excluding the 0^{th} order. The difference between the two measurements then yields the 0^{th}-order reflection (see Supporting Info (5.4) for a schematic of the setup).

Figure 5.3a shows the measured specular reflectance spectrum, as well as the total reflectance spectrum excluding the specular contribution, which we refer to as scattered spectrum. The latter shows a broad peak centered at of λ = 614 nm reaching 9.9% reflectance. The full width at half-maximum of this peak is around 200 nm, covering the wavelength range of interest for red color perception. At the same time, in the same bandwidth around λ = 614 nm, the 0^{th}-order reflection is strongly suppressed, as desired. Indeed, the 0^{th}-order reflectance is around 8% in the blue wavelength range and decreases to 2% on resonance demonstrating efficient light redirection. Additionally, the

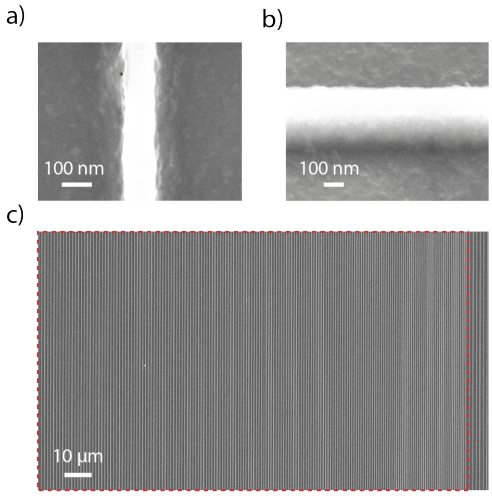

Figure 5.2: SEM image of fabricated metasurface. a) Top-view SEM of a single silicon nanowire of w = 120 nm on top of sapphire substrate b) Tilted image of a single silicon nanowire (tilt angle 45°) c) Top-view of full supercell (dashed red line) containing all metagratings with varying pitch (p = 675 nm – p = 1300 nm). Stitching of two supercells can be seen on the right side of the image.

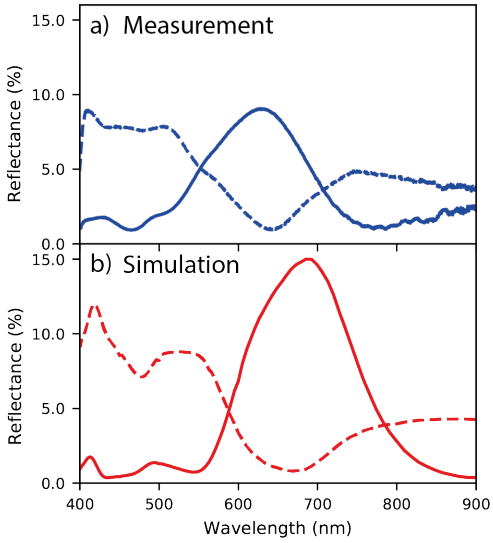

Figure 5.3: Reflectance spectra of full metasurface. a) Measured specular reflectance spectrum (dashed blue line) and scattered spectrum (solid blue line) of full metasurface. b) Simulated specular reflectance (dashed red line) and reflectance for diffraction order (solid red line) of a single supercell. Reflectance is determined by the contribution of the different metagratings in the supercell, weighted by their area respectively.

reflection at wavelengths above the resonance is slightly decreased.

Figure 5.3b shows simulated scattered and specular reflectance spectra. The exper-

imentally measured trends show good agreement with the simulated spectra: a broad peak around 680 nm in the averaged 1^{st} order reflection (average reflectance to 1^{st}–orders: sum of the reflectance from the different metagratings composing the metasurface, weighted by their relative area) corresponds to a clear reduction in specular reflection. The position of the peak can be explained by the combined contributions of the different metagratings (see section 5.4). We ascribe the lower measured reflectance compared to the simulations to fabrication imperfections resulting in silicon NWs with slightly different dimensions, as well as small slanting of the sidewalls which results in a less pronounced resonance [96].

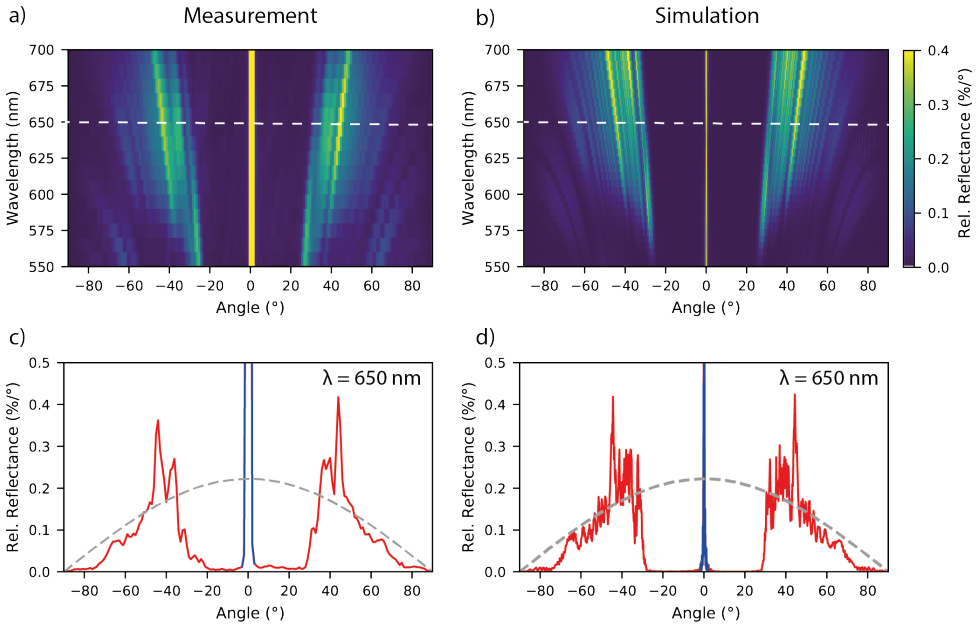

Figure 5.4: Angle-resolved reflectance. a) Measured and b) simulated angular reflectance of full metasurface. White dashed lines indicate cross section of the reflectance shown in c) and d). c) Angular reflectance at λ = 650 nm with specular (blue solid line) and diffracted (red solid line) contributions. The scattering profile of a perfect Lambertian scatterer is plotted as well (gray dashed line). d) Simulated data as in c).

Figure 5.4a shows the angular reflectance as a function of wavelength, measured using a rotating stage setup (see [91] for the description of measurement setup). The measurements were performed in the wavelength range λ = 550-700 nm in steps of 10 nm. First of all, as designed, the sample does not scatter light to angles below 30° and above 75°. As mentioned earlier, the design is optimized to have only the 1^{st} diffraction orders at $\lambda \geq 650$ nm. This can be observed in the measured spectra (Figure 5.4a). For shorter wavelengths $\lambda \leq 650$ nm, 2^{nd}-order diffraction in reflection is noticeable at high angles. Furthermore, following the grating equation, the diffraction angle for each metagrating increases as the illumination wavelength increases. The measurement significantly reflects very similar features in the simulated angular reflectance spectra in Figure 5.4b.

Figure 5.4c shows the measured angular reflectance at λ = 650 nm. The scattered

part of the light is depicted in red, whereas the grey dashed line represents the ideal Lambertian cosine distribution. Experimentally, the angular reflectance follows the desired cosine law rather well for angles in the range 30-75°. The two high reflection peaks at 45° are the result of a non-ideal design ; they are also visible in simulations (see Figure 5.4d and Table 5.1). The blue part of the angular reflectance represents the 0^{th}-order reflection and peaks at 6.8 %/° and 3.0 %/° in experiment and simulations, respectively (out of scale in Figure 5.4c and d). We observe a broader reflection range for the 0^{th} order peak in the measurement compared to that in simulation, due to a difference in binning (0.18° in simulation versus 1.0° in measurement). Overall, we conclude that the experimental results follow the simulation results with a good agreement.

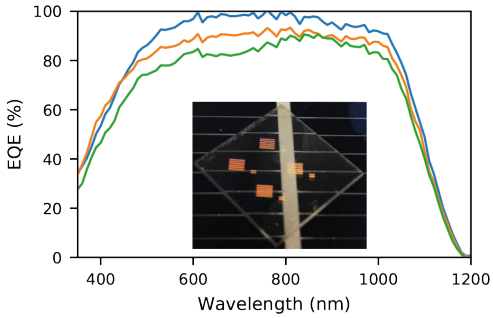

Figure 5.5: External quantum efficiency measurements. Measured external quantum efficiency of bare silicon heterojunction cell (blue line), with bare sapphire on top (orange line) and with metasurface (green line). Inset: Photograph (taken under 45°) of the sample attached to the silicon solar cell using immersion oil. The sample size is 12×12 mm. The four red patches are four metasurfaces with the same underlying design, but fabricated with a slightly different dose during e-beam lithography. On the solar cell silver contact fingers (horizontal grey lines) and a busbar (vertical grey line) can be seen.

5.3.3. Electrical characterization

Next, we apply the transparent metagrating on a Si solar cell. The nanopatterned sapphire substrate was placed on top of a heterojunction silicon solar cell using immersion oil (Fluka 10976, n=1.52) (same setup as in [24]). The cell features a textured front surface and a standard anti-reflection coating. We measured the External Quantum Efficiency (EQE) for three different cases: bare solar cell, cell with clean sapphire substrate and cell with the fabricated metagrating sample (see Figure 5.5). With the sapphire substrate in place, we observe a similar trend as for the bare silicon solar cell, with slightly lower EQE over the whole spectrum. The reduction in EQE is due to reflection of light from the front surface of the sapphire, which is around 8% over the visible wavelength range. The EQE of the cell with the metagrating sample on top is lower compared to the EQE of the cell with sapphire, especially below λ = 800 nm. A closer inspection of the spectrum, shows a reduction of the EQE from λ = 600-800 nm, which is due to the as-designed enhanced reflection shown in Figure 5.3a. The inset in Figure 5.5 shows a photo taken under 45° of the sample placed on top of the solar cell. The bright red rooftop-like colored reflection is clearly visible. In the lower wavelength range, the EQE is reduced due to the higher absorption in the silicon nanowires. This could potentially be reduced by replacing the

silicon with a material with a lower absorption in the visible range (e.g. TiO_2). The measured short circuit current density for the bare silicon solar cell is J_{sc} = 38.9 mA/cm^2. Including the metagrating sample on top slightly reduces the value to J_{sc} = 34.0 mA/cm^2. This implies that to first order the cell efficiency is reduced by relative 13% due to the narrow-angle colored scattering metasurface.

5.3.4. Conclusion

In this work, we experimentally demonstrated spectral and angular control of scattered light using resonant metagratings for colored photovoltaics. Silicon nanowires were fabricated on a transparent substrate and resonantly scatter light around λ = 650 nm. The nanowires were placed in a supercell structure composed of multiple gratings with different pitches, creating a Lambertian scattering distribution with specular reflection nearly fully suppressed and efficient transmission outside the resonant scattering band. The supercell structure was designed to backscatter light within the 30-75° range and experiments and simulations are in very good agreement. The metagratings are integrated with a silicon heterojunction solar cell creating a bright red scattering appearance under a limited range of angles, as desired, and enable seamless integration with roof tile geometries. The external quantum efficiency is only reduced in the scattering spectral band, with a short circuit current drop of only 13%. Potentially, future asymmetric designs can further enhance the efficiency by scattering light only to the ground and not to the sky. The nanopatterned geometries can be readily fabricated and upscaled to practical PV applications with some reinvestment in materials and methods. In particular, the materials used in this work could easily be replaced by more practical materials- For example, the module glass could serve directly as the transparent substrate and any dielectric high index material (polymer, amorphous Si, etc.) for the scatterers. Large-scale fabrication techniques might need further investigation, but promising routes such as spray-coating and substrate conformal imprinting lithography [38] could replace the lab-scale methods.

5.4. Supplementary

5.4.1. Scattering of Mie resonator

Figure 5.6 shows the simulated [92, 93] normalized scattering cross section (optical scattering cross section normalized by the geometrical cross section) for a Si NW of height h = 175 nm and width w = 110 nm on a sapphire substrate, illuminated at normal incidence by a plane wave polarized perpendicularly to the axes of the NW (TE polarization). The peak around λ = 720 nm marks the excitation of the magnetic dipole mode (MD), while higher order modes appear at shorter wavelengths. The inset of Figure 5.6 shows the H field intensity profile at the MD resonance. The resonant wavelength of such modes can be easily tuned by changing the size of the scatterer, thus enabling the required spectral control. Comparing the scattering cross section with the spectrum of reflectance in Figure 5.1b in the main text, raises the question why the reflectance peak is located at 650 nm for the scatterer in a periodic metagrating. The angular radiation pattern of the modes of the single scatterer determines the scattering towards different directions.

However, light can only be scattered to the accessible channels (reflection, transmis-

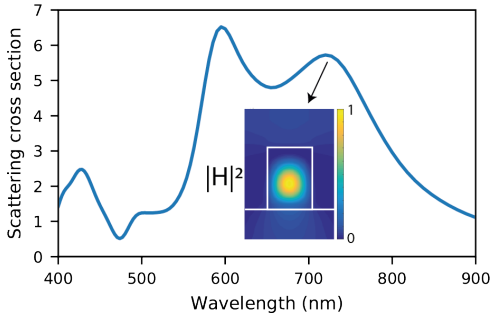

Figure 5.6: Simulated normalized scattering cross section of a single silicon nanowire (w = 110 nm, h = 175 nm) on top of a sapphire substrate. The inset shows the magnetic field intensity profile at the magnetic dipole resonance at 720 nm.

sion, diffraction). The spectrum to those fixed pathways is thus given by the radiation pattern. But there are other effects that have to be taken into account. In the case of this work, the reflection from the substrate cancels the 0 order reflection pathway and the light is thus funneled to the diffraction orders or to transmission, even though the radiation pattern might as well radiate upwards. Also, if the scatterers are getting closer their might be coupling between the particles and new modes appear that can influence the radiation direction. The exact analysis of the modes and their radiation patterns and interaction is beyond the scope of this work. To this end, a particle with resonances in the wavelength range of interest (λ = 630 nm – 670 nm) was taken as a starting point and optimized as unit cell in a metagrating to achieve high diffraction to the 1^{st} order and as such cancellation of the 0^{th} order.

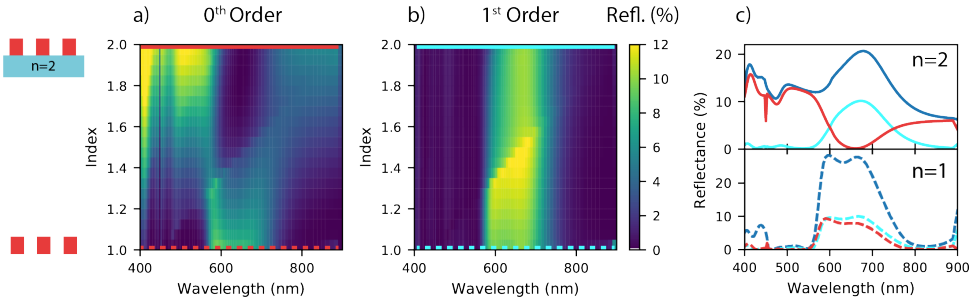

Figure 5.7: Simulated reflectance of a metagrating of silicon resonators (w = 110 nm, h = 175 nm, p = 900 nm) with changing substrate index (n=1-2). Front inset: Schematic of metagrating on a substrate or without substrate. a) Specular reflectance (0^{th} order) and b) diffraction into 1^{st} order. The cyan and red lines indicate the crosscuts of specular reflectance and diffraction plotted in c) respectively. Reflectance above 12% is saturated for better visibility. c) Bottom: The total reflectance (blue line), specular reflectance (cyan line) and diffraction into the first order (red line) of a metagrating without a substrate (n=1); Top: Same as bottom graph, with metagrating on substrate with index n=2.

5.4.2. Metagrating efficiency

As highlighted in the main text, our metagrating design efficiently steers light into the 1^{st} diffraction order by canceling the specular reflection (0^{th} order). This is due to the destructive interference between light directly reflected off the substrate and light that is resonantly scattered by the nanowires. In Figure 5.7, this effect is illustrated by plotting the simulated reflectance of a metagrating while varying the index of the substrate from n=1 to n=2. This in turn modifies the relative contribution between the scattered light and the light reflected non-resonantly from the sapphire substrate. The latter contribution is zero when n=1.

The simulated metagrating is the same as in Fig. 5.1c in the main text (width = 110 nm, height = 175 nm, pitch = 900 nm). As the substrate's index is increased, the relative specular reflectance to the 0^{th} order shows a decrease (Fig. 5.7a) while the diffraction to the 1^{st} order increases (Fig. 5.7b) for an illumination wavelength close to the resonance (λ = 650 nm).

In fact, without the substrate the nanowires scatter isotropically, while introducing a substrate and increasing its index, the specular reflection is suppressed and the diffraction efficiency increases. To corroborate this, we plot the extreme cases of a low and a high substrate index in Fig. 5.7c. With no substrate in place (Fig. 5.7c – lower panel), the reflectance to the 0^{th} order is equal to the scattering towards the 1^{st} order (isotropic scattering). On the other hand, for a substrate with index n=2 (Fig. 5.7c – upper panel), the 0^{th} order reflectance is completely suppressed. In the case of our experiment the substrate is sapphire (index = 1.7) and the 0^{th} order reflection can almost be canceled completely.

5.4.3. Parameter overview

The specific parameters of the metagratings composing the supercell are summarized in Table 5.1

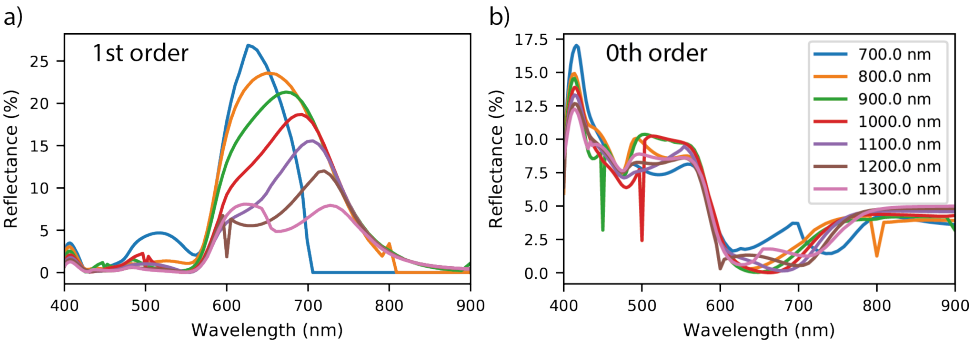

Figure 5.8: Simulated reflectance of metagratings of silicon resonators on a sapphire substrate (w = 110 nm, h = 175 nm, p = 700 nm – 1300 nm) into 1^{st} order and 0^{th} order

pitch [nm]	width [nm]	number of particles	angle [degree]
675	120	6	74
700	120	7	68
725	120	7	64
750	120	7	60
775	120	7	57
800	120	7	54
825	120	8	52
850	120	8	50
875	120	8	48
900	120	9	46
925	120	9	45
925*	120	9	45
950	120	9	43
975	120	9	42
1000	110	10	41
1025	110	9	39
1050	110	10	38
1075	110	10	37
1100	110	10	36
1125	110	10	35
1150	100	10	34
1200	100	11	33
1225	100	11	32
1250	100	11	31
1300	100	12	30

Table 5.1: Overview of design parameters of all metagratings. *The metagrating with a pitch of 925 nm was accidently put twice in the design/fabrication.

5.4.4. Reflectance with changing pitch

The metasurface is composed of metagratings with changing pitch in order to create a large range of diffraction angles as explained in the main text. Every individual metagrating was optimized to highest diffraction in a bandwidth of λ = 630 nm – 670 nm. Metagratings with NWs of the same dimensions (w = 110 nm, h = 175 nm) on a sapphire substrate with a changing pitch (p = 700 nm – 1300 nm) are simulated (Figure 5.8). In figure 5.8a the diffraction for different pitches is plotted. The strength of the reflectance is related to the strength of the scattering of the unit cell. Consequently, with increasing distance between the scatterers the overall reflectance is decreasing and so is the diffraction. In the supercell the peak of reflectance lies at 680 nm, which stems from the combined diffraction spectra of the different metagratings (See Figure 5.3). In the 0^{th} order reflectance it can be seen that the minimum does not change much between the different pitches. This is due to the fact that the cancellation process is mainly driven by the interference with reflectance of the substrate and does not change much between

different pitches.

5.4.5. Analysis of angle of incidence

The metasurface was optimized for normally incident light. As the position of the sun is changing along a day, it is important to study the operation of the metasurface with changing angle of incidence. In Figure 5.9a, the simulated angular reflectance of the full metasurface is shown with angles of incidence between 10 – 45°. For a wavelength of λ = 650 nm the angular scattering still follows the desired cosine distribution (grey dashed line), however, with a changed range of angles that depend on the change in diffraction orders. At higher angle of incidence, the metasurface supports as well 2^{nd} order diffraction at 650 nm that contribute to a wide range of reflected angles.

Next, the reflectance of a metagrating with a pitch of p = 900 nm, with the same angles of incidence as in Figure 5.9a between 10-45°. For small changes (around 10°) the resonant reflectance of the design is pretty stable. For higher incoming angles (20°) the resonance seems to disappear, but the cancellation process of the specular reflection is still efficient. For higher angles (30 and 45°), the reflectance peaks again around 700 nm, and specular reflection is still canceled. As mentioned earlier, the precise change of modes is out of the scope of this study. However, the arguments for the cancellation process still hold for different angles of incidence.

5.4.6. Integrating sphere measurement setup

We measured the scattering of the sample using an integrating sphere. There are two methods of measurements; either to measure the total reflection (Figure 5.10a; specular reflection plus all diffraction orders) or only the diffraction (Figure 5.10b; no specular reflection). For the first method, the conventional setup of the integrating sphere is used. The sample is tilted at the back of the sphere, such that all reflection is collected by the detector. In the second method the sample is placed perpendicular to the incoming light at the back of the integrating sphere. In the latter case, the specular reflected beam can escape from the front opening of the sphere, and only scattered and diffracted light is collected by the spectrometer. The specular reflectance shown in Figure 5.3a of the main text is determined by the subtraction of two measurements by the two different methods; the diffraction measurement is subtracted from the total reflectance. For the scattered spectrum in that same Figure the second method of the setup was used.

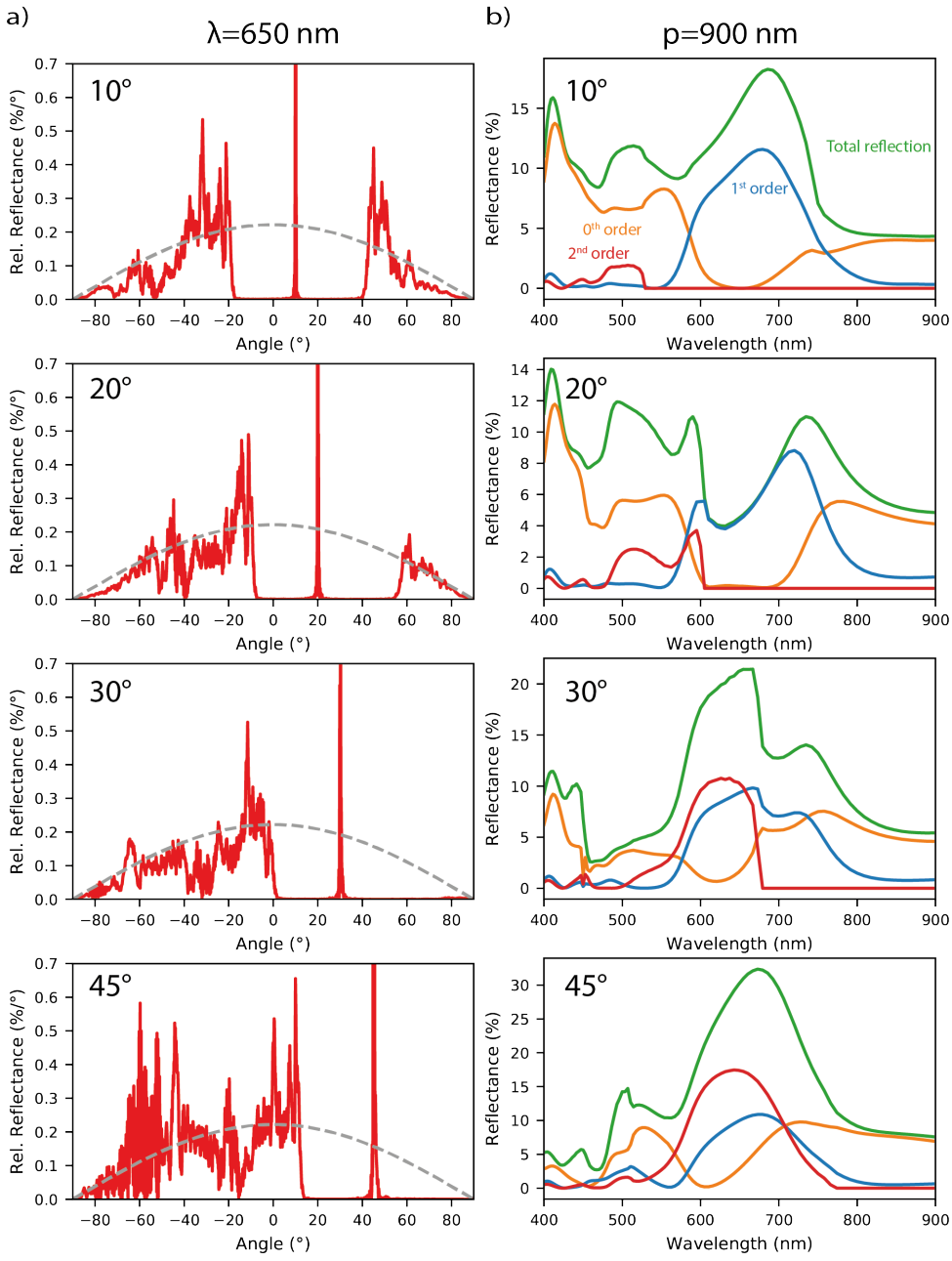

Figure 5.9: Analysis of changing angle of incidence a) Simulated angular reflectance at $\lambda = 650$ nm of full metasurface for angles from 10° - 45°. b) Simulated reflectance of metagrating as in Figure 5.1 c) with changing angle of incidence from 10° - 45°. The total reflectance (green line) is composed of specular reflectance (orange line), 1^{st} order diffraction (blue line) and 2^{nd} order diffraction (red line).

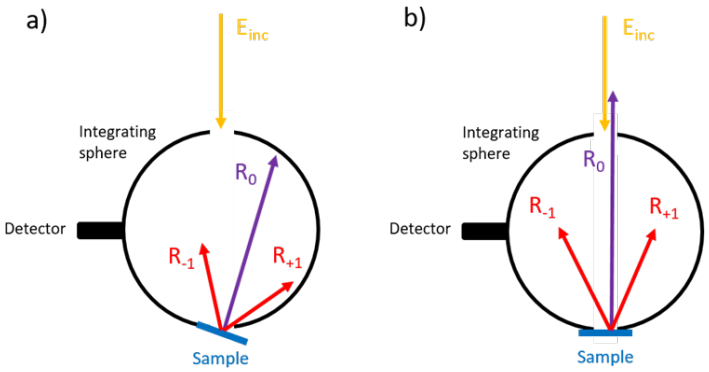

Figure 5.10: Integrating sphere setup a) Configuration with tilted sample; all scattered light is collected. b) Configuration with sample perpendicular to incoming light; specular reflection is not collected.

6

Visible light, wide-angle graded metasurface for back reflection

There's a rhythm and rush these days
Where the lights don't move and the colors don't fade

Stay alive – José González

Metasurfaces, or phase-engineered quasi-2D interfaces, enable a large degree of control over the reflection, refraction and transmission of light. Here we demonstrate the design and realization of a visible light gradient metasurface tailored for highly efficient back reflection based on the Huygens–Fresnel principle. The metasurface emulates the functionality of a Littrow grating, capable of efficiently channeling light into the first negative Floquet order over a broad angular range and bandwidth at visible frequencies. Our theoretical results predict unitary efficiency for extremely low profiles and an optical response that is robust against discretization and design modifications. The experimentally realized metasurface is comprised of high-index TiO_x nanowires over a protected Ag mirror, enabling back reflection with efficiency above 85% in the visible range, close to the reflectivity of the bare silver mirror. The presented analytical design methodology and the resulting low-profile device are advantageous compared to conventional gratings, while offering broadband efficiencies over a range of incidence angles.

6.1. Introduction

Gradient metasurfaces have started to significantly influence modern optical technology as they offer the possibility of replacing a wide range of bulky optical components with low-profile and low-loss patterned surfaces [97–100]. Graded metasurfaces rely on nanostructured surfaces with controlled variation of their transverse impedance, enabling a plethora of operational possibilities, including anomalous wave refraction and reflection [101, 102], holography [103, 104], cloaking [105–107], focusing and beam shaping [101, 108], polarization management [65, 109], and nonreciprocal beam control when combined with time modulation [110, 111]. The nanoscale control of strong wave-matter interactions in metasurfaces has opened remarkable opportunities for low-loss, integrable planar optics [98]. In contrast to other ultrathin configurations based on resonantly excited elements [112–116], gradient metasurfaces typically rely on the response of a combination of non-resonant scatterers and their tailored arrangement, enabling this class of metasurface to support inherently broadband and robust optical responses which are resilient to losses [109]. In this work, we apply the concept of graded metasurfaces to design broadband back reflectors, based on distributed surface impedances. Back reflectors are a class of periodic structures that are specifically tailored to funnel the incident energy into the first negative order Floquet harmonic. These structures are traditionally implemented using binary patterns over finite thicknesses [114, 117–119], which typically need to be optimized to maximize the coupling efficiency to the backward Floquet order [119, 120]. Here we use an alternative method based on the Huygens–Fresnel principle to define the ideal surface impedance profile of ultrathin metasurfaces that enables arbitrary negative reflection. The ideal operation of the designed surface is achieved by controlling the required secondary scattering sources on the metasurface to reconstruct the desired Floquet order. This approach offers flexibility in design, avoiding the need for optimization or specific material parameters, and enables high back-reflection efficiencies over the desired range of angles of incidence (AOI), angles of reflection and frequency. In order to validate our theoretical approach, we employ high-resolution nanolithography to experimentally implement a back reflecting graded metasurface that operates in the visible range.

6.2. Results and discussion

First, we focus our study on the design of an ideal gradient metasurface that reflects all the impinging energy back to the source for a specific frequency and angle for linear polarized light; essentially operating as a zero-thickness Littrow grating. This functionality is equivalent to an ideal retroreflector for this frequency and AOI (Fig. 6.1A shows the concept and a schematic of the fabricated structure). While an ideal homogeneous mirror (Fig. 6.1B) reflects the impinging light towards the specular direction due to momentum conservation, this ideal metasurface with a tailored gradient of the reflection phase (Fig. 6.1C) can impart a suitable additional negative transverse momentum to the impinging wave and reflect the entire impinging light flux back to the source.

Following the approach introduced in [101, 108], and tailored to efficiently manipulate reflected beams in [109], we derive in the Methods section (6.4.1) the analytical expression of the local reflection coefficient that an ultrathin metasurface needs to sup-

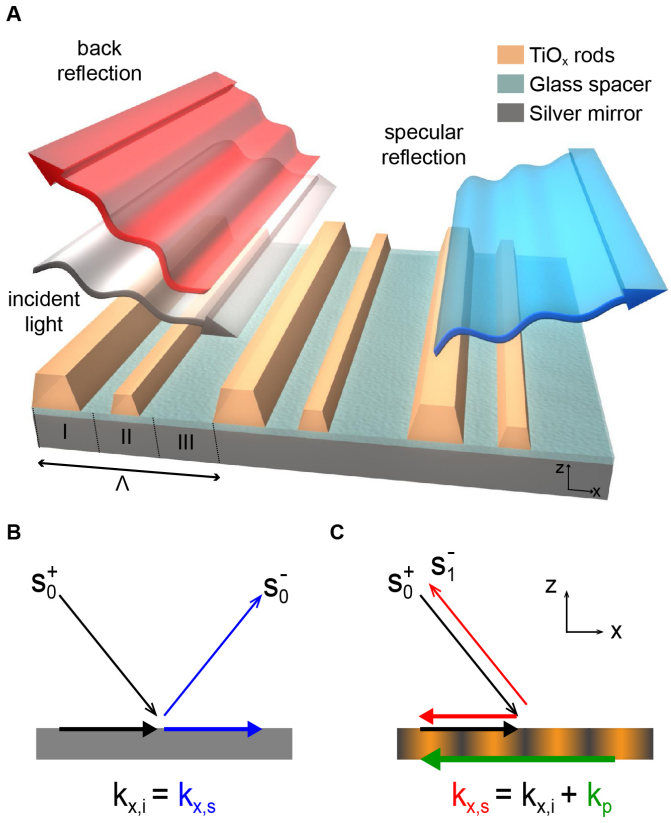

Figure 6.1: Operation principle of a metasurface back reflector. (A) Schematic illustration of back-reflection from a gradient metasurface. (B) Representation of specular reflection from an ideal mirror: incident light (s_0^+, black) is specularly reflected (s_0^-, blue) from an ideal mirror due to momentum conservation at the interface. (C) Scattering channels for reflection from a gradient metasurface: incident light is reflected back (s_1^-, red) toward the source due to the transverse momentum imparted by the inhomogeneous interface. The additional negative momentum k_p (green) is introduced by a tailored gradient of the reflection phase. Momenta in the x-direction are shown by $k_{x,i}$ and $k_{x,s}$ for incident and reflected waves, respectively.

port in order to achieve single-angle retroreflection with unity efficiency for illumination angle θ_0 in the $x-z$ plane, where $\hat{z}$ is the direction normal to the surface:

$$r(x) = \frac{-1+\cos\theta_0 - e^{\frac{2i\pi x}{\Lambda}}(1+\cos\theta_0)}{-1-\cos\theta_0 + e^{\frac{2i\pi x}{\Lambda}}(-1+\cos\theta_0)} \tag{6.1}$$

The required reflection coefficient is unitary all across the surface, implying that it can be achieved with a fully passive interface with inhomogeneous phase profile $\varphi(x)$, shown in Fig. 6.2A for $\theta_0 = 35.7$ degrees, with period $\Lambda = \frac{\lambda}{2\sin\theta_0}$, where λ is the wavelength of operation in free-space. In general, the optimal reflection coefficient of a gradient metasurface may also involve local amplitude modulation [121]. At the retroreflection angle, however, the exact impedance matching between the incident and scattered

beam guarantees that 100% wave conversion is accessible using a purely lossless surface profile, as described by the local phase variations in Eq. 6.1. This nonlinear phase profile exactly compensates for the momentum mismatch between the incoming and the desired retroreflected waves (Fig. 6.1C). For values of incident wave different from θ_0, the reflected wave does not align with the incident wave and the structure operates as an ultrathin back reflector, redirecting light back into the half-space of incidence. Compared to previous attempts to realize highly efficient back reflecting gratings, this approach is fully analytical, where calculations based on the Huygens–Fresnel principle allow us to engineer the scattering pattern over an infinitesimally thin surface at will, and without requiring iterative optimization [68, 121]. For instance, the surface may be equivalently designed to couple a desired portion of the impinging power toward the specular reflection, and the other portion toward back reflection. This concept is also fully extendable to two-dimensional surfaces and arbitrary polarization control.

For an ideal continuously modulated metasurface with a local reflection given by Eq. 6.1, given the periodicity of the modulation the reflected power can couple to only two propagating diffraction orders, the specular reflection s_0^- and the first negative Floquet order s_1^-. The numerically calculated coupling efficiency to these orders as a function of illumination angle is shown in Fig. 6.2B for the surface with phase profile in Fig. 6.2A (see Supplementary Note 1 (6.5.1)). As expected, we obtain 100% coupling efficiency at $\theta_0 = 35.7$ degrees (the design angle), i.e., $s_1^- = 1$. For this AOI, the metasurface operates in the Littrow configuration and the angle of reflection equals 35.7 degrees. In addition, the figure shows that the angular response is robust. For an AOI range $11 < \theta_{in} < 80$ degrees over half of the incident power is redirected into the non-specular direction, despite these angles residing outside of the Littrow design parameters. This broad angular response is associated with the fact that the momentum imparted by the surface does not change with the incidence angle [101], and it is sufficiently negative to ensure that the angle of the emerging reflected beam stays negative over a broad angular range. In general, the attainable angular range may be further increased by designing the retroreflection angle close to 45 degrees. The back reflection angle varies as a function of impinging angle following the grating equation for first-order diffraction $\theta_{back} = \arcsin(\sin\theta_{in} \pm \frac{\lambda}{\Lambda})$, where the $\pm$ sign refers to $\theta_{in} > 0$ and $\theta_{in} < 0$ respectively, as plotted in Fig. 6.2C. The lower cut-off for $\theta_{in} = 11$ degrees is simply determined by the cut-off of s_1^- for close-to-normal incidence, and it can be adjusted by design.

An interesting feature evident in Fig. 6.2B is the perfectly symmetric response of the back reflective surface. The symmetry arises despite the fact that the geometric profile of the surface, described by Eq. 6.1, is asymmetric and tailored for a specific oblique illumination. This symmetry is a general result stemming directly from reciprocity [122, 123], and it is not limited to our particular configuration. More specifically, if the surface is designed to back reflect with x% efficiency for the AOI θ_{in}, it ensures (100-x)% coupling to the specular direction ($\theta_r = \theta_{in}$). Reciprocity then ensures that, when the direction of illumination is flipped and the surface is illuminated from the specular direction, exactly (100-x)% of the power can be coupled back towards θ_{in}. The remaining x% of the power must be scattered through the only remaining scattering channel which is the corresponding back reflection. Given that the period is unaffected by the incidence direction, and it is designed to admit only two diffraction orders, all remaining energy (x%)

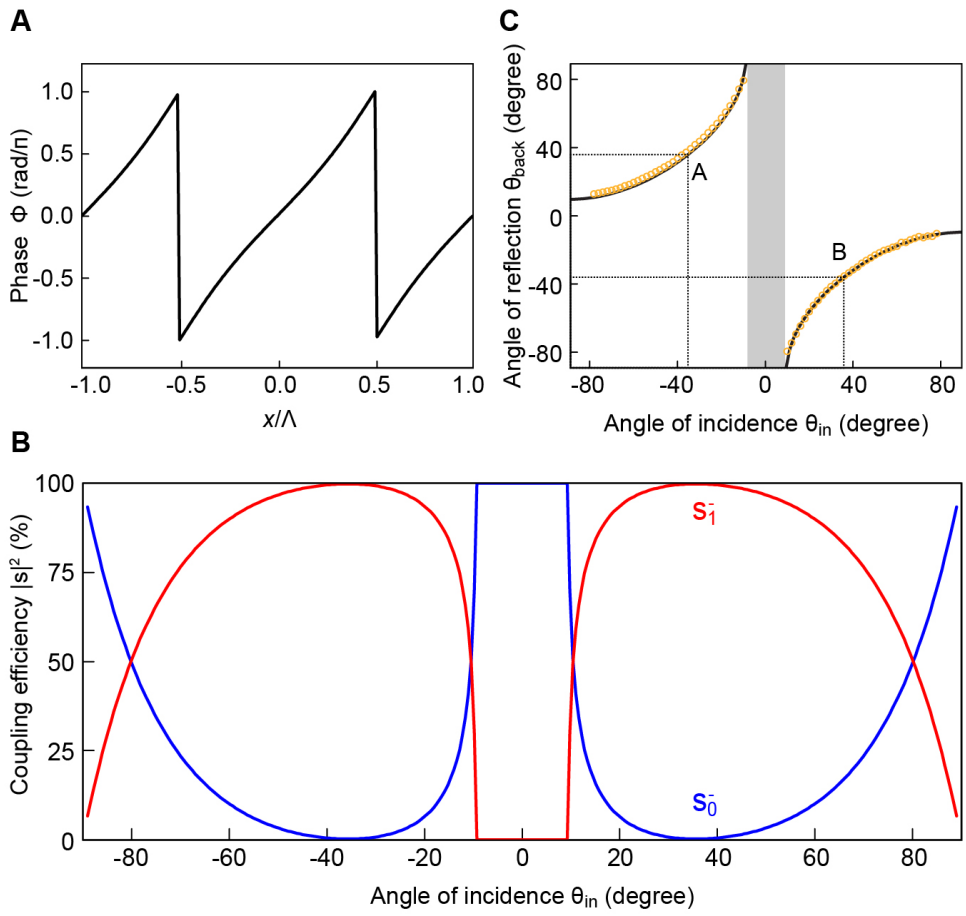

Figure 6.2: Wide angle operation of an ideal back-reflector metasurface. (A) Calculated local phase profile of the ideal surface $\Phi(x) = \angle(x)$, designed for retroreflection at AOI $\theta_0 = 35.7$ degrees following Eq. 6.1, with a surface period $\Lambda = \lambda/(2\sin(\theta_0))$. (B) Numerically calculated coupling efficiency of the ideal surface in panel (A) for different incident angles and for s-polarized illumination. Blue and red curves show the percentage of power coupled toward the specular direction (s_0^-) and first diffraction order (s_1^-), respectively. (C) Calculated (solid black line), and measured (yellow circles) angular dispersion of the gradient surface for the ± diffraction orders. The black lines correspond to the ideal surface in panel (A) and the yellow circles are analogous results measured at $\lambda = 700$nm for the fabricated sample. A and B correspond to the ideal retroreflection points where $\theta_{back} = -\theta_{in} = \pm 35.7$ degrees (Littrow configuration). Inside the highlighted gray region, the non-specular diffraction orders are evanescent.

will be coupled to the back reflected beam. Thus, the blue curve in Fig. 6.2C is center-symmetric and with the broad angular response in the negative half plane, reciprocity ensures an equally broad response for positive incidence angles.

The properties described so far are desirable from a practical standpoint, indicating that there is no trade-off between directionality and efficiency in the proposed metasurface, and back reflection can be achieved over a broad range of angles, even far from

normal incidence. This property also suggests an interesting possibility for applications in the retroreflection industry. While the designed surface is not a true retroreflector, for detectors using narrowband illumination and a relatively wide collection aperture this surface may reflect nearly all of the impinging energy back to the source. Another interesting application of this surface might be replacing the diffusive retroreflective tapes (over a limited angle), as the efficiency of reflection is significantly larger than available reflective tapes and the metasurface can be tailored to operate for extremely broad AOI range [124].

In order to practically realize the proposed metasurface we need to discretize the ideal phase profile (Eq. 6.1). Assuming an equal discretization of the ideal phase profile into N phase steps, the coupling efficiency to the retroreflected order gets closer to 100% as the number of steps increases (Supplementary Note 2 (6.5.2)). Interestingly, even a coarse discretization with only two discretization steps yields a retroreflection efficiency larger than 75%. The reason behind this robustness is again associated with the nature of our design. First, the diffraction phenomenon is non-resonant and therefore inherently robust to perturbations. Second, the period Λ determines two propagating diffraction orders for the operational frequency ensuring that, as long as the overall phase gradient along each unit cell suppresses the coupling towards the zero-th order diffraction (specular reflection), reflection will be funneled towards the first order in the back direction.

The ultrathin profile of the designed surface provides an ideal platform for microwave or terahertz graphene-based metasurfaces which are inherently deeply subwavelength. Here, we chose to realize the device characterized in Fig. 6.2A using a nanostructured dielectric metasurface operating in the visible spectrum (Fig. 6.3A-B) with subwavelength thickness t = 100nm, made of TiO_x trapezoidal bars on top of an Ag mirror via e-beam lithography and evaporation (see Methods for a description of the fabrication process (6.4.3) and Fig. 6.1A for a schematic of the fabricated structure). The dielectric nature of TiO_x and its relative high index (n=2.35 for λ = 500 nm to n=2.23 at λ = 1000 nm), are suitable to minimize absorption and provide reasonable phase control over a relatively small thickness [125]. We designed the structure with three phase discretization steps, N = 3, for operation at λ = 700 nm , tailored for s-polarized excitation (Electric fields lies in the metasurface plane). The variation of the local reflection coefficient in the first two elements is achieved by controlling the geometry of the nanorods. The third segment consists of the bare back-mirror (Fig. 6.3A).

The fabricated structure was excited with a weakly converging beam such that the excitation angle was well-defined. The reflected intensity was measured using an optical power meter (see Methods section (6.4.4) for more details on the measurement). The sample was mounted in the center and the power meter on the outer ring of a rotating stage, while the illumination direction was held constant. This enabled independent control of excitation and sampling angles, as depicted in the schematic of the measurement setup in Fig. 6.3C. We chose Λ = 600 nm (605 nm in the fabricated surface) to enable efficient back reflection in the free-space wavelength range λ = 490 - 940 nm.

The previous analysis ensures that an efficient back reflector can be implemented over a deeply subwavelength thickness. At shorter wavelengths, and specifically over the visible spectrum, current nanofabrication techniques limit the accessible resolution and accuracy of sub-hundred-nanometer features. To reduce the sensitivity of the device to

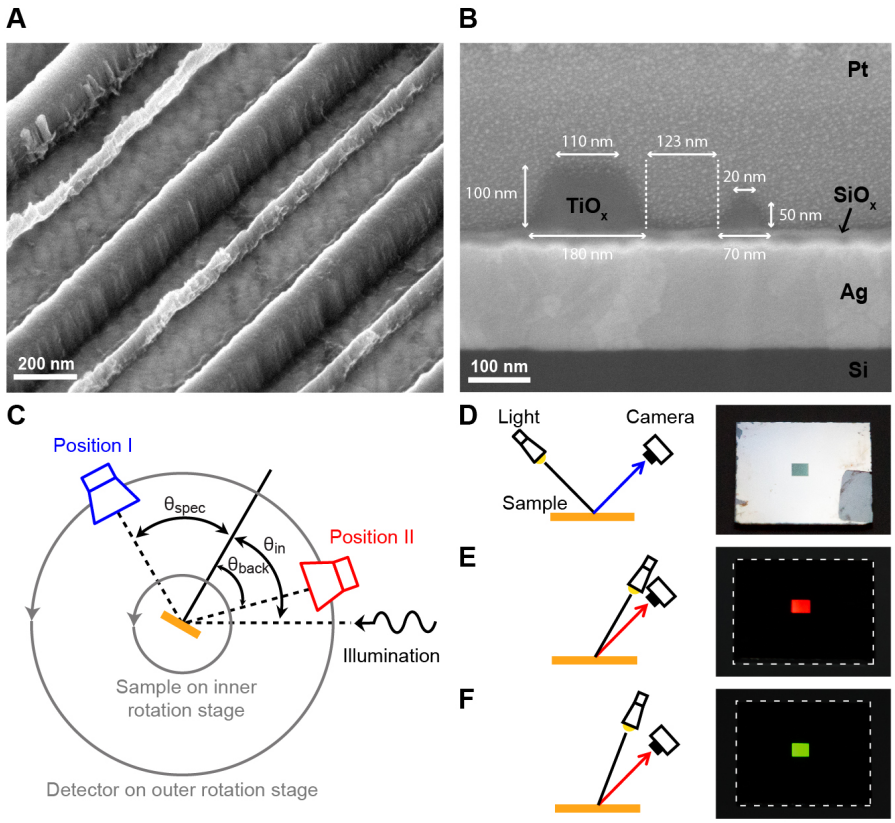

Figure 6.3: Fabricated structure and measurement setup. (A) SEM image (top view, under 40% tilt) and (B) cross section of the fabricated sample with extracted dimensions of the device. One unit cell of the structure is composed of three regions: two TiO_x nanorods and the bare mirror. See Methods section (6.4.3) for detailed geometry information. The Pt layer on top of the sample was added in the cross-section fabrication process to get a clean cross-section. (C) Schematic of the measurement setup: θ_{in} can be changed by rotating the sample on the inner rotation stage while the illumination arm is kept fixed. The coupling intensity to the different diffraction orders is measured by independently rotating the detector on the outer rotation stage to positions I to measure θ_{spec} or position II to measure θ_{back}. Illumination and detection planes are slightly tilted horizontally to allow retroreflection measurements without blocking the illumination. (D – F) Photographs of the fabricated structure on the right (1.5x1.5 mm^2 square in the center of the 12x12 mm^2 silver mirror, bare Si residual from fabrication process in the lower-left corner) and schematic of photography setup on the left. Panel (D) shows the specular response under illumination from the back with a commercial flashlight: no light is reflected in the specular direction from the structure (dark square in the middle). Panels (E – F) show efficient back reflection of the sample when illuminated with a white light lamp for different angles. The angle between light and camera was increased in (F) compared to (E).

nanofabrication errors we chose a thickness of t = 100 nm for the surface. The efficient operation of our fabricated sample from the practical observer standpoint is visualized in Fig. 6.3D–F. Photographs of the sample can be seen next to schematics of the photography setup. In Fig. 6.3D the bright specular reflection of the Ag mirror around the structure is visible while the dark square in the middle of the sample where the metasurface is placed indicates that specular reflection is almost absent. In contrast, the center of the sample is noticeably bright for an observer sitting close to the excitation source, as can be seen in Fig. 6.3E-F for different incoming angles. The bright color that can be observed in back-reflection depends on the angle of observation and illumination. As we mentioned previously, these pictures also indicate the possibility of utilizing these surfaces as efficient ultrathin retroreflectors for AOI close to the retroreflection angle. In this case, while the observable color of the reflected wave varies, the mirror covered with the designed metasurface is noticeably brighter than a conventional mirror.

The optical response of the fabricated sample is quantitatively demonstrated in Fig. 6.4. Symmetric scattering resulting from reciprocity permits a complete characterization of the device while scanning only half the angular range (Fig. 6.4A). However, to confirm the theoretical results we performed measurements over the full range of angles. In the figure, we compare the specular reflection to the measurements obtained using a flat silver mirror, similar to the ground plane utilized in our device, allowing a direct comparison that provides a quantitative calibration of the measured efficiency. The grey circles in Figure 6.4A present the measured angular response of the silver mirror when illuminated with s-polarized light at λ = 700 nm. We observe that around 10% of the incident power is lost, either through absorption or diffuse scattering. The measured response of the silver mirror is slightly lower than simulated reflectance using the tabulated dielectric response of single crystalline silver (Fig 6.4A). This difference is attributed to nanoscale surface roughness resulting from evaporation and other fabrication defects.

The level of back reflection of our sample is shown with red circles in Fig. 6.4A, demonstrating that most of the scattered light is indeed efficiently back reflected. The specular reflection thus significantly drops over a wide angular region around the retroreflective angle θ_0 = 35.7 degrees. The scattered power is focused toward the backward diffraction channel (s_1^- in Fig. 6.1C), yielding a coupling efficiency of 88% under illumination at θ_0 = 35.7 degrees, and with less than 10% of the impinging power being absorbed or diffusely scattered at the design frequency under illumination from all angles, except around the Wood's anomaly, consistent with the absorption levels obtained from the bare silver back-mirror. We note that the presence of the plasmonic mirror creates additional absorption at the metal-dielectric interface. For applications requiring the highest efficiencies, such as pulse shaping, stretching, and compression, the Ag mirror could be replaced with an optimized Bragg reflector.

Although the metasurface was originally designed for AOI of 35.7 degrees, increasing the incidence angle toward grazing angles does not significantly affect the overall efficiency and up to a remarkably large angle $|\theta_{in}|$ = 75 degrees, at λ = 700 nm the dominant portion of the scattered power remains in the same half-plane of the incident wave. For illumination at angles less than $|\theta_{in}| < 9$ degrees, the second scattering channel is non-radiative for λ = 700 nm , and thus it is not excited (Fig. 6.2C). Over this range, the metasurface operates as a simple mirror, as observed in Fig. 6.4A. For comparison, the

solid lines in Fig. 6.4A also show the calculated coupling to the two scattering orders obtained using full-wave simulation for a structure with the same geometry as the fabricated device (See Methods section for details about simulation (6.4.2)). The simulated results agree well with our experiment, even though a slightly lower cut-off at large angles is observed in the measured data compared to the calculated curves. This is due to the small size of our sample, as the area where the measurement beam hits the structure increases with higher incoming angles and exceeds the structure area for $|\theta_{in}| > 60$ degrees. In this angular range, part of the light is specularly reflected from the bare mirror adjacent to the metasurface.

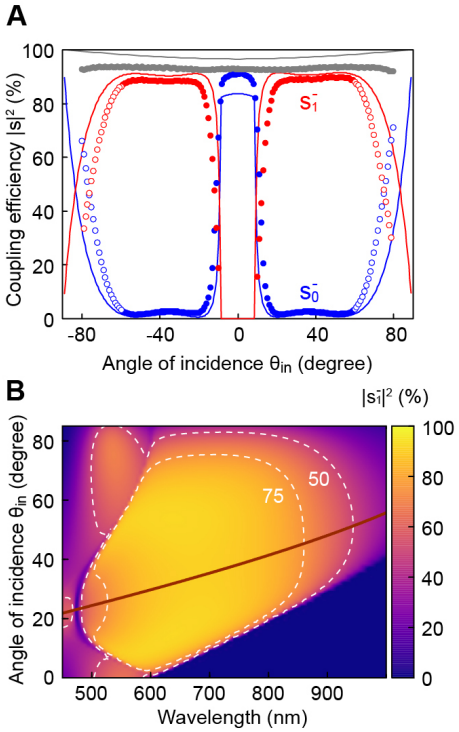

Figure 6.4: Back-reflection response of the fabricated device. (A) Angular response at λ = 700 nm. Comparison between measurements (circles) and numerical simulations (solid lines). Coupling efficiencies for the specular reflection s_0^- and the first-order negative reflection s_1^- , are shown with blue and red colors, respectively. The empty circles indicate reflection measurements for angles above $|\theta_{in}| = 60$ degrees, for which the spot size of the beam exceeds the structured area and part of the beam is specularly reflected by the mirror next to the structure. The measurements and simulations of the bare mirror are depicted in grey. The homogenous surface supports specular reflection with approximately 10% absorption across all angles. (B) Numerical simulation results of the angular/frequency dispersion of the structure with the fabricated dimensions, showing the coupling efficiency toward the first-order negative reflection s_1^- and highlighting the 75%-power and 50% - power operation regions. The dark red line indicates the ideal retroreflective loci (Littrow configuration), for which the incoming and the reflected wave are aligned. More than 50% back reflection is achieved across λ = 490-940 nm and θ_{in} = 24-51 degrees.

A remarkable property of the back reflecting metasurface consists in its broadband

operation, which is attributed to the inherent stability of retroreflection as well as non-resonant nature of the involved scattering phenomenon, based on the phase gradient imposed through the metasurface. While the surface impedance of the trapezoids is expected to change over frequency, its relative slope across each unit cell is not significantly affected by frequency variations, ensuring that the net momentum imparted to the impinging wave still funnels most of the energy back to the first negative diffraction order. To further investigate this property, we determined the amplitude dispersion of the coupling to the two scattering modes for a structure with the dimensions of the fabricated device through full-wave simulations for all incident angles. As expected, the designed metasurface operates over an extremely broad half-power wavelength range λ = 490-940 nm in terms of single-angle retroreflection efficiency. We verified our simulations with experimental measurements at multiple wavelengths, in addition to the λ = 700 nm case, as reported in the Supplementary Note 3 (6.5.3). It is worth mentioning that the angular range and bandwidth of the grating may be further increased through optimization, however, here we presented a configuration derived directly by our analytical model in Eq. 6.1, also including all fabrication tolerances (e.g. height of second rod is smaller than t = 100 nm). A further discussion of the effect of shape and size of surface elements is given in Supplementary Note 4 (6.5.4).

The response of the designed metasurface is also controllable with the polarization of the incident wave. The surface features utilized for this implementation are inherently anisotropic, as their scattering properties depend on the orientation of the field vectors, and the local reflection phase is approximately constant for p-polarized illumination. Consequently, the surface operates as a simple mirror for this polarization, as discussed and verified in Supplementary Note 5 (6.5.5). In other words, this metasurface selectively reflects in opposite half-planes the two impinging polarizations. We are currently investigating polarization independent designs of back-reflecting metasurfaces based on a similar principle, achieved by considering 2D arrangements of isotropic surface elements [65, 109].

6.3. Conclusion

We have discussed the design principle and advantages in terms of size, simplicity of design and fabrication, bandwidth, acceptance angular range, low-profile and efficiency of gradient metasurfaces for back reflecting surfaces (i.e. ultrathin Littrow gratings). Indeed, we have shown that there is no fundamental limitation on the efficiency or size of a Littrow grating. One of the challenges in experimentally realizing the optimal surface profile derived in Eq. 6.1 is to achieve (semi-) continuous phase variation along the surface, which becomes important for large-angle operation, for which the required impedance profile has faster spatial variations [121]. We have shown here that coarse sampling of the optimal profile provides reasonably good performance over wide angular and frequency ranges at visible frequencies. Possible ways to overcome this limitation and gain higher efficiency (for larger retroreflection angle or more complicated functionalities) is to use Pancharatnam-Berry phase [126], where the local variation of the surface phase is achieved through rotation of a subwavelength nanoantenna. Continuously varying surface elements can also provide a solution to eliminate the requirements on surface discretization [127].

We believe that this approach is an effective replacement of conventional bulky optical elements, particularly for subwavelength gratings used in pulse shaping and spectrum splitting applications. The design is based on the Huygens-Fresnel principle and is scalable over different frequency ranges and may be modified for achromatic retroreflection at multiple frequencies (or AOI) [128, 129]. Similar designs may be explored at radio-frequencies to improve passive and active RFID tags. The control of the angle of reflection may also enable applications for light management in solar cells. The thin metasurface profile opens the possibility of spin coating or evaporating a thin absorber material on top of the metasurface, and broadband enhanced light trapping and absorption [109].

6.4. Materials and methods

6.4.1. Derivation of reflection coefficient

Derivation of the reflection coefficient: Following Huygens–Fresnel principle to achieve the arbitrary scattering field distribution, the electromagnetic boundary conditions of the system in Fig. 6.1C for s-polarized illumination read

$$\begin{aligned} 2\hat{z}\times(\boldsymbol{H}_i+\boldsymbol{H}_s)|_\sigma &= Y_e(x)\hat{y}\cdot(\boldsymbol{E}_i+\boldsymbol{E}_s)|_\sigma \\ -2\hat{z}\times(\boldsymbol{E}_i+\boldsymbol{E}_s)|_\sigma &= Z_m(x)\hat{y}\cdot(\boldsymbol{H}_i+\boldsymbol{H}_s)|_\sigma \end{aligned} \tag{6.2}$$

for any position x on the inhomogeneous metasurface σ, where Y_e and Z_m are the effective surface electric admittance and surface magnetic impedance of the structure [108, 109]. Subscripts i and s indicate the incident and reflected waves, respectively. The local reflection coefficient of the metasurface $r(x) = A(x)e^{j\Phi(x)}$ can be related to the effective properties of the surface for normal illumination as [108, 130]:

$$r(x) = -\frac{2(\eta_0^2 Y_e(x)) - Z_m(x))}{(2+\eta_0 Y_e(x))(2\eta_0 + Z_m(x))} \tag{6.3}$$

Considering plane wave excitation at θ_0 in the $x-z$ plane and ideal operation i.e. unity retroreflection the incident and scattered waves read

$$\boldsymbol{E}_{i,s} = \hat{y}E_0\exp(i(\hat{x}\cdot\boldsymbol{k}_{i,z}x+\hat{z}\cdot\boldsymbol{k}_{i,s}z)); \eta_0\boldsymbol{H}_{i,s} = \boldsymbol{k_{i,s}}\times\boldsymbol{E}_{i,s} \tag{6.4}$$

where $\boldsymbol{k}_i = k_0(-\sin(\theta_0)\hat{x}+\cos(\theta_0)\hat{z})$, $\boldsymbol{k}_s = -\boldsymbol{k}_i$, and k_0 is the free-space wave number. Combining Eq. 6.2,6.3 and 6.4 the local reflection coefficient is found as in Eq. 6.1. Note that the local reflection coefficient is merely a nonlinear phase distribution imprinted on the reflected wave as $A(x) = 1$. The phase profile for an ideal single-angle retroreflector with θ_0= 35.7 degrees is shown in Fig. 6.2A. The local phase profile increasingly deviates from linear distribution for larger values of θ_0 [121].

6.4.2. Numerical simulations

Numerical simulations throughout the paper were carried out by the 2D finite-element software COMSOL Multiphysics in the frequency-domain radio-frequency module. Periodic ports and Floquet periodicity boundary conditions are used to model one unit-cell of each metasurface. Ports are placed far enough from the metasurface such that

all evanescent scattering modes are sufficiently weak. The ideal back reflector characterized in Fig. 6.2 is modelled as a sheet admittance derived in Supplementary Note 1 (6.5.1). The substrate and free space are meshed with maximum element sizes of 2 nm and 26 nm, respectively. Perfect electric conductors are used in the ideal set up.

To model the fabricated device, we used the SEM images in Fig. 6.3A and 6.3B and estimated the dimensions as described in the fabrication process below. All materials are modelled as dispersive and lossy and we used realistic values for the permittivities of silver and SiO_x from experimentally retrieved datasets [131, 132]. For TiO_x, we measured the refractive index for a sample of on a Si wafer by spectroscopic ellipsometry. A maximum element size of 20 nm is used for high-index TiO_x rods and the remaining parts are meshed with a maximum element size of 28 nm. A 200 nm thick silver layer is used as the back reflector which we truncated with a perfectly matched layer to model a semi-infinite ground plane. The scattering parameters of the port are used to calculate the percentage of the power coupled toward each channel.

6.4.3. Fabrication process

A 1-mm-thick Si wafer was coated with 200 nm of Ag and 20-30 nm of SiO_x by thermal evaporation. This protected mirror was then spin-coated with ZEP520a, a high-resolution positive tone resist and Espacer 300z to improve the conductivity of the sample. Then the asymmetric grating was written by E-beam lithography using a 20 keV beam. The patterned area was 1.5 x 1.5 mm^2 square, comprised of stitched 100 x 100 μm^2 write fields. The sample was then rinsed for 30 seconds in water to remove the Espacer, developed in pentylacetate for 45 seconds, rinsed 15 seconds in a mixture of methyl isobutyl ketone and isopropanol (MIBK:IPA,9:1), dipped into IPA and transferred to ethanol. To prevent collapse of the fragile resist patterns the sample was dried at the critical point. The lines were filled with 100 nm of TiO_x by e-beam evaporation followed by lift-off which was done by dissolving the resist for 10 minutes in an ultrasonic bath in anisole. TiO_x was also evaporated directly on a Si wafer to allow a determination of the TiO_x dielectric function using spectroscopy ellipsometry, fitting the data using a Gaussian-Cauchy model. Completed dimensions were measured using a focused ion beam (FIB, FEI Helios Nanolab 600) to cut cross sections, with dimensions measured by electron micrographs. The metasurface consisted of repeating unit cells with a periodicity of 605 nm. The taller line had a height of 100 nm, a bottom width of 180 nm and a top width of 110 nm. The narrower line, separated from the tall line by a gap of 123 nm, had a height of 50 nm with bottom and top widths of 70 nm and 20 nm respectively (Detailed dimensions are shown in Fig. 6.3B).

6.4.4. Details of optical measurement

The coupling efficiency of the fabricated sample to the two orders was measured experimentally using a rotating stage, sweeping the angle of the incident plane wave across θ_{in}= -80 degree to θ_{in}= 80 degree. For illumination, a collimated broadband beam from a laser-driven light source (EQ-99X, Energetiq) was sent through a linear polarizer and then focused onto the sample with a weak lens. The focal point on the sample had a diameter of 0.75 mm. For excitation angles below 60 degrees the focus was smaller than the structure with an area of 1.5 x 1.5 mm^2; above this angle the light beam illuminated

both the structured region and part of the adjacent mirrored substrate. This resulted in measured intensities of specular and first order reflection with a slight contribution from the mirror. The intensity of the scattered power for the allowed scattering modes s_0^- and s_1^- was measured respectively for each degree using an optical power meter (Powermeter PM100USB with Photodiode Power Sensor S121C (Thorlabs)). The reflected beam was focused with a lens on the power sensor. To measure only the frequency ranges of interest an optical filter (either 700 nm, 750 nm or 850 nm center wavelength, 40 nm bandwidth, Andover Corporation) was placed in front of the lens of the power sensor.

6.5. Supplementary

6.5.1. Supplementary Note 1

We implemented the ideal phase profile in Fig. 6.2A following the method described in [109]. The variation in the phase of the local reflection coefficient is realized by varying the surface admittance at a subwavelength distance from a perfect electric conductor (ideal mirror). The obtained surface profile is modelled as a sheet admittance in COMSOL, with $h = \lambda/20 = 35$ nm for the distance between the sheet admittance Y_{surface} and the ground plane. In general, the relation between the local phase and the admittance reads:

$$\eta_0 Y_{\text{surface}} = -i \tan(\Phi(x)/2) + i \cot k_0 h \tag{6.5}$$

where $\Phi(x) = \angle(x)$ and η_0 is the characteristic impedance of free-space.

6.5.2. Supplementary Note 2

With the approximately linear phase profile in Fig. 6.2A, the metasurface performance is expected to be robust to surface discretization. Given that surface discretization is necessary in practical designs, here we investigate retroreflective efficiency (i.e. efficiency in Littrow configuration) for discretized realizations of the ideal surface shown in Fig. 6.2. For the ideal surface complete single-angle retroreflection is achieved for light incident at an angle of $\theta_{in} = 35.7$ degrees, and $\lambda = 700$ nm. The ideal local reflection phase is shown in Fig. 6.2A, and also shown in Fig. 6.5 (blue lines). Each period of the surface is then divided into N segments, and we increase N from 1 to 16. The case N=1 represents a fully homogenous surface and the case N=16 is a finely discretized surface for which the length of each step is 600/16 = 37.5 nm. For comparison, in Fig. 6.5 we also plotted the quantized reflection phase along the surface for the N=4 case. Following Supplemental Note 1 (6.5.1) we have numerically calculated the percentage of power coupled toward specular reflection and retroreflection for each discretization N (Fig. 6.6).

For N=1 the surface is a simple mirror that imprints a constant phase onto the specularly reflected wave s_0^-. Increasing the number of surface segments rapidly increases the power coupled into the first negative diffraction order s_1^-, with only two phase steps required to couple more than 75% of the incident power into this retroreflective order. We note that in this case the metasurface is still symmetric but the excitation asymmetry enforces an asymmetric scattering from the surface. For N=3, which corresponds to our physically implemented surface, a 90% efficiency in a lossless ultrathin structure is predicted. Quite interestingly, in experiments we obtained around 85% efficiency which is

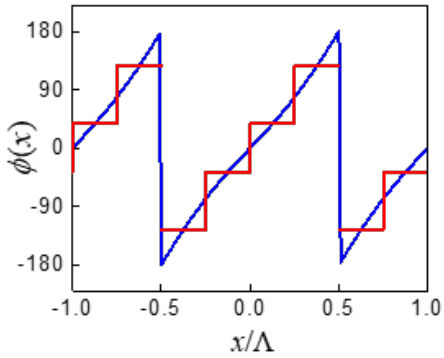

Figure 6.5: Discretized local reflection. Calculated ideal local phase profile of the surface $\Phi(x) = \angle(x)$, designed for an incoming angle of θ_0= 35.7 (blue line), and the discretized reflection profile for N=4 (red line). The surface period is Λ = 600 nm for operation at λ = 700 nm.

consistent with the amount of absorption from the back reflector (see Fig. 6.4A). Beyond this point ($N > 3$) the single-angle retroreflection efficiency is more than 98%, demonstrating the robustness of the metasurface response to surface discretization. For larger retroreflective angles, the optimal phase starts to deviate from linear shape and larger number of discretization are expected to be required.

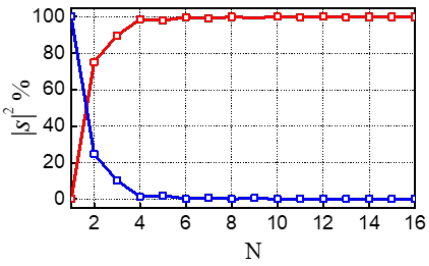

Figure 6.6: Effects of surface discretization. Coupling efficiency of the surface when the ideal continuous profile is discretized into N steps. Blue and red lines correspond to the numerically calculated coupling efficiency for an incident s-polarized wave at θ_{in}= 35.7 degrees, reflecting toward the specular direction (s_0^-) and retroreflection (s_1^-), respectively.

6.5.3. Supplementary Note 3

In addition to the measurements performed at λ = 700 nm on the fabricated sample (reported in Fig. 6.4A in the main text), we verified the broadband operation of the back reflector through analogous measurements at λ = 750 nm and λ = 850 nm. We sweep the angle of the incident plane wave from θ_{in} = -80 degrees to θ_{in} = 80 degrees. The intensity of the scattered power for the allowed scattering modes s_0^- and s_1^- is then measured experimentally as shown schematically in Fig. 6.3C. The results are compared in Figs. 6.7 and 6.8 with full-wave simulations of the metasurface, with dimensions obtained from

the fabricated device.

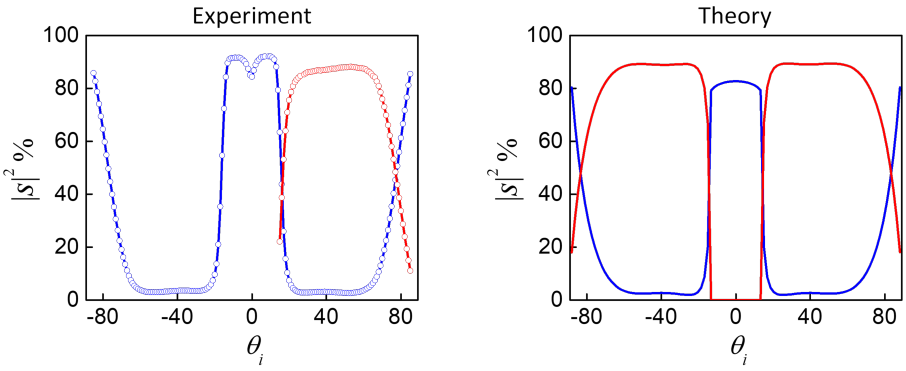

Figure 6.7: Angular response at 750 nm. Coupling efficiencies for the specular reflection s_0^- (blue) and the first-order negative reflection s_1^- (red) are shown: measurement (left) and numerical analysis (right) of the structure with the fabricated dimensions.

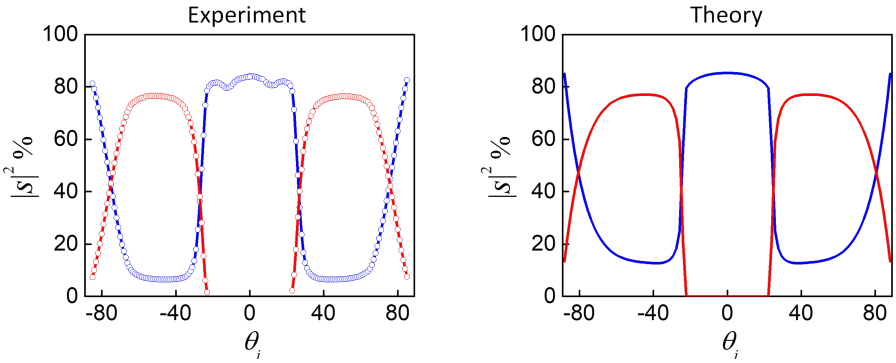

Figure 6.8: Angular response at 850 nm. Coupling efficiencies for the specular reflection s_0^- (blue) and the first-order negative reflection s_1^- (red) are shown: measurement (left) and numerical analysis (right) of the structure with the fabricated dimensions.

At $\lambda = 750$ nm we performed the measurement campaign only for half of the angular spectrum. As we discussed in the main text, reciprocity ensures that the distribution of the scattering amplitudes are symmetric with θ_{in}. The small irregularities observed in the measurement close to normal incidence are associated with polarization impurity of the incident light. Due to non-ideal alignment of the polarizer, the incident beam may contain a small fraction of p-polarized light. The response of the surface for p-polarized illumination is discussed in Supplementary Note 4 (6.5.4).

6.5.4. Supplementary Note 4

In this section and through series of numerical simulations, we study the effect of shape and size of nanorods on the response of metasurface. Fabrication errors may introduce

variations in the width and height of the nanorods and subsequently deteriorate the scattering response of the system. Intestinally, however, numerical simulations show that ±10% variations introduce only minor variations in the back-reflection response and coupling to the first negative order is almost constant (Fig. 6.9). This is consistent with our discussions on the non-resonant nature of the design. Furthermore, the exact shape of the nanorods is not a crucial parameter and the trapezoidal shape is simply chosen to facilitate fabrication process and avoid sharp corners. In this regard, the trapezoidal nanobars are replaced with rectangular bars (with equal mean widths) and the angular response of the system is shown in Fig. 6.10, also demonstrating very robust behavior with respect to the shape of surface elements.

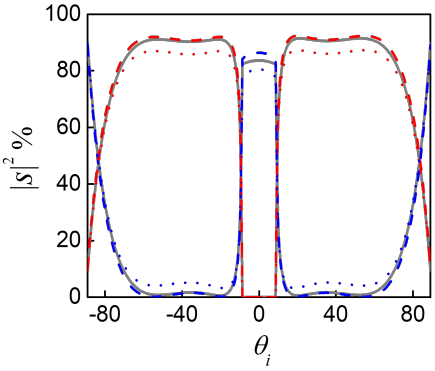

Figure 6.9: Tolerance to variations in the size of surface elements. Scattering response of the system considering +10% (dashed lines) and -10% (dotted lines) variations in heights and widths of surface elements while the period is kept constant. For comparison, grey lines also project the scattering response of the original surface. Specularly reflected power and the first order negative reflection are shown by blue and red colors, respectively.

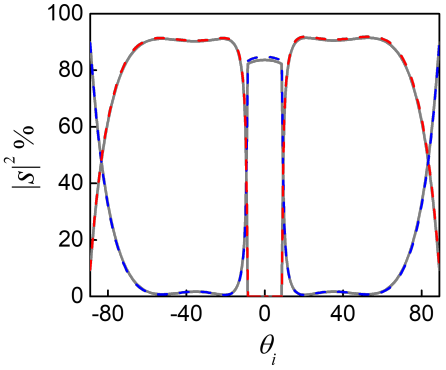

Figure 6.10: Tolerance to variations in the shape of surface elements. Scattering response of the system, replacing the original trapezoidal rods with rectangular rods (with equal mean widths). For comparison, gray lines project the scattering response of the original surface. Specularly reflected power and the first order negative reflection are shown by blue and red colors, respectively.

6.5.5. Supplementary Note 5

The metasurface is designed for s-polarized light, i.e.,light with electric field vector parallel to its plane. For s-polarized illumination, the majority of the incident wave is redirected toward the first diffraction order (which lies in the same half-plane as the incident one), creating a negative reflection effect. This effect is supported by the tailored distribution of local reflection coefficient for this polarization. On the other hand, under p-polarization the surface elements experience different local reflection phases due to their anisotropy. For measurements under p-polarized illumination, the surface is approximately a mirror, with around 15% coupling toward the non-specular diffraction channel and 15% absorption (Fig. 6.11, left panel). The measurements also show a critical incident angle for this polarization at which the incident light experiences enhanced absorption. Enhanced absorption at this angle is attributed to critical coupling between the free space mode and a grating resonance at the glass-silver interface. The measured reflection and absorption is confirmed via the corresponding simulations shown in Fig. 6.11 (right panel). We note that, by using isotropic surface elements in proper 2D arrangements, the metasurface can be designed to operate isotropically for both polarizations and 3D illumination angles [109]. We are currently exploring this possibility to create polarization insensitive back reflection.

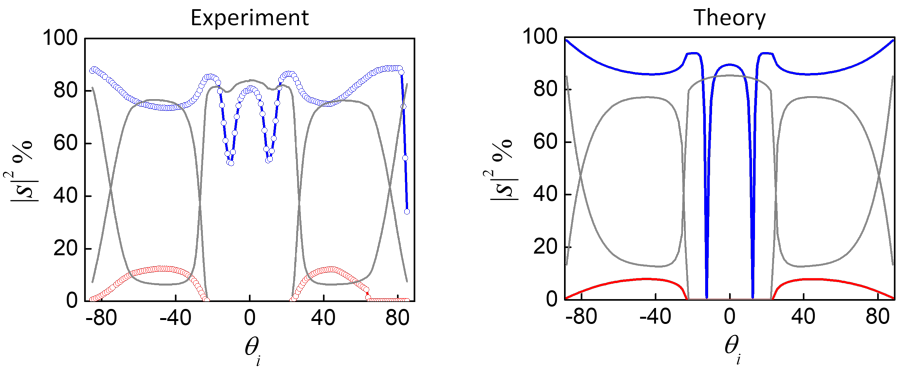

Figure 6.11: Scattering response for p-polarized illumination at 850 nm. Side-by-side comparison between measurement (left) and numerical analysis (right) of the fabricated device under p-polarized illumination. Specular reflection s_0^- the first-order negative reflection s_1^-, are shown with blue and red colors, respectively. To highlight surface anisotropy, the projected graylines show the corresponding response for s-polarized light, as in Fig. 6.8.

7

Detailed-balance efficiency limits of two-terminal perovskite/silicon tandem solar cells with planar and Lambertian spectral splitters

All alone she moves
Into a broken paradise surrounded by the colored lights

She moves – Alle Farben

We derive the photovoltaic conversion efficiency limit for two-terminal tandem solar cells with a perovskite top cell and silicon bottom cell with an embedded spectrum splitter. For large-bandgap top-cells a spectrum splitter strongly enhances the efficiency because of enhanced light absorption and trapping. A Lambertian spectral splitter shows a significantly improved effect compared to a planar splitter: we find an ideal efficiency enhancement in the thermodynamic limit for a 500 nm thick top cell of 6% absolute for bandgaps above 1.75 eV. Vice versa, the use of a spectral splitter geometry enables the use of a thinner top cell. Using experimental parameters for perovskite cells we show that for a top-cell bandgap of 1.77 eV a 2.8% absolute efficiency can be gained. The calculations in this work show that integration of a spectral splitter into perovskite/silicon tandem cells with a top bandgap above 1.7 eV can lead to a large increase in efficiency, even with realistic experimental losses and non-unity reflection of the spectral splitter.

7.1. Introduction

At present, solar photovoltaics (PV) has an installed capacity of around 600 GW_p worldwide [133]. Following the IRENA roadmap, by 2050 PV should reach an installed capacity of 8.5 TW_p to account for 43% of the total installed power capacity for electricity generation [134]. With the costs of the cells determining only a small part of the costs of a PV system, raising their efficiency is a key method to reduce the cost of PV per kW_p. Also, higher-efficiency panels take up less space, which is essential as PV is applied at very large scale. Therefore, in PV research it is crucial to fight for every digit that can be gained in cell efficiency. With 95% of the total production in 2019, the market is strongly dominated by single-junction Si-wafer based PV technology [135]. Silicon-based tandem solar cells have the potential to raise the efficiency beyond the theoretical limit of 29.4% for Si-only cells [8]. The combination of perovskite and Si in a 2-terminal (2T) or 4-terminal (4T) tandem configuration is one of the most growing and promising concepts. Recently, a Si-perovskite 2T tandem solar cell was presented with an efficiency of 29.15% [136] well above the record for a single-junction Si cell of 26.7% [137].

One aspect that is of high importance to improve the performance of tandem cells is light management to optimize the coupling and distribution of sunlight in the tandem subcells [31, 32, 138, 139]. Recent work has focused on minimizing reflection from the top or interlayers [29, 139–141] and reducing parasitic absorption in the inactive layers such as transparent conductive layers [32, 142, 143] and to optimize light trapping in the top and bottom cells [35, 144]. A concept that has not been studied in much detail is to control the spectral splitting of light directed into the two subcells [145]. Spectral splitting can be achieved by an additional interlayer between the top- and bottom cells that effectively reflects the part of the spectrum with energy above the bandgap of the top cell, and that transmits the remainder to the bottom cell. In an ideal case, the low- and high-energy spectral bands are fully split between the cells, so that maximum current and voltage can be harvested. However, in practical geometries a low-energy tail close to the top-cell bandgap is always transmitted due to incomplete light absorption in the top cell, and is then absorbed in the underlying cell (Figure 7.1a). This transmitted tail creates higher thermalization losses in the bottom cell and should thus be avoided.

Earlier, spectral splitting in 4T tandem cells has been modelled [145] and it was predicted that, by integrating a spectral splitting light trapping layer, an efficiency gain between 0.5% and 3% (absolute) and a two- to threefold reduction in thickness of the top cell can be reached, depending on the diffusion length of the absorber material. The benefits of spectral splitting in 2T tandem concepts have been studied previously to achieve current matching between top and bottom cell, using Bragg reflectors [147–150] or three-dimensional photonic crystals [151–153] as intermediate layers. Current matching is a limiting factor in 2T tandems, in particular for top cell materials with a bandgap below E_{BG} = 1.73 eV. In that case the current generated in the perovskite can exceed that in the Si, depending on the absorption in the top cell, in which case no spectral splitter is needed. However, a spectral splitter enables the use of a smaller perovskite cell thickness to obtain current matching with low-gap perovskites. In addition, for tandems with higher perovskite bandgaps, which have the largest potential tandem efficiency, and which have applications in photoelectrochemical splitting of water because of their high voltage [154, 155], for example, spectrum splitting has significant potential to en-

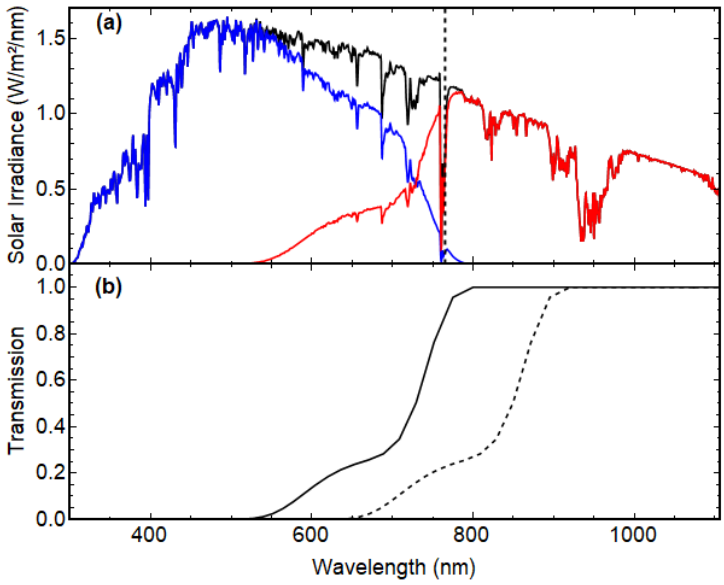

Figure 7.1: (a) AM 1.5G solar spectrum (black line) with theoretical absorption in 500 nm thick perovskite top cell (blue line) and spectrum directed into Si bottom cell (red line). The vertical dashed line marks the position of the bandgap E_{BG} = 1.62 eV. (b) Transmission spectrum of 500 nm thick perovskite with E_{BG} = 1.62 eV (solid black line) from [146] and modelled transmission for 500 nm thick perovskite with E_{BG} = 1.4 eV (dashed black line).

hance the efficiency. In the following, we show for which conditions a spectral splitter in a 2T perovskite/Si tandem cell is beneficial and what efficiency gains can be achieved. We make a distinction between planar spectral splitters with specular reflectivity, and spectral splitters with a Lambertian scattering distribution that enhances light trapping in the perovskite top cell.

7.2. Methods

Throughout the article, we use detailed-balance calculations [156] to determine the theoretical maximum efficiencies of the different 2T tandem configurations. Auger recombination in Si and other non-radiative processes are not taken into account and we assume full current collection from light that is absorbed in the top- and bottom cells. While such theoretical maximum efficiencies cannot be reached in reality, they allow a reliable comparison between different configurations. Similar trends as we find here will also apply for tandem designs in realistic experimental geometries. We differentiate between three cases of light absorption in the perovskite top cell:

1. Full absorption up to the bandgap as is typically done in detailed-balance limit calculations;

2. Ideal current splitting that assumes that the top cell absorbs exactly the amount of light such that half of the maximum possible current of the bottom cell (as a single-junction cell) is generated in the top cell;

3. Single pass absorption of a semi-transparent top cell with finite thickness d:

$$A_{TTC} = (1 - exp(-\alpha \cdot d)) \tag{7.1}$$

with α the absorption coefficient for the transmitting top cell (TTC). To model the bandgap-dependent absorption in the perovskite top cell we use the wavelength-dependent absorption coefficient of CsFAPbIBr with a bandgap of E_{BG} = 1.62 eV [146] which is in the bandgap range of the most frequently used perovskite top cells. Figure 7.1b shows the transmission of a 500 nm thick layer of this material (black solid line). The transmission for perovskites with the same thickness but other bandgap was then modelled by shifting the graph by the bandgap shift (Fig. 7.1b). Our simplified model of light absorption might not fully reflect transmission for specific perovskites with different material compositions and bandgaps, however, it allows us to systematically compare the effect of transparency of the top cell for different bandgaps.

7.3. 2T tandem efficiencies with semitransparent top cells

The thermodynamic (TD) limiting efficiency for 2T tandems, assuming perfect absorption up to the bandgap in the top cell of the perovskite/Si tandem, is maximal for E_{BG} = 1.73 eV with an efficiency of 45.1%. [157] (Fig. 7.2). The limiting efficiency gradually decreases as the top-cell bandgap approaches the Si bandgap (1.12 eV), where all light up to that energy is absorbed in the top cell with no current left for the bottom cell. We then define the current splitting (CS) limit as a condition, for a given perovskite bandgap, where the top cell is not fully absorbing up to its bandgap, but rather absorbs an optimized smaller fraction to obtain current matching (Fig. 7.2). In this ideal case the top cell absorbs light such that exactly half of the maximum possible current of the bottom cell (as a single-junction cell) is generated in the top cell. This requires a top cell with a bandgap below 1.73 eV. For bandgaps below 1.73 eV the CS limit is well above that for the thermodynamic limit of fully absorbing top cells. For higher perovskite bandgaps full absorption in the top cell is always optimal and equal to the CS limit.

As described above, for any perovskite bandgap the optimized absorption, or equivalently transmission, of the top cells can be realized by selecting the proper top cell thickness (see method section). We calculate the detailed-balance limiting efficiency using the modeled transmission (Eqn. 7.1) for thicknesses in the range 250-1000 nm as a function of bandgap of the top cell (Fig. 7.2). Several trends can be observed in this figure. First, the shape of every individual TTC limit is similar to the shape of the thermodynamic limit, with a pronounced maximum efficiency that is quickly decreasing for lower or higher bandgaps. This is because of the large sensitivity of 2T tandem cells to unbalanced currents in the top and bottom cells. For bandgaps below 1.73 eV the maximum efficiency for every thickness is much higher than the one derived from the thermodynamic limit assuming full absorption. The maximum of all four graphs for different thicknesses match the CS curve at the bandgaps where the currents are matched.

Figure 7.2 shows there is a wide range of perovskite bandgaps (1.5-1.7 eV) for which very high 2T tandem efficiencies can be reached by optimizing the perovskite thickness in the practical range of 250-1000 nm.

For top cells with bandgaps higher than E_{BG} = 1.73 eV, the TTC limit is much lower

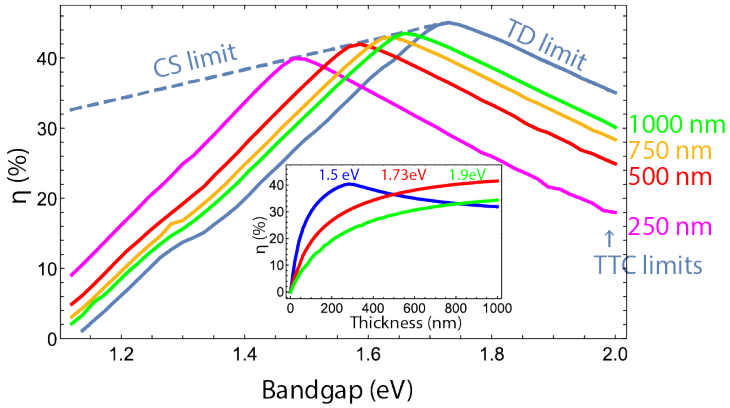

Figure 7.2: Detailed-balance efficiency limits for 2T tandem solar cells with Si bottom cell: Thermodynamic limit (TD) assuming perfect absorption in the top cell (solid blue line); Current splitting (CS) limit assuming ideal splitting of the spectrum for perfect current matching in top and bottom cell (dashed blue line); Transmitting top cell (TTC) limit assuming realistic absorption/transmission in a perovskite top cell for top cell thickness in the range 250-1000 nm. Inset: Comparison of dependence of efficiency on top cell thickness for three different perovskite top cell materials with E_{BG} = 1.5 eV, E_{BG} = 1.73 eV and E_{BG} = 1.9 eV.

than the thermodynamic limit, because incomplete absorption in the top cell due to the limited thickness limits the overall current. This is where a spectral splitting light trapping layer could be of special interest. Transmitted light above the bandgap is then reflected and trapped in the top cell, such that the thermodynamic limit could be approached for those bandgaps even with finite top cell thicknesses. This is discussed in detail in the next section.

The described trends are illustrated by the inset in Figure 7.2 where the TTC limit versus thickness of the top cell is plotted for three different bandgaps. For a bandgap below E_{BG} = 1.73 eV an ideal thickness can be chosen to reach the maximum TTC efficiency for that bandgap (e.g. 280 nm at 1.5 eV, see the inset). For bandgaps of E_{BG} = 1.73 eV and higher, the cell ideally is 'infinitely' thick to absorb all light above the bandgap energy.

7.4. Planar and Lambertian spectral splitter

Next we discuss the effect of a spectral splitter in between the top and bottom cell of a 2T tandem cell. We distinguish between: (1) a planar spectral splitter that reflects the light specularly back to the top cell and creates one extra path for absorption in the top cell; (2) a Lambertian spectral splitter that reflects the light back in a cosine angular fashion such that enhanced light trapping can be achieved in the top cell. Figure 7.3a shows a schematic of both spectral splitter geometries. The reflectivity $R(\lambda)$ of the spectral splitter is defined as a step function with tunable step wavelength λ_{step} and reflectance r:

$$R(E) = \begin{cases} 0, & \text{if } \lambda > \lambda_{step}. \\ r, & \text{if } \lambda \leq \lambda_{step}. \end{cases} \tag{7.2}$$

In both cases, we assume that light that is not reflected is transmitted losslessly to

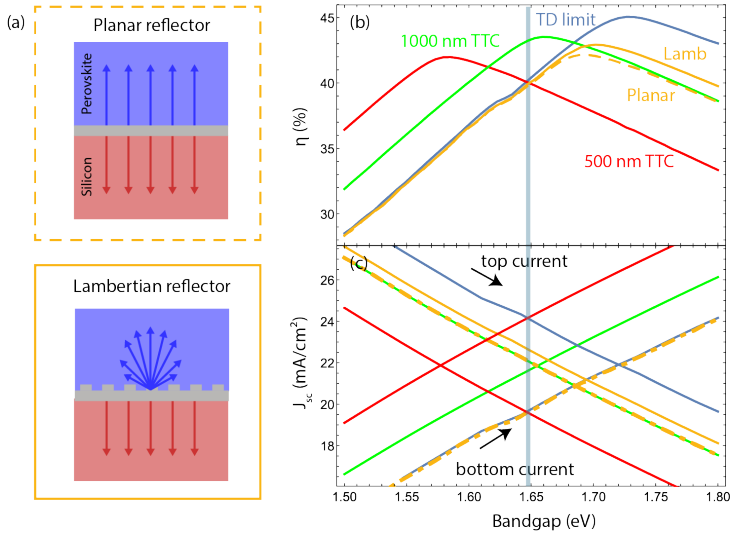

Figure 7.3: Spectral splitter in 2T tandem cell. (a) Schematics of planar and Lambertian spectral splitter (in gray). Light is selectively scattered back to the perovskite top cell (blue). The remainder of the spectrum is transmitted to the underlying Si cell (red). (b) Thermodynamic limiting efficiency for full absorption in the top cell (blue line), TTC limit with 500 nm (red) and 1000 nm (green) thick perovskite top cell. Limiting efficiencies of 2T tandems with 500 nm thick perovskite top cell and planar (dashed yellow line) and Lambertian spectral splitter (solid yellow line). (c) J_{sc} of top and bottom cell of tandem cells for all limits from (b). The graphs decreasing and increasing with bandgap represent the current of the top and bottom cells, respectively.

7

the underlying Si substrate. We add one additional absorption path in the top perovskite cell with length d for the planar splitter and length $d_{eff} = d \cdot (2 + x)/(1 - x)$ with $x = a(\alpha d)^b$, $a = 0.935$ and $b = 0.67$ to represent the angular distribution scattered by the Lambertian splitter [145, 158]. The absorption in the bottom cell is modified to account for the reflectivity R.

First, we assume that the reflectivity is split at the bandgap of the top cell ($\lambda_{step} = \lambda_{BG}$), and assume $r = 1$. In that case for both spectral splitter configurations the absorption in the Si bottom cell is identical to the one in the thermodynamic limit as no light below the top cell bandgap energy is transmitted to the bottom cell. Figure 7.3b shows the tandem efficiencies for a 500 nm thick perovskite top cell, comparing the TTC limit with the planar and Lambertian spectral splitting limits. Figure 7.3c shows the corresponding top and bottom cell currents. For a 500 nm top cell the planar or Lambertian spectral splitters strongly improve the tandem efficiency. At 1.70 eV the Lambertian splitter increases the tandem efficiency by more than 5% to 42.9%. Interestingly, this is even beyond the TTC maximum of 42.0% that occurs for a bandgap of 1.58 eV, reflecting the trend that the higher the absorption in the top cell, the closer the ultimate thermodynamic limit that assumes full absorption, which occurs at 1.73 eV, is achieved.

To further illustrate the benefit of the spectrum splitters, we show the TTC limit of a 1000 nm top cell in the same figure and compare the short-circuit current J_{sc} of the top and bottom cells in in the lower panel. The top cell J_{sc} for the 1000 nm thick cell and the 500 nm cell with planar spectral splitter is identical for all bandgaps as the top cell

thickness is effectively doubled by the planar spectral splitter. The bottom cell current, however, is always lower for the 500 nm thick cell with spectrum splitter. This is because for the planar geometry above-bandgap light that is not absorbed in the top cell is transmitted into the Si bottom cell, while with the spectral splitter it is reflected and lost from the front side of the top cell. For the larger bandgaps, the efficiencies of the 1000 nm thick cell and the 500 nm cell with planar spectral splitter become equal as the identical top cell currents are the limiting factor in both tandems.

The benefit of the Lambertian splitter over the planar splitter is twofold: it further enhances absorption in the top cell due to the larger angular scattering range, and, as a result, less light is lost from the front of the cell. Consequently, the top cell current of the cell with Lambertian spectral splitter is consistently higher than that of the planar spectral splitter while the bottom cell current of both cases is equal.

7.5. Splitting conditions

Next, we investigate the influence on the efficiency of an offset of the step energy from the top cell bandgap energy as well as incomplete reflectance from the spectrum splitter. This is of interest because it has been found that for 4T tandem cells, especially for planar reflectors, the escape losses from the front side of the cell for light at energies just above the top cell bandgap can be detrimental for the overall tandem performance [145]. To avoid this, we shift the reflection spectrum to slightly higher energy, so that the non-absorbed spectral band just above the top-cell bandgap is transmitted to the Si bottom cell. Figures 7.4a and b show the efficiency gains/losses for a 500 nm top cell with a bandgap of 1.7 eV as a function of ΔE and r, with and without planar and Lambertian spectral splitter, respectively. In both cases the best result is found for the highest reflectivity of the spectral splitter, but the figure shows that also for non-ideal splitters with $r < 1$, as they may be made experimentally, large efficiency gains are expected. For the planar splitter a maximum achievable efficiency enhancement above 4% is found; for the Lambertian one a gain of more than 5% is expected. In both cases, the optimum is found for a shift in the reflectance edge by about 10 meV above bandgap of the top cell. The maxima are marked with black stars in Figure 7.4a,b.

To further study the impact of the reflectance r we calculate the possible efficiency gain as a function of top cell bandgap for a Lambertian spectral splitter with 500 nm top cell thickness (Fig. 7.4c). In agreement with what is described above, efficiency gain is observed for the highest top cell bandgaps, while a loss is observed for the lowest gaps. However, we find that variation of r allows further optimization depending on the top-cell bandgap. An interesting subtlety occurs just at the cutoff energy 1.65 eV. Contrary to what was observed for the spectral splitter with $r = 1$ in Figure 7.3b, also for smaller bandgaps a spectral splitter geometry can be beneficial if the reflectivity is reduced. In Fig. 7.4c one can see that also here a Lambertian spectral splitter is beneficial and increases the efficiency by 2.7% absolute (marked with black star in Figure 7.4c), if the reflectance is set to be $r = 0.63$. In detailed balance calculations, an equal increase can be reached by increasing the thickness of the top cell, however, in practice an increase in thickness leads to losses in the open-circuit voltage .

We note that all calculations so far were based on an idealized set of assumptions. To get an idea of what efficiency enhancement can be expected in the Lambertian case

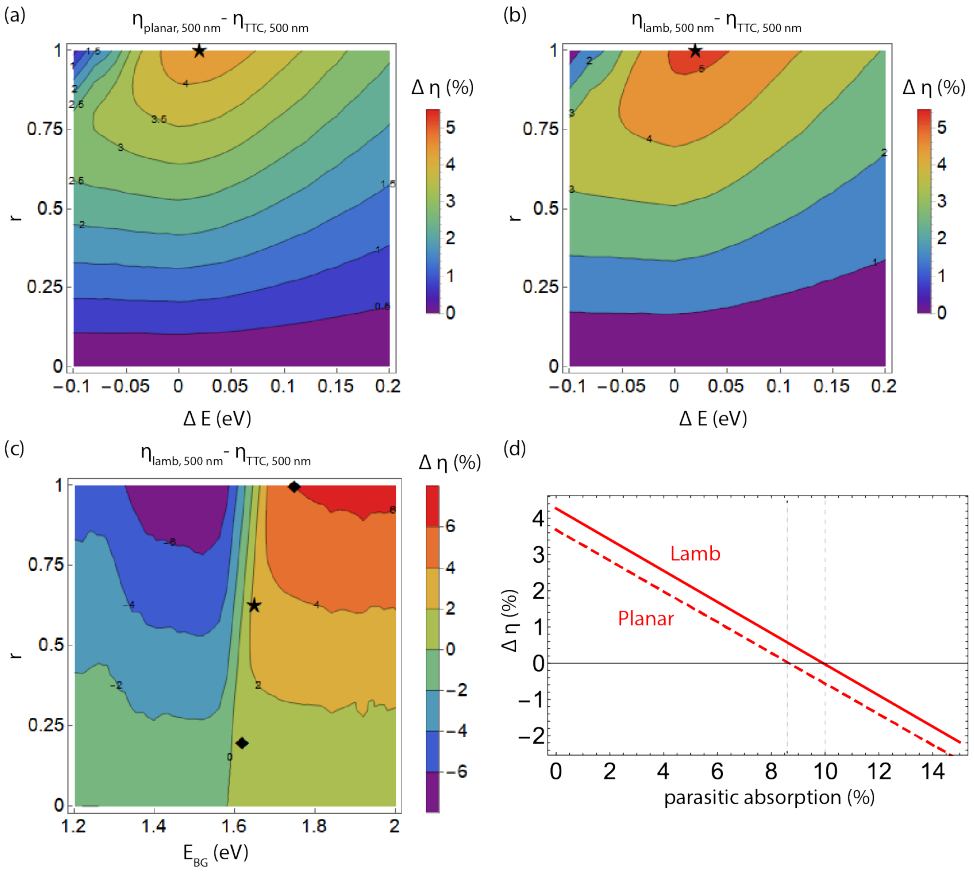

Figure 7.4: Absolute efficiency gain of 2T tandem cells depending on reflectance of the spectral splitter, the step wavelength and parasitic absorption in the spectral splitter. Efficiency gain for tandem cells with planar (a) and Lambertian (b) spectral splitter and 500 nm thick perovskite top cell with E_{BG} = 1.7 eV compared to TTC limit of the same cell, as function of ΔE and r. (c) Efficiency gain for tandem cell with Lambertian spectral splitter and 500 nm thick top cell as function of top cell bandgap and reflectance r with ΔE = 0.01 eV. The star indicates the ideal spectral splitting condition for maximal efficiency gain for a tandem cell with a 500 nm thick perovskite top cell with E_{BG} = 1.65 eV. The diamonds mark the position of maximum gain for two examples of realistic perovskit/silicon cells with E_{BG} = 1.62 eV and E_{BG} = 1.77 eV. (d) Efficiency gain for a tandem cell with Lambertian (solid red line) and planar (dashed red line) spectral splitter and 500 nm thick top cell as function of parasitic absorption in the spectral splitter.

for realistic materials, we applied detailed-balance calculations using data from selected record cells [159]. As a first estimate, we took a state-of-the-art perovskite/Si tandem cell with a top-cell bandgap of 1.62 eV. The corresponding EQE-spectra and thickness for the top cell layer were used to approximate the absorption coefficient around the bandgap, by assuming unity internal quantum efficiency. The resulting absorption coefficient was used to investigate the potential performance of a Lambertian spectral splitter for a 500 nm thick perovskite layer on top of Si. Figure 7.4c contains markers (diamonds) representing this comparison. In the case of the 1.62 eV perovskite, it turns out that an effi-

ciency enhancement of 0.30% absolute could be achieved (in the detailed-balance limit) for an ideal reflectance of $r = 0.2$.

So far, this analysis assumed detailed-balance-derived open-circuit voltage (V_{oc}) and fill-factor (FF) values. To get a more accurate estimate for realistic conditions, we approximate the tandem cell as a non-ideal diode under illumination described by $J(V) = J_{sc} - J_0 \cdot (\exp((q \cdot V)/(n \cdot k \cdot T)) - 1)$, where the overall current density $J(V)$ depends on the short-circuit current density J_{sc} and the voltage dependent diode current density term with the voltage V, the reverse saturation current density J_0, an ideality factor n, Boltzmann's constant k and the temperature $T = 300$ K. Using this equation, we can fit the effective recombination current $J_{0,tandem}$ and ideality factor n_{tandem} of the full tandem device from the cell's IV-curve. The V_{oc} was calculated by using the J_{sc} for the Lambertian case as derived above in the detailed-balance calculations, plugging it into the non-ideal diode equation and solving the equation for $J(V) = 0$. Furthermore, we account for the local FF minimum around the current matching condition [160] by applying the same relative FF-loss that is observed in the detailed-balance analysis above on the listed FF value of the experimental cell. This comparison yields 0.26% absolute efficiency enhancement ($r = 0.2$), just slightly lower compared to the initial estimate that was based on only adjusting the absorption coefficient to the experimental value.

Considering the two estimated values are rather close to each other, we feel confident in doing estimations for cases for which the nature of the available data only allows an estimate according to the first method. We take the top cell from the current perovskite/perovskite record tandem cell (1.77 eV) [159] and determine the absorption coefficient. For the imagined case of such a top cell on top of a Si bottom cell, this analysis yields an efficiency enhancement of 2.8% absolute at a reflectance of $r = 1$, highlighting that the significance of a Lambertian spectral splitter increases with the top cell bandgap. We note that the efficiency gains according to this estimate are less than what Figure 7.4c suggests (upper diamond), and this is attributed to the sharper onset of the EQE-derived absorption coefficients compared to the reference absorption coefficient that was used for the modelling of Figure 7.4.

Finally, an important parameter in the experimental realization of a spectral splitter are the losses that such a layer could introduce into the system. Figure 7.4d shows the efficiency gain/loss as a function of absorption, assuming spectrally flat parasitic absorption for a 500 nm thick cell. We find that for absorption up to 9/11% the planar/Lambertian spectral splitter is still beneficial.

7.6. Conclusion

In this chapter, we derive the detailed-balance efficiency limit of two-terminal tandem solar cells with a perovskite top cell and a Si bottom cell, considering the realistic incomplete absorption conditions for the perovskite top cell. We calculate the theoretically possible efficiency gain due to the introduction of a spectral splitter in between the top and bottom cell. For top cells with bandgaps above 1.7 eV, a spectral splitter strongly enhances light absorption in the top cell, leading up to 5-6% absolute efficiency gain in the thermodynamic limit for a 500-nm thick top cell. Using experimental parameters of realistic cells, we predict an efficiency gain for a practical perovskite-tandem cell with Lambertian spectral splitter of 2.8% for a top cell with a bandgap energy of 1.77 eV and

unity spectrum splitter reflectivity. In optimizing the reflectivity of the spectral splitter we find small subtleties in the 1.6-1.7 eV bandgap range, due to unwanted outscattering of light from the front side of the cell. The effect of parasitic absorption that will occur in experimental spectral splitters is also derived. Overall, our work shows there is a bright perspective for the integration of spectral splitters in perovskite-Si tandem solar cells, even if unity reflectivity cannot be achieved experimentally.

8

Four-terminal perovskite/silicon tandem solar cell with integrated Mie-resonant spectral splitter metagrating

Licht? Welches Licht?
Erzähl mir nicht du siehst das Licht nicht!

Sockosophie – Käptn Peng & Die Tentakel von Delphi

A spectral splitting, light trapping dielectric metasurface is designed, fabricated and integrated into a four-terminal perovskite/silicon hybrid tandem solar cell to increase the absorption of light close to the bandgap of the perovskite top cell, and enhance transmission of the near-infrared spectral band towards the bottom cell. The metagrating is composed of a hexagonal array of unit cells of 150-nm-tall hydrogenated amorphous silicon trimer nanostructures with dielectric Mie resonances in the 600-800 nm perovskite near-gap region, made using substrate-conformal imprint lithography. By tailoring the metasurface resonant scattering modes and their interference with the direct reflection paths we minimize specular reflection and obtain high diffraction efficiency that leads to improved light trapping in the perovskite top cell. The measured short-circuit current increase in the perovskite top cell is 0.5 mA/cm^2 corresponding to an estimated efficiency gain of 0.26% (absolute) for the metasurface-integrated 4T perovskite/silicon tandem cell. Simulations for a further optimized metasurface spectrum splitter geometry predict a short-circuit current gain in the perovskite top cell of 1.4 mA/cm^2 and an efficiency gain for the 4T tandem cell of 0.40% (absolute). The metagrating approach for simultaneous spectral splitting, light trapping and reflectance reduction provides a flexible platform that can be applied to many tandem cell geometries.

8.1. Introduction

Perovskite/silicon tandem cells are promising candidates for high efficiency solar cells that could find their route to broader commercialization in the next years. The present efficiency record of 29.15% lies well above the single-junction Si solar cell efficiency and the record will likely increase further in the coming years [136]. Four-terminal (4T) tandem cells are of specific interest, as for this cell design current matching is not needed and therefore their efficiency is less dependent on the top cell bandgap than for the case of two-terminal (2T) cells. 4T tandem cells are composed of two independent cells, with a transparent bottom contact on the top cell to allow light transmission to the underlying cell. In the top cell light absorption is usually incomplete, as the cell thickness is typically on the order of 0.5 µm, and part of the light close to the bandgap of the top material is transmitted to the underlying bottom cell. A schematic of the absorption of the solar spectrum in the top and bottom cell of a 4T perovskite/silicon tandem cell is shown in Figure 8.1a, using measured data for the transmission from a perovskite top cell [30] and full absorption in the silicon bottom cell. Light with wavelength in the λ = 600-800 nm spectral range at energy just above the perovskite bandgap energy (1.55 eV in this case) is partly transmitted and then absorbed in the underlying silicon cell. This creates losses in the tandem cell, as light close to the bandgap absorbed in the bottom cell creates a lower photovoltage than in the top cell. Introducing a spectral splitter interlayer in between the top and bottom cells can help circumvent these losses [145]. Ideally, a spectral splitter is designed such that all light with energy above the bandgap that is not absorbed in the first pass through the top cell is reflected back and trapped in the top cell. At the same time the spectral splitter can help reduce reflection of infrared (IR) light at the top/bottom cell interface, and thereby create enhanced IR absorption in the underlying silicon cell [140]. In our 4T tandem cell design [30] the perovskite top cell is placed on top of the silicon bottom cell with an airgap in between. This geometry allows to put the spectral splitter placed on a glass slide on the bottom of the perovskite cell without modification of the silicon bottom cell as the schematic in Figure 8.1b shows. To not introduce additional losses in the silicon cell, the spectral splitter/air interface has to fulfill the requirement to have a lower near-infrared reflectance than the glass/air interface on the perovskite bottom side in the top cell.

Spectral splitting has been explored in different tandem cell concepts and other hybrid solar cell systems. The spectral splitter was often designed to split the spectrum and direct the light in a specular direction. Most common approaches are the use of (semi-)reflective elements such as multilayer structures [161] and dichroic mirrors[162–165], or selective reflection off the top cell [166]. Intermediate reflectors for improved absorption in the top cell have also been studied before, using Bragg reflectors [140, 147–150] which can control the splitting spectrum in a stacked tandem cell and optimize for reduced IR reflection at interfaces. However none of these planar designs can direct light over an angular range to create light trapping. Martins et al. studied intermediate structures in 4T tandem cells and concluded that optical impedance matching between the sub cells is of higher importance than spectral splitting, however, not taking light trapping into account [140]. Three-dimensional photonic crystal structures have been used as intermediate reflectors with a small light trapping effect introduced by their diffraction orders [151, 152], but additional anti-reflection coatings are necessary to keep these

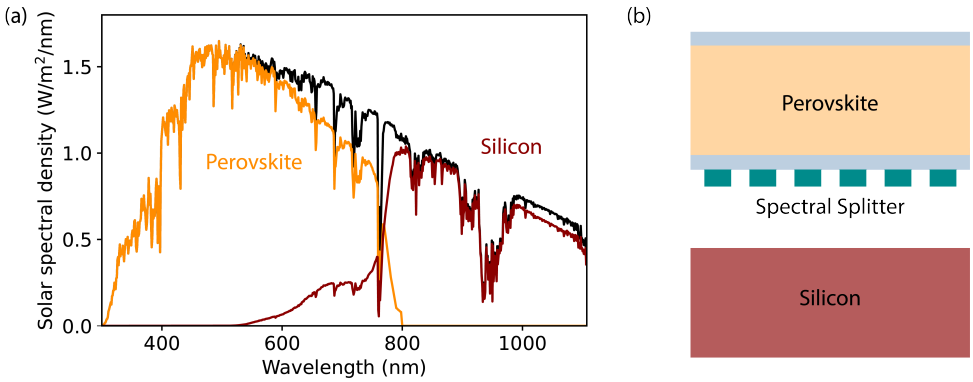

Figure 8.1: 4T Perovskite/silicon tandem solar cell (a) Absorption of solar spectrum (black) in 500 nm thick perovskite top cell (orange) and silicon bottom cell (red) based on experimental data from [30]. (b) Schematic of air-coupled 4T tandem cell with spectral splitter metasurface on bottom side of perovskite top cell. Blue bands on top and bottom of the perovskite are glass layers (not to scale); the top glass is the superstrate for perovskite growth; the bottom glass layer supports the metasurface and is attached to the perovskite with index-matching oil.

structures effective [153].

In this chapter, we design a spectral splitter that acts as a semi-transparent light trapping layer for the perovskite top cell. It reflects light with energy above the perovskite bandgap back to the top cell under high diffraction angles, creating light trapping in the top cell, while the long-wavelength spectral range is transmitted nearly lossless to the bottom cell. Previously, it has been shown that for a spectral splitter in a 4T tandem to be effective light has to be reflected in a Lambertian fashion to achieve maximum light trapping in the top cell [145]. However, the challenge has remained of how to create the spectral selectivity of Lambertian scattering that is required for the 4T design. For example, conventional textured scattering surfaces can create Lambertian light trapping but do not have spectral control.

Here, we introduce wide-angle scattering light-trapping metasurface that is spectrally selective by making use of dielectric scattering nanoparticles with optical Mie resonances. Dielectric metasurfaces have been used previously to improve the performance of tandem solar cells for increased absorption and anti-reflection from the different interfaces [34, 167], and light trapping [168, 169]]. First, we recap the theoretical 4T tandem efficiency limits in the thermodynamic limit case, and investigate potential improvements using an optimized metagrating. We then design and fabricate the metagrating and integrate it into a 4T perovskite/silicon tandem device [30]. In comparison with a 4T reference without spectrum splitter we measure a current improvement of 0.5 mA/cm^2 in the top cell of the tandem. The metasurface spectral splitter offers the first experimental solution to a spectral splitting layer with high light trapping in 4T tandem cells.

8.2. Thermodynamic limit for spectrum splitter designs

In this work, we distinct between a planar and a Lambertian spectral splitter (see schematics in Figure 8.2a). The planar spectral splitter reflects light back specularly and creates a single extra path of absorption through the top cell. The Lambertian spectral splitter reflects light back following a Lambertian angular distribution and creates enhanced light trapping in the top cell. We first calculate the thermodynamic detailed-balance efficiency limits, assuming imperfect absorption in a 580-nm-thick perovskite top cell and unity transmission to the underlying silicon cell using the methods discussed in [170]. Auger recombination in Si and other non-ideal processes are not taken into account and we assume full carrier collection in top and bottom cells. While the maximum efficiencies calculated using the detailed-balance model cannot be reached in reality, they allow a reliable comparison between different configurations and help predict important trends.

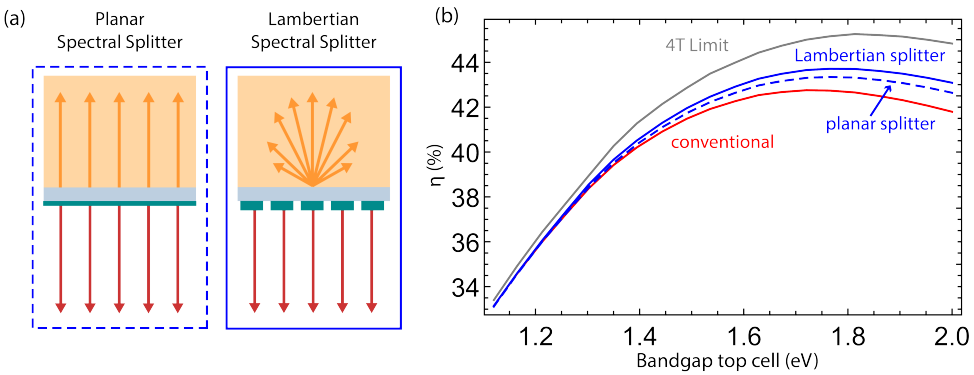

Figure 8.2: Spectral splitting in 4T tandem cell. (a) Schematics of planar (left) and Lambertian (right) spectral splitter. (b) Efficiency limit from detailed balance calculations of 4T tandem cell as function of top cell bandgap energy with silicon bottom cell (E_{BG}=1.12 eV). Thermodynamic limit (gray line), limit for 580 nm thick perovskite top cell (red line) and 580 nm thick perovskite top cell with integrated planar (dashed blue line) and Lambertian spectral splitter (solid blue line).

The results for the planar 580-nm-thick top cell, as well as the integrated planar and Lambertian spectral splitter are plotted in Fig. 8.2b. For both configurations we assume ideal spectral splitting, with 100% reflection of light with energy above the bandgap of perovskite (see details in supplementary (8.7.1)) and unity transmission into the bottom cell below that range. As seen in Fig. 8.1, the earlier conventional tandem design suffered from significant reflection losses at the perovskite/Si interface, as well as parasitic absorption in the transparent contacts, resulting in incomplete light collection in the Si bottom cell.

As can be seen in the figure, for a top cell bandgap of E_{BG}=1.55 eV (used in our previous work [30]), an absolute increase in efficiency of 0.3/0.6% is found for the planar/Lambertian spectral splitter, respectively. Enhancements by more than 1% are found for larger perovskite bandgaps. These calculations for the thermodynamic limiting case pave the way for designs of realistic geometries that are discussed next.

8.3. Spectrum splitting metasurface design

In this work scattering nanoparticles are arranged in a metagrating structure, a geometry that scatters light only in a well-defined resonant scattering spectral band, towards an optimized distribution of scattering angles, as we have shown before [26, 71, 91]. We design the scattering resonance spectrum of trimer-assemblies of resonant dielectric Mie scatterers that form the unit cell of the grating. The angular directivity is controlled by the periodicity of the grating in combination with the angular scattering distribution of the unit cell. We optimize the metagrating such that specular reflection is cancelled out, by creating destructive interference between light scattering from the resonant Mie particles and light reflected from the glass substrate that holds the scatterers. As scattering nanoparticles we use hydrogenated amorphous silicon (a-Si:H) cylinders; their high refractive index (n=3.89 at λ = 750 nm) makes them efficient scatterers, while low losses in the near-infrared (k<0.01 at λ = 750 nm) make them transparent in the perovskite light trapping range. The particle geometries are arranged on a 0.7 mm thick glass slide in a hexagonal grating.

To integrate the metasurface with the perovskite top cell, the glass slide is placed with index matching liquid against the indium tin oxide (ITO) bottom contact of the cell, with the nanopattern facing the air gap towards the silicon bottom cell. The perovskite top cell is grown in a superstrate configuration, with a 0.7 mm glass plate on its front side (see Fig. 8.1). The metasurface is designed and positioned in such a way that light trapping occurs in between the top and bottom glass plates of the top cell. Light that is scattered within the escape cone leaves the front of the top cell after one extra path through the perovskite. Light scattered from the metagrating outside the escape cone is reflected from the top glass back into perovskite. When interacting with the metasurface again, it partly leaves the cell on the bottom side, is partly scattered inside the cell again and, by reciprocity, partly scattered upwards, leaving the top cell on the front side.

The design of an optimized spectral splitter requires an integrated optimization of several scattering mechanisms. First, the Mie scattering unit cells must be made such that the resonance spectrum matches the desired λ = 600-800 nm light trapping spectral band for the perovskite. It must also be completely off-resonant for longer wavelength to facilitate full transmission of the 800-1200 nm spectral band into the silicon bottom cell. Furthermore, the scattering cross section combined with the geometrical unit cell fill fraction must create near-unity interaction of incident light with the metagrating in the 600-800 nm spectral band. We use insights from our previous work on metagratings [26, 91] to design the far-field interference of the electric and magnetic dipole and quadrupole Mie resonances to create the desired spectral shape and scattering strength. In parallel, we tailor the intensity and phase of the specularly scattered light such that it destructively interferes with light reflected off the glass/interface.

Our metasurface design is based on a hexagonal grid to have diffraction into 6 different azimuthal directions. The periodicity p = 525 nm was chosen to create diffraction in glass below λ = 800 nm. Light with a wavelength larger than λ = 525 nm has a diffraction angle larger than 42° inside glass and therefore experiences internal light trapping in the top cell. We perform finite-difference time-domain (FDTD) simulations [93] to calculate the reflection/transmission spectra of the metasurface on glass numerically. In the simulations, the source was placed inside the glass substrate, together with a reflec-

tion monitor behind it, in the glass, to determine the angle and intensity of individual diffracted orders inside the glass-perovskite-glass stack, while the transmission monitor was placed outside the bottom glass carrying the metasurface, to calculate the transmission to the underlying silicon cell. The dimensions (height and diameter) and unit-cell geometry (arrangement of scattering particles) were optimized for maximum efficiency of the complete 4T tandem cell. The optimized geometry consists of a unit cell composed of three 170-nm-tall scattering particles arranged in a windmill-like trimer geometry with elliptical wings of 70 nm diameter and 140 nm length (see Supplementary (8.7.2) for details on the geometry).

The simulated reflection spectrum of the optimized metasurface is plotted in Fig. 8.3a. The total reflectance is shown as well as the part that is diffracted into diffraction orders. One can see that the a-Si:H nanoparticles reach a resonant reflectivity up to 80% in the λ = 600-800 nm wavelength range, with a peak at around 750 nm, where enhanced light coupling and trapping in the top cell is desired. The major part of the reflected light is diffracted and trapped in the perovskite top cell. Furthermore, the reflectance for wavelengths between 800–1200 nm is around 0.5-2.5%, which is well below the reflectance of the glass-air interface (4%). This reduced reflectance for higher wavelengths is due to the fact that the particles are designed to show enhanced forward scattering in this wavelength regime, in addition to the fact that the metasurface has an effective index of around n=1.1 between λ = 800–1200 nm and therefore acts as an effective anti-reflection coating for glass [16]. The absorption spectrum is also shown in Fig. 8.3a and shows a Mie-resonant absorption peak for the a-Si:H nanoparticles as well as an increasing absorption due to tail states in the a-Si:H electronic bandstructure. This absorption forms no limitation in the spectrum splitting operation as the perovskite top cell is absorbing well in the low-wavelength range.

To determine the potential overall gain in efficiency due to integration of the spectral splitter we first use the detailed-balance calculations with perovskite bandgap 1.55 eV to determine the change in absorption in the top and bottom cell for the geometry in Fig. 8.1b. We compare a perovskite top cell with a glass bottom slide with the same cell with the above described spectral splitter metasurface. We take into account absorption enhancement in a 580-nm-thick perovskite top cell due to spectral splitting and light trapping, the corresponding absorption reduction in the silicon bottom cell and the absorption gain in the bottom cell due to higher transmission in the IR. The efficiency that can be gained is 0.7% absolute compared to the same tandem cell with a glass-air interface without spectral splitter.

Interestingly, this is higher than the 0.6% increase calculated above for the idealized Lambertian spectrum splitter. This is because the reduced IR reflectance to the planar glass-air interface is also taken into account here, while it was not in the calculations above. The short-circuit current gain in the perovskite top cell is calculated to be 1.6 mA/cm^2, a relative increase of 7%. Translating this to the experimental short circuit current for the perovskite top cell that we will use below [30] this corresponds to a short-circuit current enhancement of 1.4 mA/cm^2.

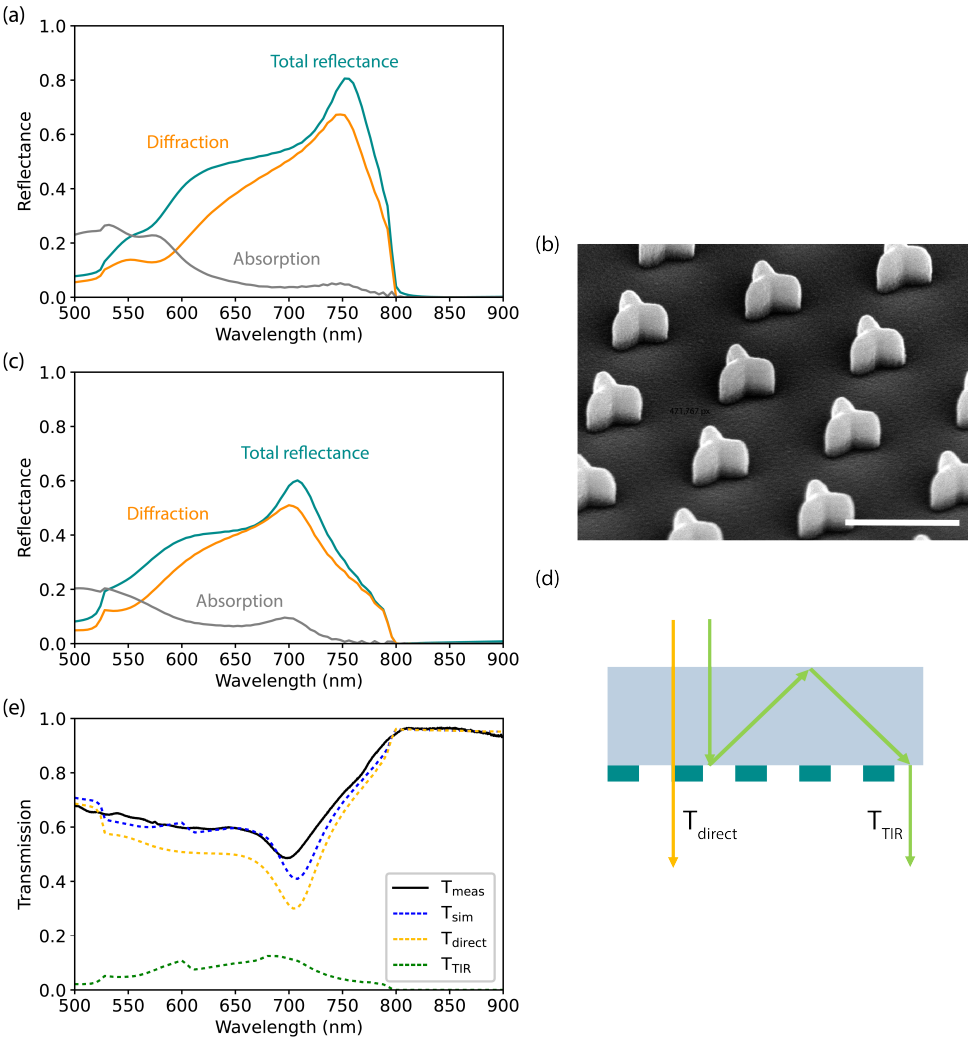

Figure 8.3: Spectral splitter metasurface. (a) Simulated total reflectance (green), diffraction (orange) and absorption (grey) of optimized spectral splitter metasurface. (b) SEM tilted top-view image of metasurface: a-Si:H windmill shaped particles on glass substrate (covered with around 10 nm chromium layer for better imaging). Scale bar is 500 nm. (c) Simulated total reflectance (green), diffraction (orange) and absorption (grey) of fabricated spectral splitter metasurface. (d) Paths of transmission through glass slide with same coloration as in (e). (e) Optical transmission measurements (black) of fabricated metasurface, calculated/simulated transmission (blue dashed line) composed of direct transmission (yellow dashed line) and transmission after total internal reflection (green dashed line).

8.4. Metagrating spectrum splitter fabrication

To fabricate the spectrum splitting metasurface and integrate it in the 4T design, a 150-nm-thick a-Si:H layer was deposited on a glass substrate by plasma-enhanced chemical

vapor deposition (PEVCVD), and the glass was cut into 2x2 cm^2 samples. We use Substrate Conformal Soft Imprint Lithography (SCIL), to replicate the structure over an area of several cm^2 [38]. For this, first we create a SCIL stamp with an imprint area of 2.5x2.5 cm^2 with notches with parameters of the nanoparticles described above. We spin-coat a layer of 50-nm-thick silica sol-gel on top of the a-Si:H/glass sample, imprint the sol-gel with the SCIL stamp and let it cure for 8 minutes. After removal of the stamp, the pattern is transferred into the silicon with a double Reactive Ion etching (RIE) plasma etch step, first to break through the sol-gel layer (25 sccm CHF_3, 25 sccm Ar) and second to transfer the pattern from the sol-gel mask into the silicon layer (15 sccm CHF_3, 10 sccm SF_6, 3 sccm O_2). The residual of around 10 nm of sol-gel on top of the Si nanoparticles showed a negligible effect on the results in simulation and was therefore not removed from the silicon pillars. Fig. 8.3b shows a Scanning Electron Microscopy (SEM) top-view image of the fabricated structure. It matches quite well with the targeted dimensions calculated above: the windmill wings are 15 nm shorter than designed and the height of the particle is 150 nm, 20 nm less than designed. Figure 8.3c shows the simulated reflectance of the fabricated structure. The reflectance shows a maximum above 60% and the resonance peaks near 700 nm, somewhat blue-shifted from the desired range. However, the simulation shows also for this fabricated geometry the key desired features: high diffraction efficiencies and low reflectance above 800 nm. Using the simulated data for the experimental geometry as input for detailed-balance calculations we calculate an efficiency gain for the perovskite/Si tandem with metagrating in Fig. 8.3b of 0.6% absolute, and a current gain of 1.0 mA/cm^2 (+4%) in the perovskite top cell. In practice, the latter would translate to a 0.9 mA/cm^2 enhancement in the experimental perovskite top cell.

8.5. Experiments

To characterize the fabricated spectrum splitter, two different measurements were performed. First, the transmission of the metasurface/glass sample was measured and compared with the simulations. Second, the spectral splitter was integrated with a semi-transparent perovskite top cell using index-matching fluid and External Quantum Efficiency (EQE) as well as transmission and reflection measurements were performed. In parallel, we used measurements of the external quantum efficiency of the Si bottom cell to calculate the performance of the metasurface-integrated 4T tandem cell geometry.

8.5.1. Optical measurements

Transmission measurements of the fabricated metasurface/glass sample were performed in an integrating sphere setup with an NKT super-K white-light laser source with a collimated beam at perpendicular incidence on the sample. The measured transmission is mainly composed of two contributions (Fig. 8.3d); direct transmission though the glass slide with metasurface, and transmission of light that follows diffracted paths inside the glass. The measured transmission is shown in Fig. 8.3e and compared with the sum of the contributions derived from the simulated spectrum of the fabricated sample. The spectrum compares very well with the simulated transmission spectrum, in which we have taken into account an additional 4% reflection at the top glass surface and total internal reflectance inside the glass slide. The measured transmission dip of

35% near 700 nm in Fig. 8.3e indicates the metasurface effectively reflects in the spectral range near the perovskite bandgap, in agreement with the simulated reflectivity in Fig. 8.3c. The simulations show that up to 12% of the transmitted light originates from paths that are first diffracted off the spectrum splitting metasurface. For a metasurface integrated with the perovskite top cell these paths will lead to enhanced absorption in the perovskite. Given the fact that strong correspondence is achieved between simulation and experiment in Figure 8.3e, we are confident that optimized metasurface design presented above (with more redshifted resonance and higher resonant reflectivity) will in practice yield the 1.4 mA/cm^2 current enhancement for the perovskite top cell as calculated above.

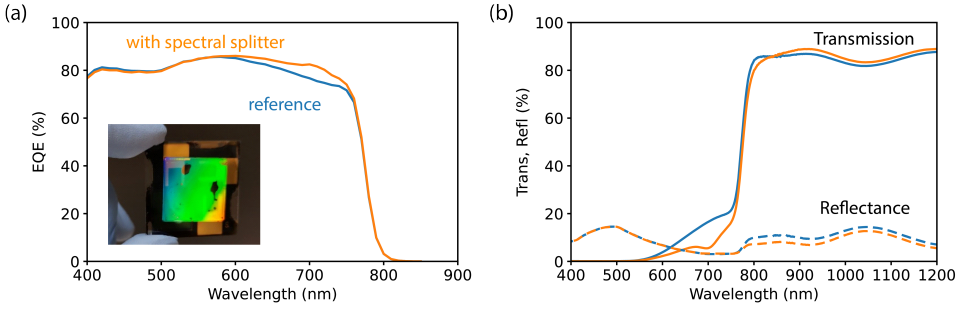

Figure 8.4: Measurements of metasurface integrated with perovskite cell. (a) EQE measurements of perovskite with spectral splitter (orange) and with glass reference (blue) Inset: Photograph of perovskite with spectral splitter taken from the bottom (facing the metasurface). Diffracted colors from the metasurface are clearly visible. (b) Transmission and reflectance measurement of the perovskite cell with spectrum splitter integrated.

8.5.2. Transmission and reflection spectra and EQE measurements of spectral splitter integrated in perovskite cell

Next, the glass/metagrating sample was placed on the bottom side of a perovskite top cell (see schematic of Figure 8.1b, and inset in Figure 8.4a). The glass side of the sample was connected with index matching oil on the ITO bottom side, with the silicon metasurface facing towards air. The perovskite cell is composed of a ~580 nm thick $Cs_{0.05}(MA_{0.17}FA_{0.83})Pb(I_{0.9}Br_{0.1})_3$ absorber layer with hole and electron transport layers and ITO top and bottom contact layers. The layer stack is composed (from top to bottom) of thermally-evaporated MgF_2, a Corning XG glass substrate, sputtered hydrogen doped indium oxide, spincoated PTAA, the spincoated perovskite layer, evaporated C60, a layer of SnO_2 deposited with spatial atomic layer deposition, and another layer of sputtered ITO [30]. For the reference measurements a perovskite cell with a glass bottom slide was used. EQE measurements are shown in Fig. 8.4a. The metasurface spectrum splitter creates a clearly enhanced EQE over the 600-750 nm spectral range, corresponding to a current gain of 0.4 mA/cm^2 in the perovskite top cell. This trend is in agreement with the reduced transmittance of the cell in this spectral range as shown in Fig. 8.4b. The transmittance spectrum shows an enhanced transmission above λ = 800 nm demonstrating the effective forward scattering and anti-reflection effect of the metagrating. No

additional reflectance is measured below λ = 800 nm showing the spectrum splitter does not create additional escape of light from the top side of the perovskite. Above λ = 800 nm, the reflectance is lower than in the reference sample, consistent with the increased transmission.

Finally, we compare the gain in short-circuit current derived from Fig. 8.4a (0.4 mA/cm^2) with the simulations. As described above, the detailed-balance calculations, scaled to the experimental short-circuit current for the used perovskite predict a current improvement of 0.9 mA/cm^2, well above the measured value. We attribute the difference between measurement and simulation to light leaking from the edge of the spectral splitter, as well as incomplete light trapping because light can escape from the edges of the top cover glass. In the present geometry the perovskite cells size is only 4x4 mm^2. As light close to λ = 800 nm is refracted from the metagrating under a wide angle a major fraction of it will escape from the 0.7-mm-thick glass slide and is thus not absorbed in the perovskite cell. Furthermore, light that passes through the perovskite cell once and experiences total internal reflection on the top glass slide is not channelled through perovskite a second time, because of the small cell size (see sketch and further explanation in SI (8.7.3)). To qualitatively prove the importance of this effect we repeated the EQE measurement with a similar sample that was cut to roughly match the size of the perovskite top cell and covered the sample edges with a 50-nm-thick silver layer to serve as a mirror. With this modification we measure (from EQE measurements) a slightly higher current increase of 0.5 mA/cm^2 in the perovskite top cell. Given the strong correspondence between reflectance simulations and measurements (Fig. 8.3b) further improved metasurface/cell integration is expected to yield the estimated current gain of 0.9 mA/cm^2.

Taking into account the EQE of the used Si bottom cell this would translate into an overall efficiency gain of the 4T tandem cell with spectral splitter of 0.26% (abs.) (See SI (8.7.4)). Calculations using the further optimized metasurface design introduced above yield an efficiency enhancement for that geometry of 0.40%. At last, it should be mentioned that adding an anti-reflection coating of MgF_2 as in [30] on the bottom side of perovskite can lead to further enhanced transmission in the infrared compared to the spectral splitter geometry in this work. Such additional optimization steps for reduced reflectance in the infrared are therefore of interest in future.

8.6. Conclusion

In conclusion, we designed and fabricated a spectral splitting light trapping dielectric metasurface as an interlayer in 4T perovskite/silicon tandem cells. We use the resonant light scattering principle of metagratings to design a spectral splitter with high diffraction efficiency in the bandwidth of interest and reduced reflectance and enhanced transmittance for the near-infrared spectral band. Simulations for the experimental geometry, corrected for experimental cell parameters, predict a short-current current enhancement in the perovskite top cell of 0.9 mA/cm^2 and an efficiency gain of 0.26% (abs.). The experimental enhancement derived from EQE measurements is 0.5 mA/cm^2, the difference partly attributed to light leakage due to the small sample size. Simulations show a further improved design could yield an experimental short-circuit current enhancement of 1.4 mA/cm^2, corresponding to an efficiency enhancement of 0.40% (abs.). The

demonstrated metagrating structure is flexible in design and can be adjusted to other top bandgaps or tandem geometries. The soft imprint technique to fabricate the metagratings is scalable up to wafer-sized imprints. Our work shows that the critical balance between spectral splitting, light trapping and concurrent reduced reflectance in the infrared can be fulfilled with these dielectric metasurfaces.

8.7. Supplementary

8.7.1. Ideal design conditions of spectral splitter for an ideal 4T tandem solar cell with Si bottom cell

We define the reflectivity $R(E)$ of an ideal spectral splitter as a step function with tunable step ΔE away from the bandgap energy of the top cell and reflectance r:

$$R(E) = \begin{cases} 0, & \text{if } E < E_{BG} + \Delta E. \\ r, & \text{if } E \geq E_{BG} + \Delta E. \end{cases} \tag{8.1}$$

In Figure 8.5 the parameters r and ΔE are swept to find the optimal splitting conditions, leading to the maximal efficiency enhancement compared to a 4T tandem cell with Si bottom cell without spectral splitter, as shown in the main text in Figure 8.6b. The top cell bandgap was fixed to E_{BG}=1.55 eV. The ideal parameters were found to be r=1 and ΔE = 0.1 eV and ΔE = 0.06 eV for the planar and Lambertian spectral splitter respectively. The smaller value for ΔE found for the Lambertian case reflects the better light trapping for that geometry.

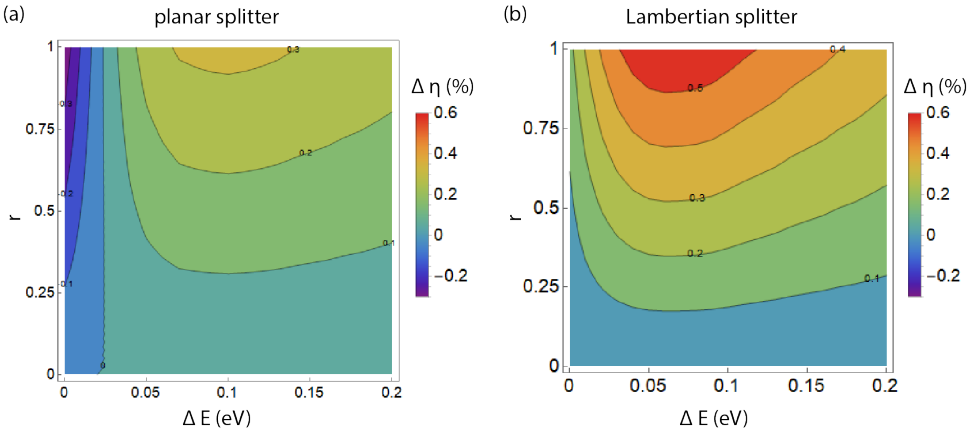

Figure 8.5: Parameter sweep of selective reflector step function for a (a) planar and (b) Lambertian spectral splitter in a 4T tandem solar cell with a top cell bandgap of E_{BG} = 1.55 eV and Si bottom cell.

8.7.2. Optimized spectral splitter design

The unit cell of the metasurface was optimized using parameter sweep optimization. The windmill-shaped particle described in the main text is composed of 3 identical ellipses (see Figure 8.6a), each rotated by 120°, with minor radius of r_1 and major radius r_2.

The relation between r_1 and r_2 is given by $r_2 = f_1 \cdot r_1$. The distance between the center of the ellipses (C_1, C_2 and C_3) and the center of the unit cell (C_0) is given by d, with d given by : $d = r_1 + f_2 \cdot r_1$. The maximum gain in efficiency for the metasurface-integrated 4T geometry was found for a hexagonal lattice with pitch 525 nm and a unit cell described by : $r_1 = 35$ nm, $f_1 = 2.4$, and $f_2 = 0.7$. The simulated scattering cross section of this windmill-shaped particle normalized by the geometrical area is shown in Figure 8.6b. The particle has a clear resonance in the relevant wavelength band between 550-800 nm with a peak scattering cross section beyond 10. This implies that a geometrical filling fraction of 10% suffices to achieve full interaction of incident light with the metasurface on resonance.

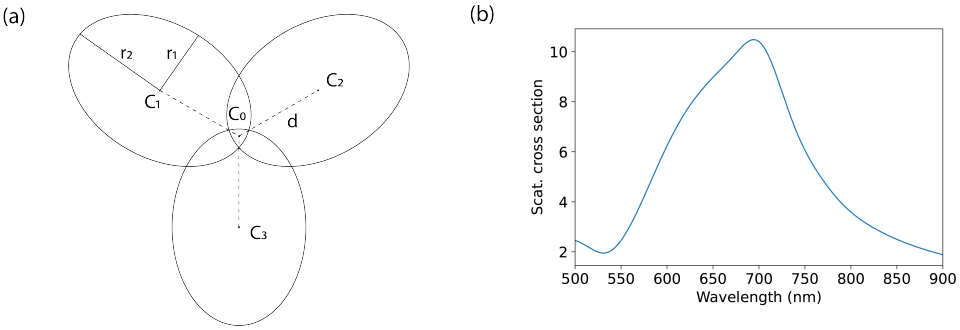

Figure 8.6: (a) Dimensions of the windmill shaped a-Si:H particle in the hexagonal unit cell of the metagrating. (b) Scattering cross section of the optimized particle.

8.7.3. Edge effect

The spectral splitter metasurface was designed for a wafer-sized solar cell where edge effects do not play a major role. The simulations were performed not taking any edge effects into account. However, in experiments, the size of the perovskite top cells is limited to 4 mm x 4 mm. This means that, for the glass thickness that is used (0.7 mm), light with wavelengths above 760 nm, which has a diffraction angle below 75° is lost at the edges. This is a substantial part of the reflectance spectrum and can explain the lower measured current gain in the perovskite, in comparison to the simulations (see Fig. 8.7 top schematic, red solid light path). Additionally, light that is reflected to the perovskite top cell and experiences total internal reflection on the top glass surface also is partially lost due to the small size of the perovskite and does not experience a second pass through the cell (see Fig. 8.7 top schematic, red dashed light path). The geometry with the Ag coated edges described in the main text is presented in the bottom schematic of Figure 8.7 and can partly reduce the edge effect. Furthermore, in the EQE measurements the light beam has a 3 mm–diameter spot size, so that part of the light that is diffracted under shallower angles can escape from the edges, lowering the achievable current enhancement.

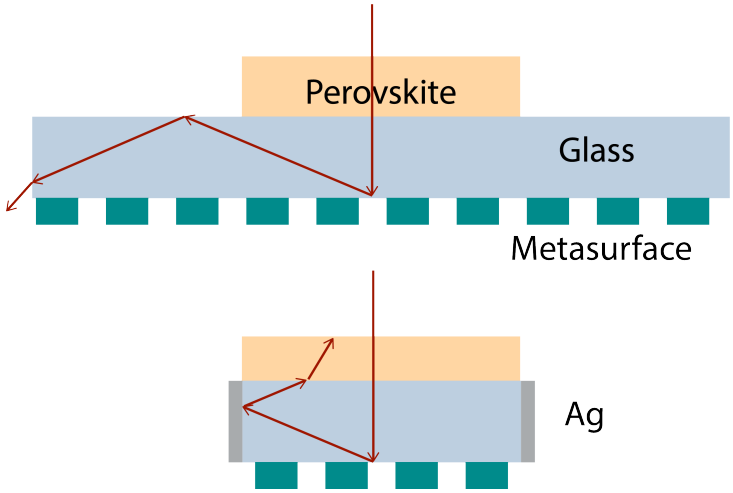

Figure 8.7: Schematic of edge effect in experiment. Top schematic: Part of the light escapes because the spectral splitter is bigger than perovskite cell (red solid line) and because the front glass slide is bigger than the perovskite cell (dashed red line). Bottom: If the spectral splitter is cut and the edges are covered with silver light is redirected to the perovskite cell

8.7.4. Overall tandem cell performance with integrated spectral splitter metagrating

Figure 8.8 shows EQE measurements of the silicon solar cell in the 4T geometry with the spectrum splitter integrated in the top cell. We use a commercial 5" interdigitated-back-contact (IBC) c-Si solar cell from SunPower. The data are compared to the EQE of a reference 4T tandem cell with a glass plate on the bottom side of the perovskite. For wavelengths below 800 nm the EQE in the silicon cells is decreased, because, as designed, light is reflected towards the perovskite top cell by the spectral splitter. Above 800 nm, the EQE is increased compared to the reference sample, due to reduced near-IR reflectance at the bottom side of the perovskite cell by the spectral splitter.

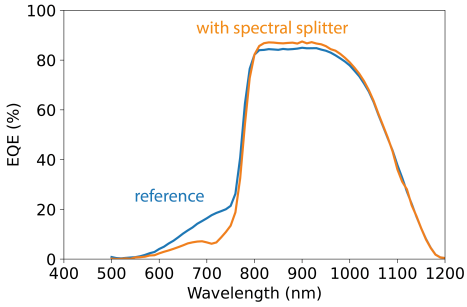

Figure 8.8: EQE measurement of Si bottom cell with and without spectral splitter.

From the EQE data we infer that a short-circuit current of 0.8 mA/cm^2 is lost in the

silicon cell. With the presently measured 0.5 mA/cm^2 short-circuit current gain in the perovskite top cell this would not enhance the tandem cell efficiency. However, as described above light leakage in the small sample geometry has likely affected the current measurement. Assuming the calculated 0.9 mA/cm^2 current enhancement for the experimental geometry (see main text), an efficiency gain for the tandem due to the spectrum splitter of 0.26% is expected. As described in the main text, a further optimized metasurface geometry would lead to a 1.4 mA/cm^2 short-circuit current enhancement in the perovskite cell, which would translate into an estimated 0.4% efficiency enhancement for the tandem cell. For these efficiency calculations, the open-circuit voltage (V_{oc}) and fill factor (FF) were taken from I-V measurements of the individual cells in the 4T geometry, as listed in Table 8.1. The table also summarizes the efficiencies for different geometries quoted in the paper.

Cell		V_{oc} (mV)	J_{sc} (mA/cm^2)	FF	Efficiency (%)
perovskite top cell	reference	1063	20.7	0.778	17.12
	with spectrum splitter + Ag	1063	21.2 (+0.5)	0.778	17.53
Si bottom cell	reference	703	16.1	0.800	9.05
	with spectrum splitter + Ag	701	15.3 (-0.8)	0.799	8.57
4T perovskite/Si tandem: experiment	reference				26.17
	with spectrum splitter				26.10 (-0.07)
4T perovskite/Si tandem: calculations	reference		20.7 (perovskite)		26.17 (4T cell)
	with fabricated splitter		21.6 (+0.9) (perovskite)		26.43 (+0.26) (4T cell)
	with optimized splitter		22.1 (+1.4) (perovskite)		26.57 (+0.40) (4T cell)

Table 8.1: Performance of the perovskite, c-Si cell and tandem cell with and without spectral splitter. The enhancements due to the spectrum splitting metasurface compared to the geometry without spectrum splitter are indicated between brackets.

Summary

Photovoltaics (PV) has the potential to become one of the major energy sources in a future with carbon-neutral energy supply. Two key aspects to achieve large-scale implementation of PV in our society are the seamless integration into buildings and infrastructure and a further increase of photovoltaic conversion efficiency. Integration of PV in our environment requires the development of solar cells with a colorful appearance. An increase of the efficiency in PV can provide a reduction in cost per generated power, as well as the demanded area required for the installation of PV systems. Achieving high efficiency requires the development of multijunction solar cells composed of multiple materials.

In this thesis we develop dielectric nanostructures to create tailored colorful appearance of solar cells and show how similar structures can increase the efficiency in tandem cells. For this, we design layers composed of dielectric nanoparticles that show strong light scattering in the visible spectral range. In particular, we develop dielectric metasurfaces and combined (gradient) metagratings that enable the control of spectrum and directivity of scattered light. In the first part of the thesis, we present novel ways to realize coloration of PV (Chapter 2-5), and design metasurfaces with tailored spectral and angular control of light (Chapter 4, 6). In the second part of the thesis, we theoretically and experimentally develop metasurface spectral splitters to improve the performance of two-terminal and four-terminal perovskite/silicon tandem solar cells (Chapter 7, 8).

In Chapter 2 we integrate crystalline Si nanocylinder arrays (radius = 100–120 nm, height = 240 nm, period = 325 nm) in the front module layer of mini silicon PV modules and demonstrate efficient coloration of the modules. The characteristic Mie resonances in the visible of the nanocylinder cause strong (35-40%) specular light scattering around a wavelength of λ = 540 nm and create a green coloration of the module that is quite independent from incoming angles over the 8–75° angular range. The colored module only shows a reduction of 10–11% in short-circuit current and efficiency. The green solar modules presented here can find applications in building- and landscape-integrated photovoltaics of many different kinds. For the fabrication we use the soft imprint conformal lithography (SCIL) nano-imprint technique that is applicable to full-area (15 x 15 cm^2) solar cell patterning.

Chapter 3 expands the technology of Chapter 2 to an increased color space. By changing the size and the distribution of the scattering nanocylinders (radius = 50–150 nm, period = 160-300 nm) we control the interference of electric and magnetic dipoles to create resonant scattering over a distinct spectral band. Pure colors from blue to red can be created with a scattering efficiency of up to 75%. The technique is extended by creating mixed colors (e.g. white) by combined pixels of nanocylinder arrays. We fabricate a white solar mini-module that shows a current loss of only 19%, due to the fact that only light in a well-defined visible spectral band is reflected. The route of combining differently structured metasurface pixels shows a great flexibility in creating colors by choice

and demonstrates the large potential for this technique to be widely applied.

In Chapter 4 we demonstrate metasurfaces composed of combined metagratings with tailored angular scattering profiles of Si Mie resonators. We control the spectral response by tailoring the interference of the modes of the nanoparticles and arrange them into patches of different periodicities to control the directivity of the scattering into diffraction orders. Based on a theoretical dipole scattering model, we designed these ultrathin surfaces (height = 185 nm) to realize broad-angle (35-75°) and Lambertian-like large-angle (0-75°) scattering profiles on resonance (λ = 650 nm). Specular reflection is canceled out by destructive interference of the scattering of the particles and reflection of the substrate, and high-order diffraction modes are strongly suppressed by shaping the scattering of a unit cell with several nanoparticles. Experimentally, the metasurfaces are composed of Si nanobars on a Ag mirror protected by a thin dielectric layer, and reach scattering efficiencies of 73-84%. The ultrathin resonant metagratings effectively create the functionality of "nanostructured paint", which can find applications in photovoltaics with colored appearance and angular behavior by choice as demonstrated in Chapter 5. Similarly, the presented metasurfaces can serve as spectrum splitting architectures in tandem solar cells as described in Chapter 7 and 8.

In Chapter 5 we follow up on Chapter 4 by experimentally demonstrating spectral and angular control of scattered light using combined resonant metagratings that create light scattering only for a determined set of angles. By tailoring the interference between the light scattering modes of the nanoparticles we control the scattering spectrum, and by arranging them into patches of different periodicities, we control the directivity. Silicon nanowires were fabricated on a transparent substrate and resonantly scatter light around λ = 650 nm. The nanowires were placed in a supercell structure composed of multiple gratings with different pitches (675-1300 nm), creating a wide-angle scattering distribution within the 30-75° range. The metagratings are designed to suppress specular refection and show efficient transmission outside the resonant scattering band. The metagratings are integrated with a silicon heterojunction solar cell creating a bright red scattering appearance under a limited range of angles. The external quantum efficiency is only reduced in the scattering spectral band, with a short-circuit current drop of only 13%. This structure can find application in rooftop photovoltaics and other building integrated PV that benefits from light reflection towards a well-defined angular range.

Chapter 6 shows the theory, design and experimental realization of a broadband back reflector metasurface based on the Huygens-Fresnel principle. Using a phase-gradient approach we design a theoretical metasurface with unity efficiency for back reflection. By creating a periodic phase change of light reflected from the surface, light is efficiently channeled into the first negative diffraction order over a broad angular range and over bandwidth in the visible spectral range. In the experimental realization, the calculated phase gradient is discretized and arrays are formed by unit cells of TiO_2 nanowires of different height, placed on a Ag mirror. This metasurface allows back reflection for a broad range of wavelengths from λ = 490 - 940 nm with an efficiency above 85%. The advantages of the design lie in its low profile, simplicity of design, broad bandwidth and wide acceptance angular range. The ultrathin metasurface can replace more bulky back reflectors and find application in many optical technologies.

In Chapter 7 we theoretically study the benefits of a spectral splitter integrated into

a perovskite/silicon two-terminal (2T) tandem solar cell. The spectral splitter reflects light with energy above the bandgap energy of the top cell and therefore enhances the absorption in the perovskite to benefit from the higher photovoltage in the top cell. We distinguish between a planar and a Lambertian scattering spectral splitter and find that by choosing the right splitting condition for the strength and spectral onset of the reflectivity, both spectral splitter configurations are beneficial for 2T tandem cells. For top cell materials with bandgaps above 1.7 eV, a spectral splitter is always beneficial as it enhances absorption in the top cell and creates better current matching with the bottom cell. Detailed-balance calculations show that including a Lambertian spectral splitter interlayer for 500 nm thick perovskite top cells with bandgap higher than 1.7 eV leads to 5%-6% absolute efficiency gain. Using experimental parameters of realistic cells, we predict a potential efficiency gain of 2.8% (absolute) for a top cell with a bandgap energy of 1.77 eV.

In Chapter 8 we experimentally demonstrate a spectral splitting light trapping metagrating as an interlayer in 4T perovskite/silicon tandem cells. This metagrating has the property to efficiently diffract light with energies above the bandgap of the perovskite into the top cell under high angles and thus create light trapping of the reflected light in the perovskite top cell. At the same time, the spectral splitter metasurface reduces reflection in the infrared and therefore enhances photocurrent generation in the silicon bottom cell. We fabricate the metasurface spectrum splitter using SCIL and integrate it in a perovskite/silicon 4T tandem cell, and demonstrate a current increase in the top cell of 0.5 mA/cm^2. We predict an efficiency gain for the fabricated geometry in a wafer-sized 4T perovskite/silicon tandem solar cell of 0.26% (absolute). We present a further optimized metasurface design for which we predict a 1.4 mA/cm^2 enhancement in short-circuit current in the perovskite top cell and an efficiency enhancement of the 4T tandem solar cell of 0.40% (absolute). The metagrating geometry is very flexible in design and can be adjusted to other top and bottom cell bandgap combinations. The spectrum splitting metagratings present an optimized balance between spectral splitting, light trapping and optimized transmission in the infrared.

Overall, this thesis provides novel solutions based on nanophotonic light scattering to create colored PV and tandem solar cells with enhanced efficiency. It employs control over the scattering properties of resonant dielectric nanoscatterers and metasurfaces to create desired scattering distributions that are tailored in angular and spectral range. The metagrating concepts for photovoltaics developed in this thesis can be applied on a wide range of solar cells and can be scaled up to practical large-area fabrication technologies.

Samenvatting

Photovoltaica (PV) heeft het potentieel om één van de belangrijkste bronnen van energie te worden in een toekomst met een koolstofneutrale energievoorziening. Twee belangrijke aspecten om tot een grootschalige implementatie van PV in onze samenleving te komen zijn de naadloze integratie in gebouwen en infrastructuur en een verdere verhoging van het rendement van de fotovoltaïsche omzetting. Integratie van PV in onze omgeving vereist de ontwikkeling van zonnecellen met een kleurrijk uiterlijk. Een verhoging van het rendement van PV kan zorgen voor een verlaging van de kosten per opgewekt vermogen en van de benodigde oppervlakte voor de installatie van PV-systemen. Het bereiken van een hoog rendement vereist de ontwikkeling van tandemzonnecellen die uit meerdere materialen bestaan.

In dit proefschrift ontwikkelen we diëlektrische nanostructuren om een kleurrijk uiterlijk van zonnecellen op maat te creëren en laten we zien hoe vergelijkbare structuren het rendement in tandemcellen kunnen verhogen. Hiervoor ontwerpen we dunne lagen die bestaan uit diëlektrische nanodeeltjes die een sterke lichtverstrooiing vertonen in het zichtbare spectrum. We ontwikkelen diëlektrische metaoppervlakken en gecombineerde (gradiënt) metatralies die het mogelijk maken om het spectrum en de hoekverdeling van het verstrooide licht te controleren. In het eerste deel van het proefschrift presenteren we nieuwe manieren om de kleuring van PV te realiseren (Hoofdstuk 2-5), en ontwerpen we metaoppervlakken met op maat gemaakte spectrale en hoekverdeling van het licht (Hoofdstuk 4, 6). In het tweede deel van het proefschrift ontwikkelen we theoretisch en experimenteel metaoppervlakken-spectrale splitser om de prestaties van twee- en vier-terminale perovskiet/silicium tandemzonnecellen te verbeteren (Hoofdstuk 7, 8).

In Hoofdstuk 2 integreren we kristallijne Si-nanocilinderroosters (straal = 100-120 nm, hoogte = 240 nm, roosterconstante = 325 nm) in de voorste module laag van mini-silicium-PV-modules en demonstreren we een efficiënte kleuring van de modules. De karakteristieke Mie-resonanties van de nanocilinder in het zichtbaar spectrum veroorzaken een sterke (35-40%) reflectie rond een golflengte van λ = 540 nm en creëren een groene kleur van de module die slechts zwak afhankelijk is van de inkomende hoeken tussen 8-75°. De gekleurde module toont slechts een reductie van 10-11% in kortsluitstroom en omzettingsrendement. De hier gepresenteerde groene zonnemodules kunnen toepassingen vinden in verschillende soorten gebouw- en landschapsgeïntegreerde zonnepanelen. Voor de fabricage maken we gebruik van een substraat-conforme imprint lithografie (SCIL) nano-imprint techniek die toepasbaar is op zonnecel patronen met een groot oppervlak. (15 x 15 cm ^{2}).

Hoofdstuk 3 breidt de technologie van Hoofdstuk 2 uit tot een breder kleurspectrum. Door het veranderen van de grootte en de verdeling van de verstrooiende nanocilinders (straal = 50-150 nm, roosterconstante = 160-300 nm) controleren we de interferentie van elektrische en magnetische dipolen om resonerende verstrooiing te creëren over een

specifieke spectrale band. Zuivere kleuren van blauw tot rood kunnen worden gecreëerd met een verstrooiingsefficiëntie tot 75%. De techniek wordt uitgebreid door het creëren van gemengde kleuren (bijv. wit) door gecombineerde pixels van nanocilinderroosters. We maken een witte zonnemodule die een stroomverlies van slechts 19% laat zien, omdat alleen licht in een welgedefinieerde zichtbare spectrale band wordt gereflecteerd. De route van het combineren van verschillend gestructureerde metaoppervlak-pixels toont een grote flexibiliteit in het creëren van kleuren naar keuze en demonstreert het grote potentieel voor deze techniek om op grote schaal te worden toegepast.

In Hoofdstuk 4 demonstreren we metaoppervlakken die bestaan uit gecombineerde metaoppervlakken met op maat gemaakte hoekverstrooiingsprofielen van Si Mie-resonatoren. We controleren de spectrale respons door de interferentie van de modi van de nanodeeltjes op maat te maken en ze te rangschikken in patches met verschillende periodiciteit om de richtingsgevoeligheid van de verstrooiing over diffractieorders te controleren. Gebaseerd op een theoretisch dipoolverstrooiingsmodel, hebben we deze ultradunne oppervlakken (hoogte = 185 nm) ontworpen om wijdhoekige (35-75$^c irc$) en Lambertiaanse (0-75$^c irc$) verstrooiingsprofielen te realiseren bij een resonante golflengte (λ = 650 nm). Directe reflectie wordt tenietgedaan door destructieve interferentie van de verstrooiing van de deeltjes en reflectie van het substraat, en hoge-orde diffractie modi worden sterk onderdrukt door het controleren van de verstrooiing van een eenheidscel met verschillende nanodeeltjes. Experimenteel zijn de metaoppervlakken samengesteld uit Si nanobalken op een Ag spiegel die beschermd wordt door een dunne diëlektrische laag, en bereiken ze een verstrooiingsefficiëntie van 73-84%. De ultradunne resonerende metagratings creëren effectief de functionaliteit van "nanogestructureerde verf", die toepassingen kan vinden in de PV industrie met een gekleurd uiterlijk en hoekverdeling naar keuze, zoals aangetoond in Hoofdstuk 5. Op dezelfde manier kunnen de gepresenteerde metaoppervlakken dienen als spectrum-splitsende architecturen in tandemzonnecellen zoals beschreven in Hoofdstuk 7 en 8.

Hoofdstuk 5 is het vervolg van Hoofdstuk 4 waarin we spectrale en hoekverdelingscontrole van verstrooid licht experimenteel demonstreren met behulp van gecombineerde resonante metagratings die alleen voor bepaalde hoeken lichtverstrooiing creëren. Door de interferentie tussen de lichtverstrooiingsmodi van de nanodeeltjes op maat te maken, controleren we het verstrooiingsspectrum, en door ze te rangschikken in gebieden met verschillende roosterconstanten, controleren we de gerichtheid. Silicium nanobalken zijn gefabriceerd op een transparant substraat en resonantie treedt op bij λ = 650 nm. De nanobalken werden geplaatst in een supercelstructuur die bestaat uit meerdere roosters met verschillende roosterconstanten (675-1300 nm), waardoor een brede hoekverstrooiing ontstaat over 30-75$^c irc$. De metagratings zijn ontworpen om directe reflectie te onderdrukken en voor een efficiënte transmissie buiten de resonante verstrooiingsband. De metagratings zijn geïntegreerd met een silicium heterojunctie zonnecel waardoor een helderroodverstrooiend beeld ontstaat onder een beperkt aantal hoeken. Het externe quantumrendement is alleen gereduceerd in de verstrooiingsband, met een kortsluitstroomdaling van slechts 13%. Deze structuur kan worden toegepast in PV op daken en andere gebouwen met geïntegreerde PV die profiteren van lichtreflectie in de richting van een welgedefinieerd hoekbereik.

Hoofdstuk 6 toont de theorie, het ontwerp en de experimentele realisatie van een

breedbandig terugverstrooiend metaoppervlak op basis van het Huygens-Fresnel principe. Met behulp van een fase-gradiënt benadering ontwerpen we een theoretisch metaoppervlak met volledige terugverstrooiing. Door het creëren van een periodieke faseverandering van het licht dat gereflecteerd wordt van het oppervlak, wordt het licht efficiënt gekanaliseerd naar de eerste negatieve diffractieorde over een breed hoekbereik en over de bandbreedte in het zichtbare spectrum. In de experimentele realisatie wordt de berekende fasegradiënt gediscretiseerd en worden roosters gevormd door eenheidscellen van TiO_2 nanobalken van verschillende hoogte, die zijn geplaatst op een dunne zilver spiegel. Dit metaoppervlak maakt terugkaatsing mogelijk voor een breed scala van golflengten van λ = 490 - 940 nm met een rendement boven 85%. De voordelen van het ontwerp liggen in het lage profiel, de eenvoud van het ontwerp, de brede bandbreedte en de brede acceptatiehoek. De ultradunne metagratings kunnen de conventionele meer volumineuze terugverstrooiers vervangen en worden toegepast in diverse optische technologieën.

In Hoofdstuk 7 bestuderen we theoretisch de voordelen van een spectrale splitser die is geïntegreerd in een perovskiet/silicium twee-klems (2K) tandemzonnecel. De spectrale splitser reflecteert licht met energie boven de bandkloofenergie van de bovenste cel en verbetert daardoor de absorptie in het perovskiet om te profiteren van de hogere lichtspanning in de bovenste cel. We maken onderscheid tussen een vlakke en een Lambertiaanse verstrooiende spectrale splitser en vinden dat door de juiste splitsingsconditie te kiezen voor de sterkte en bandbreedte van de reflectie, beide spectrale splitserconfiguraties gunstig zijn voor 2K-tandemcellen. Voor topcelmaterialen met een bandkloof boven 1.7 eV is een spectrale splitser altijd gunstig omdat deze de absorptie in de topcel verbetert en zorgt voor een betere stroomafstemming met de bodemcel. Thermodynamische berekeningen tonen aan dat het opnemen van een Lambertiaanse spectralesplitsertussenlaag voor 500 nm dikke perovskiet-topcellen met een bandkloof hoger dan 1.7 eV leidt tot 5%-6% absolute rendementswinst. Met behulp van experimentele parameters van realistische cellen, voorspellen we een potentiële efficiëntiewinst van 2.8% (absoluut) voor een topcel met een bandkloofenergie van 1.77 eV.

In Hoofdstuk 8 demonstreren we experimenteel een spectrale splitser die tevens zorgt voor lichtopsluiting, als een tussenlaag in 4K perovskiet/siliciumtandemcellen. Dit metaoppervlak heeft de eigenschap om licht met energieën boven de bandkloof van het perovskiet onder hoge hoeken efficiënt te verstrooien in de topcel en zo het gereflecteerde licht in de perovskiet topcel op te vangen. Tegelijkertijd vermindert het spectrale-splitser metaoppervlak de weerkaatsing in het infrarood en verbetert daardoor de fotostroomgeneratie in de silicium bodemcel. We fabriceren de metaoppervlak-spectralesplitser met behulp van SCIL en integreren deze in een perovskiet/silicium 4K-tandemcel, en demonstreren een stroomtoename in de topcel van 0.5 mA/cm^2. We voorspellen een rendementsverhoging voor de gefabriceerde geometrie in een 4K perovskiet/silicium tandemzonnecel van 0.26% (absoluut). We presenteren een verder geoptimaliseerd metaoppervlak ontwerp waarvoor we een 1.4 mA/cm^2 verbetering in kortsluitstroom in de perovskiet topcel en een rendementsverhoging van de 4T-tandem zonnecel van 0.40% (absoluut) voorspellen. De metagrating geometrie is zeer flexibel van opzet en kan worden aangepast aan andere bandkloofcombinaties van de top- en bodemcel. De spectrumsplitser metaoppervlakken hebben een optimale balans tussen spectrale splitsing,

lichtopsluiting en geoptimaliseerde transmissie in het infrarood.

Samenvattend geeft dit proefschrift nieuwe oplossingen op basis van nanofotonische lichtverstrooiing om gekleurde PV- en tandemzonnecellen met een verbeterde efficiëntie te creëren. Het maakt gebruik van controle over de verstrooiingseigenschappen van resonerende diëlektrische nanoscillatoren en metaoppervlakken om de gewenste verstrooiingshoekverdeling te creëren die in een spectraal bereik op maat is gemaakt. De in dit proefschrift ontwikkelde metagrating concepten voor PV cellen kunnen worden toegepast op een breed scala aan zonnecellen en kunnen worden opgeschaald tot praktische technologieën voor de productie van grote oppervlakken.

Zusammenfassung

Photovoltaik (PV) hat das Potenzial eine der wichtigsten Energiequellen in einer CO_2 neutralen Zukunft zu werden. Zwei Schlüsselaspekte um eine großflächige Implementierung von PV in unserer Gesellschaft zu erreichen sind die nahtlose Integration in Gebäude und Infrastruktur, sowie eine weitere Steigerung des Wirkungsgrads von PV. Die Integration von PV in unsere Umgebung erfordert die Entwicklung von Solarzellen mit einem farbigen Erscheinungsbild. Eine Erhöhung des Wirkungsgrads der Solarzellen kann zudem eine Reduzierung der Kosten pro erzeugter Leistung sowie der geforderten Fläche für die Installation von PV-Systemen bewirken. Das Erreichen eines hohen Wirkungsgrades erfordert die Entwicklung von Tandem-Solarzellen, die aus mehreren Halbleiter-Schichten zusammengesetzt sind.

In dieser Dissertation entwickeln wir dielektrische Nanostrukturen, um ein maßgeschneidertes farbiges Erscheinungsbild von Solarzellen zu erzeugen und zeigen, wie ähnliche Strukturen den Wirkungsgrad in Tandem-Solarzellen erhöhen können. Dazu entwerfen wir Schichten aus dielektrischen Nanopartikeln, die eine starke Lichtstreuung im sichtbaren Spektralbereich aufweisen. Insbesondere entwickeln wir dielektrische Metaoberflächen und Metagratings, die eine Kontrolle des Spektrums und der Richtung des gestreuten Lichts ermöglichen. Im ersten Teil der Arbeit stellen wir neuartige Wege vor, um die Färbung von PV Zellen zu realisieren (Kapitel 2-5), und entwerfen Metaoberflächen mit maßgeschneiderter Spektrum- und Winkelkontrolle des Lichts (Kapitel 4, 6). Im zweiten Teil der Arbeit entwickeln wir theoretisch und experimentell Metaoberflächen-Spektrumsteiler zur Verbesserung der Leistung von zwei- und vierpoligen Perowskit/Silizium-Tandem-Solarzellen (Kapitel 7, 8).

In Kapitel 2 integrieren wir kristalline Si-Nanozylinder-Arrays (Radius = 100-120 nm, Höhe = 240 nm, Periode = 325 nm) in die vordere Modulschicht von Mini-Silizium-PV-Modulen und demonstrieren eine effiziente Einfärbung der Module. Die charakteristischen Mie-Resonanzen der Nanozylinder im sichtbaren Spektrum bewirken eine starke (35-40%) Lichtstreuung bei eine Wellenlänge von etwa λ = 540 nm und erzeugen eine Grünfärbung des Moduls, die über den Winkelbereich von 8-75° relativ unabhängig von den Einfallswinkeln ist. Das eingefärbte Modul zeigt lediglich eine Reduzierung des Kurzschlussstroms und des Wirkungsgrads um 10-11%. Die hier vorgestellten grünen Solarmodule können in der gebäude- und landschaftsintegrierten Photovoltaik verschiedenste Anwendungen finden. Für die Herstellung verwenden wir das Nano-Imprint-Verfahren Soft Imprint Conformal Lithography (SCIL), das für die vollflächige (15 x 15 cm^2) Strukturierung von Solarzellen geeignet ist.

In Kapitel 3 wird die Technik aus Kapitel 2 auf einen größeren Farbraum ausgeweitet. Durch Veränderung der Größe und der Verteilung der Nanozylinder (Radius = 50-150 nm, Periode = 160-300 nm) kann die Interferenz von elektrischen und magnetischen Dipolen so kontrolliert werden, dass resonante Streuung über ein bestimmtes Spektralband erzeugt wird. Reine Farben von Blau bis Rot können mit einer Streueffizienz

von bis zu 75% erzeugt werden. Die Technik wird durch die Erzeugung von Mischfarben (z.B. weiß) durch kombinierte Pixel von Nanozylinder-Arrays erweitert. Wir stellen ein weißes Solar-Minimodul her, das einen Stromverlust von nur 19% aufweist, da nur Licht in einem gut definierten sichtbaren Spektralband reflektiert wird. Die Kombination von unterschiedlichen Pixeln weißt eine große Flexibilität bei der Erzeugung von Farben nach Wahl auf und demonstriert das große Potenzial dieser Technik für eine breite Anwendung.

In Kapitel 4 demonstrieren wir Metaoberflächen, die aus kombinierten Metagratings aus Si-Mie-Resonatoren mit maßgeschneiderten Streuwinkel Profilen bestehen. Wir kontrollieren die Reflexion, indem wir die Interferenz der Streumoden der Nanopartikel anpassen und die Partikel in unterschiedlicher Periodizität anordnen, um die Winkel der Beugungsordnungen zu kontrollieren. Basierend auf einem theoretischen Dipol-Streumodell haben wir diese ultradünnen Oberflächen (Höhe = 185 nm) so gestaltet, dass sie bei Resonanz (λ = 650 nm) breitwinklige (35-75°) und Lambertsche großwinklige (0-75°) Streuprofile aufzeigen. Die spiegelnde Reflexion wird durch destruktive Interferenz zwischen der Streuung der Partikel und der Reflexion des Substrats aufgehoben, und die Beugungsmoden höherer Ordnung werden durch Einheitszellen mit mehreren Nanopartikeln stark unterdrückt. Experimentell bestehen die Metaoberflächen aus Si-Nanostäben auf einem Silberspiegel, der durch eine dünne dielektrische Schicht geschützt ist, und erreichen Streueffizienzen von 73-84%. Die ultradünnen resonanten Metagratings besitzen effektiv die Funktionalität einer "nanostrukturierten Farbe", die in der Photovoltaik mit farbigem Aussehen und wählbarem Winkelverhalten Anwendung finden kann, wie in Kapitel 5 gezeigt wird. In ähnlicher Weise können die vorgestellten Metaoberflächen als Spektrumsteiler in Tandemsolarzellen dienen, wie in Kapitel 7 und 8 beschrieben.

In Kapitel 5 knüpfen wir an Kapitel 4 an, indem wir die Kontrolle über Spektrum und Winkel des gestreuten Lichts experimentell demonstrieren. Hierfür kombinieren wir verschiedene Metagratings, um die Lichtstreuung nur für einen bestimmten Winkelbereich zu erzeugen. Indem wir die Interferenz zwischen den Lichtstreumoden der Nanopartikel steuern, kontrollieren wir das Streuspektrum, und indem wir sie in Arrays unterschiedlicher Periodizität anordnen, kontrollieren wir die Streuwinkel. Silizium-Nanodrähte wurden auf einem transparenten Substrat hergestellt und streuen Licht bei einer Resonanz von λ = 650 nm. Die Nanodrähte wurden in einer Superzellenstruktur platziert, die aus mehreren Gittern mit unterschiedlichen Abständen (675-1300 nm) besteht, wodurch eine breitwinklige Streuung im Winkelbereich von 30-75° entsteht. Die Metagratings sind so konzipiert, dass sie spiegelnde Reflexion unterdrücken und eine effiziente Transmission außerhalb des resonanten Streubandes aufweisen. Die Metagratings sind mit einer Silizium-Heterojunction-Solarzelle integriert, die in einem bestimmten Winkelbereich ein hellrotes Streuungsbild erzeugt. Die externe Quanteneffizienz ist nur im streuenden Spektralband reduziert, mit einem Kurzschlussstromabfall von nur 13%. Diese Struktur kann Anwendung in Aufdach-Photovoltaikanlagen und anderen gebäudeintegrierten PV finden, die von der Lichtreflexion in Richtung eines wohldefinierten Winkelbereichs profitieren.

Kapitel 6 zeigt die Theorie, das Design und die experimentelle Realisierung einer breitbandigen Rückreflektor-Metaoberfläche basierend auf dem Huygens-Fresnel-Prinzip.

Unter Verwendung eines Phasengradienten-Ansatzes entwerfen wir eine theoretische Metaoberfläche mit einer Effizienz von 100% für die Rückreflexion. Durch die Erzeugung einer periodischen Phasenänderung des von der Oberfläche reflektierten Lichts wird das Licht über einen breiten Winkelbereich und über eine Bandbreite im sichtbaren Spektralbereich effizient in die erste negative Beugungsordnung gelenkt. In der experimentellen Umsetzung wird der berechnete Phasengradient diskretisiert und Arrays aus Einheitszellen von TiO_2-Nanodrähten unterschiedlicher Höhe gebildet, die auf einem Silberspiegel platziert werden. Diese Metaoberfläche ermöglicht die Rückreflexion für einen breiten Wellenlängenbereich von λ = 490 - 940 nm mit einer Effizienz über 85%. Die Vorteile des Designs liegen in der geringen Höhe, der Einfachheit des Aufbaus, der großen Bandbreite und dem großen möglichen Winkelbereich. Die ultradünnen Metaoberflächen können sperrigere Rückreflektoren ersetzen und finden Anwendung in vielen optischen Technologien.

In Kapitel 7 untersuchen wir theoretisch die Vorteile eines Spektrumsteilers, der in eine 2-Terminal (2T) Perowskit/Silizium-Tandem-Solarzelle integriert ist. Der Spektrumsteiler reflektiert Licht mit einer Energie größer als die Bandlücke der Topzelle und erhöht somit die Absorption im Perowskit, um von dem höheren Spannungspotenzial in der Topzelle zu profitieren. Wir unterscheiden zwischen einem planaren und einem Lambertschen streuenden Spektrumsteiler und stellen fest, dass durch die Wahl der richtigen Bedingungen für die Stärke und den Spektralbereich beide Spektrumsteilerkonfigurationen zum Vorteil für 2T-Tandem-Solarzellen sind. Für Topzellen mit einer Bandlücke größer als 1,7 eV ist ein Spektrumsteiler immer von Vorteil, da er die Absorption in der Topzelle erhöht und eine bessere Stromanpassung mit der unteren Stromzelle schafft. Detailed-Balance Berechnungen zeigen, dass eine Lambertschen Spektrumsteiler-Zwischenschicht bei 500 nm dicken Perowskit-Topzellen mit einer Bandlücke von mehr als 1,7 eV zu einem absoluten Effizienzgewinn von 5%-6% führt. Unter Verwendung experimenteller Parameter realistischer Solarzellen sagen wir einen potenziellen Effizienzgewinn von 2,8% (absolut) für eine Topzelle mit einer Bandlückenenergie von 1,77 eV voraus.

In Kapitel 8 demonstrieren wir experimentell eine Metagrating-Zwischenschicht in 4T-Perowskit/Silizium-Tandemzellen, die das einfallende Spektrum teilt und in der Topzelle einfängt. Dieses Metagrating hat die Eigenschaft, Licht mit Energien oberhalb der Bandlücke des Perowskits unter hohen Winkeln effizient in die Topzelle zu beugen und somit das reflektierte Licht in der Perowskit-Topzelle einzufangen. Gleichzeitig reduziert die Spektrumsteiler-Metaoberfläche die Reflexion im Infraroten Spektalbereich und erhöht damit die Photostromerzeugung in der unteren Silizium-Solarzelle. Wir stellen den Spektrumsteiler mittels SCIL her, integrieren ihn in eine Perowskit/Silizium 4T-Tandemzelle und zeigen eine Stromerhöhung in der Topzelle von 0,5 mA/cm^2. Wir prognostizieren einen Wirkungsgradgewinn für die hergestellte Struktur in einer 4T-Perowskit/Silizium-Tandemsolarzelle in Wafergröße von 0,26% (absolut). Wir stellen ein weiteres optimiertes Metasurface-Design vor, für das wir eine Erhöhung des Kurzschlussstroms in der Perowskit-Topzelle um 1,4 mA/cm^2 und eine Effizienzsteigerung der 4T-Tandemsolarzelle von 0,40% (absolut) vorhersagen. Die Metagrating-Geometrie ist sehr flexibel im Design und kann an andere Tandemsolarzellen-Kombinationen angepasst werden. Das spektrumsteilende Metagrating optimiert spektrale Aufspaltung und Lichteinfang im optischen Spektralbereich und Transmission im Infraroten Spektralbereich.

Insgesamt präsentier diese Arbeit neuartige Lösungen, die auf nanophotonischer Lichtstreuung basieren, um farbige PV- und Tandem-Solarzellen mit verbessertem Wirkungsgrad zu erzeugen. Die Kontrolle über die Streueigenschaften von resonanten dielektrischen Nanoteilchen und Metaoberflächen wird genutzt, um gewünschte Streuprofile zu erzeugen, mit maßgeschneidertem Winkel-Streuprofil und Spektrum. Die in dieser Arbeit entwickelten Metagrating-Konzepte für die Photovoltaik können auf eine breite Palette von Solarzellen angewendet werden und lassen sich auf praktische großflächige Fertigungstechnologien hochskalieren.

References

[1] Natural Resources Defense Council, *The road from Paris: The European Union's progress towards its climate pledge*, Tech. Rep. November (2017).

[2] A. Jäger-Waldau, I. Kougias, N. Taylor, and C. Thiel, *How photovoltaics can contribute to GHG emission reductions of 55% in the EU by 2030,* Renewable and Sustainable Energy Reviews **126**, 109836 (2020).

[3] A. Jäger-Waldau, *PV Status Report 2019*, Tech. Rep. (Publications Office of the European Union, Luxembourg, 2019).

[4] Fraunhofer ISE, *Integrierte Photovoltaik - Flächen für die Energiewende*, Tech. Rep. (2020).

[5] Planbureau voor de Leefomgeving & DNV GL, *Het potentieel van zonnestroom in de gebouwde omgeving van Nederland*, Tech. Rep. (2014).

[6] J.-B. Eggers, M. Behnisch, J. Eisenlohr, H. Poglitsch, W.-F. Phung, M. Muenzinger, C. Ferrara, and T. Kuhn, *PV-Ausbauerfordernisse versus Gebäudepotenzial: Ergebnis einer gebäudescharfen Analyse für ganz Deutschland,* in *Proc. 35. PV-Symposium* (Bad Staffelstein, 2020) pp. 837–856.

[7] K. Yamamoto, K. Yoshikawa, H. Uzu, and D. Adachi, *High-efficiency heterojunction crystalline si solar cells,* Japanese Journal of Applied Physics **57**, 08RB20 (2018).

[8] A. Richter, M. Hermle, and S. W. Glunz, *Reassessment of the Limiting Efficiency for Crystalline Silicon Solar Cells,* IEEE Journal of Photovoltaics **3**, 1184 (2013).

[9] D. Crisp, A. Pathare, and R. C. Ewell, *The performance of gallium arsenide/germanium solar cells at the Martian surface,* Acta Astronautica **54**, 83 (2004).

[10] Oxford PV, *https://www.oxfordpv.com/news/oxford-pv-hits-new-world-record-solar-cell,* (2021).

[11] M. Jošt, L. Kegelmann, L. Korte, and S. Albrecht, *Monolithic Perovskite Tandem Solar Cells: A Review of the Present Status and Advanced Characterization Methods Toward 30% Efficiency,* Advanced Energy Materials **10**, 1904102 (2020).

[12] H. A. Atwater and A. Polman, *Plasmonics for improved photovoltaic devices.* Nature materials **9**, 205 (2010).

[13] A. Polman and H. A. Atwater, *Photonic design principles for ultrahigh-efficiency photovoltaics,* Nature Materials **11**, 174 (2012).

[14] P. Spinelli and A. Polman, *Light Trapping in Thin Crystalline Si Solar Cells Using Surface Mie Scatterers,* IEEE Journal of Photovoltaics **4**, 554 (2014).

[15] P. Spinelli, M. Verschuuren, and A. Polman, *Broadband omnidirectional antireflection coating based on subwavelength surface Mie resonators,* Nature Communications **3**, 692 (2012).

[16] J. Van De Groep, P. Spinelli, and A. Polman, *Single-Step Soft-Imprinted Large-Area Nanopatterned Antireflection Coating,* Nano Letters **15**, 4223 (2015).

[17] E. C. Garnett, B. Ehrler, A. Polman, and E. Alarcon-Llado, *Photonics for Photovoltaics: Advances and Opportunities,* ACS Photonics , 0 (2020).

[18] A. Schüler, C. Roecker, J.-L. Scartezzini, J. Boudaden, I. Videnovic, R.-C. Ho, and P. Oelhafen, *On the feasibility of colored glazed thermal solar collectors based on thin film interference filters,* Solar Energy Materials and Solar Cells **84**, 241 (2004).

[19] A. Schüler, J. Boudaden, P. Oelhafen, E. De Chambrier, C. Roecker, and J. L. Scartezzini, *Thin film multilayer design types for colored glazed thermal solar collectors,* Solar Energy Materials and Solar Cells **89**, 219 (2005).

[20] J. H. Selj, T. T. Mongstad, R. Søndenå, and E. S. Marstein, *Reduction of optical losses in colored solar cells with multilayer antireflection coatings,* Solar Energy Materials and Solar Cells **95**, 2576 (2011).

[21] M. Li, L. Zeng, Y. Chen, L. Zhuang, X. Wang, and H. Shen, *Realization of Colored Multicrystalline Silicon Solar Cells with SiO_2/SiN_x:H Double Layer Antireflection Coatings,* International Journal of Photoenergy **2013**, 1 (2013).

[22] G. Y. Yoo, J. S. Jeong, S. Lee, Y. Lee, H. C. Yoon, V. B. Chu, G. S. Park, Y. J. Hwang, W. Kim, B. K. Min, and Y. R. Do, *Multiple-Color-Generating Cu(In,Ga)(S,Se)$_2$ Thin-Film Solar Cells via Dichroic Film Incorporation for Power-Generating Window Applications,* ACS Applied Materials and Interfaces **9**, 14817 (2017).

[23] B. Bläsi, T. Kroyer, O. Höhn, M. Wiese, C. Ferrara, U. Eitner, and T. E. Kuhn, *Morpho Butterfly Inspired Coloured BIPV Modules,* in *Proc. 33rd EUPVSEC*, September (2017) pp. 2–6.

[24] V. Neder, S. L. Luxembourg, and A. Polman, *Efficient colored silicon solar modules using integrated resonant dielectric nanoscatterers,* Applied Physics Letters **111**, 073902 (2017).

[25] V. Neder, S. L. Luxembourg, and A. Polman, *Colored solar modules using integrated pixelated resonant dielectric nanoscatterer arrays,* in *Proc. 33rd European Photovoltaic Solar Energy Conference and Exhibition* (Amsterdam, 2017) pp. 34–37.

[26] F. Uleman, V. Neder, A. Cordaro, A. Alù, and A. Polman, *Resonant Metagratings for Spectral and Angular Control of Light for Colored Rooftop Photovoltaics,* ACS Applied Energy Materials **3**, 3150 (2020).

[27] G. Peharz, K. Berger, B. Kubicek, M. Aichinger, M. Grobbauer, J. Gratzer, W. Nemitz, B. Großschädl, C. Auer, C. Prietl, W. Waldhauser, and G. C. Eder, *Application of plasmonic coloring for making building integrated PV modules comprising of green solar cells,* Renewable Energy **109**, 542 (2017).

[28] J. Halme and P. Mäkinen, *Theoretical efficiency limits of ideal coloured opaque photovoltaics,* Energy and Environmental Science **12**, 1274 (2019).

[29] R. Santbergen, R. Mishima, T. Meguro, M. Hino, H. Uzu, J. Blanker, K. Yamamoto, and M. Zeman, *Minimizing optical losses in monolithic perovskite/c-Si tandem solar cells with a flat top cell,* Optics Express **24**, A1288 (2016).

[30] D. Zhang, M. Najafi, V. Zardetto, M. Dörenkämper, X. Zhou, S. Veenstra, L. J. Geerligs, T. Aernouts, and R. Andriessen, *High efficiency 4-terminal perovskite/c-Si tandem cells,* Solar Energy Materials and Solar Cells **188**, 1 (2018).

[31] D. A. Jacobs, M. Langenhorst, F. Sahli, B. S. Richards, T. P. White, C. Ballif, K. R. Catchpole, and U. W. Paetzold, *Light Management: A Key Concept in High-Efficiency Perovskite/Silicon Tandem Photovoltaics,* Journal of Physical Chemistry Letters **10**, 3159 (2019).

[32] H. Shen, D. Walter, Y. Wu, K. C. Fong, D. A. Jacobs, T. Duong, J. Peng, K. Weber, T. P. White, and K. R. Catchpole, *Monolithic Perovskite/Si Tandem Solar Cells: Pathways to Over 30% Efficiency,* Advanced Energy Materials **10**, 1902840 (2019).

[33] M. I. Hossain, N. Yumnam, W. Qarony, A. Salleo, V. Wagner, D. Knipp, and Y. H. Tsang, *Non-resonant metal-oxide metasurfaces for efficient perovskite solar cells,* Solar Energy **198**, 570 (2020).

[34] M. H. Elshorbagy, E. López-Fraguas, F. A. Chaudhry, J. M. Sánchez-Pena, R. Vergaz, and B. García-Cámara, *A monolithic nanostructured-perovskite/silicon tandem solar cell: feasibility of light management through geometry and materials selection,* Scientific Reports **10**, 1 (2020).

[35] F. Sahli, J. Werner, B. A. Kamino, M. Bräuninger, R. Monnard, B. Paviet-Salomon, L. Barraud, L. Ding, J. J. Diaz Leon, D. Sacchetto, G. Cattaneo, M. Despeisse, M. Boccard, S. Nicolay, Q. Jeangros, B. Niesen, and C. Ballif, *Fully textured monolithic perovskite/silicon tandem solar cells with 25.2% power conversion efficiency,* Nature Materials **17**, 820 (2018).

[36] J. Van De Groep, D. Gupta, M. A. Verschuuren, M. M. Wienk, R. A. Janssen, and A. Polman, *Large-area soft-imprinted nanowire networks as light trapping transparent conductors,* Scientific Reports **5**, 1 (2015).

[37] M. W. Knight, J. van de Groep, P. C. Bronsveld, W. C. Sinke, and A. Polman, *Soft imprinted Ag nanowire hybrid electrodes on silicon heterojunction solar cells,* Nano Energy **30**, 398 (2016).

[38] M. A. Verschuuren, M. Megens, Y. Ni, H. van Sprang, and A. Polman, *Large area nanoimprint by substrate conformal imprint lithography (SCIL),* Advanced Optical Technologies **6**, 243 (2017).

[39] L. E. Perret-Aebi, P. Heinstein, V. Chapuis, S. Pélisset, C. Roecker, A. Schüler, K. Lumsden, Y. Leterrier, J. L. Scartezzini, J.-A. Manson, and C. Ballif, *New challenges in solar architectural innovation,* in *Proc. Conf. Cleantech for sustainable buildings* (Lausanne, 2011) p. 761.

[40] J. Escarre, H.-Y. Li, L. Sansonnens, F. Galliano, G. Cattaneo, P. Heinstein, S. Nicolay, J. Bailat, S. Eberhard, C. Ballif, and L.-E. Perret-Aebi, *When PV modules are becoming real building elements: White solar module, a revolution for BIPV,* in *Proc. 2015 IEEE 42nd Photovoltaic Specialist Conference (PVSC)* (IEEE, 2015).

[41] J. van de Groep and A. Polman, *Designing dielectric resonators on substrates: Combining magnetic and electric resonances,* Optics Express **21**, 26285 (2013).

[42] R. Paniagua-Domínguez, Y. F. Yu, A. E. Miroshnichenko, L. A. Krivitsky, Y. H. Fu, V. Valuckas, L. Gonzaga, Y. T. Toh, A. Y. S. Kay, B. Luk'yanchuk, and A. I. Kuznetsov, *Generalized Brewster effect in dielectric metasurfaces,* Nature Communications **7**, 10362 (2016).

[43] E.-H. Cho, H.-S. Kim, B.-H. Cheong, P. Oleg, W. Xianyua, J.-S. Sohn, D.-J. Ma, H.-Y. Choi, N.-C. Park, and Y.-P. Park, *Two-dimensional photonic crystal color filter development,* Optics Express **17**, 8621 (2009).

[44] L. Cao, P. Fan, E. S. Barnard, A. M. Brown, and M. L. Brongersma, *Tuning the Color of Silicon Nanostructures,* Nano Letters **10**, 2649 (2010).

[45] S. Sun, Z. Zhou, C. Zhang, Y. Gao, Z. Duan, S. Xiao, and Q. Song, *All-Dielectric Full-Color Printing with TiO_2 Metasurfaces,* ACS Nano **11**, 4445 (2017).

[46] J. Proust, F. Bedu, B. Gallas, I. Ozerov, and N. Bonod, *All-Dielectric Colored Metasurfaces with Silicon Mie Resonators,* ACS Nano **10**, 7761 (2016).

[47] Y. Kanamori, T. Ozaki, and K. Hane, *Reflection color filters of the three primary colors with wide viewing angles using common-thickness silicon subwavelength gratings,* Optics Express **22**, 25663 (2014).

[48] M. L. Brongersma, Y. Cui, and S. Fan, *Light management for photovoltaics using high-index nanostructures,* Nature Materials **13**, 451 (2014).

[49] M. Verschuuren, *Substrate Conformal Imprint Lithography for Nanophotonic*, Phd thesis, Utrecht University (2010).

[50] A. I. Kuznetsov, A. E. Miroshnichenko, Y. H. Fu, J. Zhang, and B. Luk'yanchuk, *Magnetic light,* Scientific Reports **2**, 492 (2012).

[51] A. I. Kuznetsov, A. E. Miroshnichenko, M. L. Brongersma, Y. S. Kivshar, and B. Luk'yanchuk, *Optically resonant dielectric nanostructures,* Science **354**, aag2472 (2016).

[52] J. Henrie, S. Kellis, S. M. Schultz, and A. Hawkins, *Electronic color charts for dielectric films on silicon,* Optics Express **12**, 1464 (2004).

[53] P. Spinelli, B. Macco, M. a. Verschuuren, W. M. M. Kessels, and A. Polman, *Al_2O_3/TiO_2 nano-pattern antireflection coating with ultralow surface recombination,* Applied Physics Letters **102**, 233902 (2013).

[54] A. Majumder, *https://www.ics.uci.edu/˜majumder/vispercep/chap5notes.pdf,* (2017).

[55] O. Berger, D. Inns, and A. G. Aberle, *Commercial white paint as back surface reflector for thin-film solar cells,* Solar Energy Materials and Solar Cells **91**, 1215 (2007).

[56] M. Wang, X. Ye, X. Wan, Y. Liu, and X. Xie, *Brilliant white polystyrene microsphere film as a diffuse back reflector for solar cells,* Materials Letters **148**, 122 (2015).

[57] H. Cao, Y. G. Zhao, H. C. Ong, S. T. Ho, J. Y. Dai, J. Y. Wu, and R. P. H. Chang, *Ultraviolet lasing in resonators formed by scattering in semiconductor polycrystalline films,* Applied Physics Letters **73**, 3656 (1998).

[58] P. D. García, R. Sapienza, and C. López, *Photonic Glasses: A Step Beyond White Paint,* Advanced Materials **22**, 12 (2010).

[59] D. S. Wiersma, P. Bartolini, A. Lagendijk, and R. Righini, *Localization of light in a disordered medium,* Nature **390**, 671 (1997).

[60] T. Schwartz, G. Bartal, S. Fishman, and M. Segev, *Transport and Anderson localization in disordered two-dimensional photonic lattices,* Nature **446**, 52 (2007).

[61] J. M. Miranda-Muñoz, G. Lozano, and H. Míguez, *Design and Realization of a Novel Optically Disordered Material: A Demonstration of a Mie Glass,* Advanced Optical Materials **5**, 1700025 (2017).

[62] M. Moccia, S. Liu, R. Y. Wu, G. Castaldi, A. Andreone, T. J. Cui, and V. Galdi, *Coding Metasurfaces for Diffuse Scattering: Scaling Laws, Bounds, and Suboptimal Design,* Advanced Optical Materials **5**, 1700455 (2017).

[63] M. Moccia, C. Koral, G. P. Papari, S. Liu, L. Zhang, R. Y. Wu, G. Castaldi, T. J. Cui, V. Galdi, and A. Andreone, *Suboptimal Coding Metasurfaces for Terahertz Diffuse Scattering,* Scientific Reports **8**, 11908 (2018).

[64] K. Chen, Y. Feng, Z. Yang, L. Cui, J. Zhao, B. Zhu, and T. Jiang, *Geometric phase coded metasurface: from polarization dependent directive electromagnetic wave scattering to diffusion-like scattering,* Scientific Reports **6**, 35968 (2016).

[65] A. Pors and S. I. Bozhevolnyi, *Plasmonic metasurfaces for efficient phase control in reflection,* Optics Express **21**, 27438 (2013).

[66] H. Kwon, E. Arbabi, S. M. Kamali, M. Faraji-Dana, and A. Faraon, *Computational complex optical field imaging using a designed metasurface diffuser,* Optica **5**, 924 (2018).

[67] M. Jang, Y. Horie, A. Shibukawa, J. Brake, Y. Liu, S. M. Kamali, A. Arbabi, H. Ruan, A. Faraon, and C. Yang, *Wavefront shaping with disorder-engineered metasurfaces,* Nature Photonics **12**, 84 (2018).

[68] N. M. Estakhri and A. Alù, *Recent progress in gradient metasurfaces,* Journal of the Optical Society of America B **33**, A21 (2016).

[69] V. S. Asadchy, M. Albooyeh, S. N. Tcvetkova, A. Díaz-Rubio, Y. Ra'di, and S. A. Tretyakov, *Perfect control of reflection and refraction using spatially dispersive metasurfaces,* Physical Review B **94**, 075142 (2016).

[70] A. Epstein and G. V. Eleftheriades, *Huygens' metasurfaces via the equivalence principle: design and applications,* Journal of the Optical Society of America B **33**, A31 (2016).

[71] Y. Ra'di, D. L. Sounas, and A. Alù, *Metagratings: Beyond the Limits of Graded Metasurfaces for Wave Front Control,* Physical Review Letters **119**, 067404 (2017).

[72] A. Epstein and O. Rabinovich, *Unveiling the Properties of Metagratings via a Detailed Analytical Model for Synthesis and Analysis,* Physical Review Applied **8**, 054037 (2017).

[73] D. Sell, J. Yang, S. Doshay, R. Yang, and J. A. Fan, *Large-Angle, Multifunctional Metagratings Based on Freeform Multimode Geometries,* Nano Letters **17**, 3752 (2017).

[74] J. Yang, D. Sell, and J. A. Fan, *Freeform Metagratings Based on Complex Light Scattering Dynamics for Extreme, High Efficiency Beam Steering,* Annalen der Physik **530**, 1700302 (2018).

[75] O. Rabinovich and A. Epstein, *Analytical Design of Printed Circuit Board (PCB) Metagratings for Perfect Anomalous Reflection,* IEEE Transactions on Antennas and Propagation **66**, 4086 (2018).

[76] E. Khaidarov, H. Hao, R. Paniagua-Domínguez, Y. F. Yu, Y. H. Fu, V. Valuckas, S. L. K. Yap, Y. T. Toh, J. S. K. Ng, and A. I. Kuznetsov, *Asymmetric Nanoantennas for Ultrahigh Angle Broadband Visible Light Bending,* Nano Letters **17**, 6267 (2017).

[77] W. Liu and A. E. Miroshnichenko, *Beam Steering with Dielectric Metalattices,* ACS Photonics **5**, 1733 (2018).

[78] R. Paniagua-Domínguez, Y. F. Yu, E. Khaidarov, S. Choi, V. Leong, R. M. Bakker, X. Liang, Y. H. Fu, V. Valuckas, L. A. Krivitsky, and A. I. Kuznetsov, *A Metalens with a Near-Unity Numerical Aperture,* Nano Letters **18**, 2124 (2018).

[79] D. M. Callahan, J. N. Munday, and H. A. Atwater, *Solar Cell Light Trapping beyond the Ray Optic Limit,* Nano Letters **12**, 214 (2012).

[80] C. Balanis, *Antenna theory; analysis and design,* Vol. 72 (Wiley, 1984) pp. 989–990.

[81] P. Heinstein, C. Ballif, and L.-E. Perret-Aebi, *Building Integrated Photovoltaics (BIPV): Review, Potentials, Barriers and Myths,* Green **3**, 125 (2013).

[82] A. Soman and A. Antony, *Colored solar cells with spectrally selective photonic crystal reflectors for application in building integrated photovoltaics,* Solar Energy **181**, 1 (2019).

[83] C. Ji, Z. Zhang, T. Masuda, Y. Kudo, and L. J. Guo, *Vivid-colored silicon solar panels with high efficiency and non-iridescent appearance,* Nanoscale Horizons **4**, 874 (2019).

[84] S. Pélisset, M. Joly, V. Chapuis, A. Schueler, S. Mertin, V. Hody-Le Caër, C. Ballif, and L.-E. Perret-Aebi, *Efficiency of silicon thin-film photovoltaic modules with a front coloured glass,* Proceeding of the CISBAT International Conference 2011 , 37 (2011).

[85] E. Klampaftis, D. Ross, and B. S. Richards, *Color, graphic design and high efficiency for photovoltaic modules,* in *Proc. 2014 IEEE 40th Photovoltaic Specialist Conference (PVSC)* (IEEE, 2014) pp. 0025–0029.

[86] N. Jolissaint, R. Hanbali, J.-C. Hadorn, and A. Schüler, *Colored solar façades for buildings,* Energy Procedia **122**, 175 (2017).

[87] T. Masuda, Y. Kudo, and D. Banerjee, *Visually Attractive and High-Power-Retention Solar Modules by Coloring with Automotive Paints,* Coatings **8**, 282 (2018).

[88] M. Pilliod, C. Gougoussis, O. Lefevre, M. Laurin, and J. Liu, *Obscuring, color matching, and camouflaging solar panels,* U.S. Patent 0122973A1 (2018).

[89] K.-T. Lee, J.-Y. Jang, J. Zhang, S.-M. Yang, S. Park, and H. J. Park, *Highly Efficient Colored Perovskite Solar Cells Integrated with Ultrathin Subwavelength Plasmonic Nanoresonators.* Scientific reports **7**, 10640 (2017).

[90] Y. Zhang, S. Chen, D. Hu, Y. Xu, S. Wang, F. Qin, Y. Cao, B.-O. Guan, A. Miroshnichenko, M. Gu, and X. Li, *Coloring solar cells with simultaneously high efficiency by low-index dielectric nanoparticles,* Nano Energy **62**, 682 (2019).

[91] V. Neder, Y. Ra'di, A. Alù, and A. Polman, *Combined Metagratings for Efficient Broad-Angle Scattering Metasurface,* ACS Photonics **6**, 1010 (2019).

[92] E. Palik, *Handbook of Optical Constants of Solids* (Academic, New York, 1985).

[93] Lumerical Inc., *https://www.lumerical.com/products/,* .

[94] A. Taflove and S. C. Hagness, *Computational Electrodynamics: The Finite-Difference Time-Domain Method* (Artech House Publishers, 2005).

[95] H. Chalabi, Y. Ra'di, D. L. Sounas, and A. Alù, *Efficient anomalous reflection through near-field interactions in metasurfaces,* Physical Review B **96**, 075432 (2017).

[96] A. Cordaro, J. van de Groep, S. Raza, E. F. Pecora, F. Priolo, and M. L. Brongersma, *Antireflection High-Index Metasurfaces Combining Mie and Fabry-Pérot Resonances,* ACS Photonics **6**, 453 (2019).

[97] A. V. Kildishev, A. Boltasseva, and V. M. Shalaev, *From metamaterials to metadevices,* Nature Materials **11**, 917 (2012).

[98] D. Lin, P. Fan, E. Hasman, and M. L. Brongersma, *Dielectric gradient metasurface optical elements,* Science **345**, 298 (2014).

[99] N. Yu and F. Capasso, *Flat optics with designer metasurfaces,* Nature Materials **13**, 139 (2014).

[100] M. Khorasaninejad, W. T. Chen, R. C. Devlin, J. Oh, A. Y. Zhu, and F. Capasso, *Metalenses at visible wavelengths: Diffraction-limited focusing and subwavelength resolution imaging,* Science **352**, 1190 (2016).

[101] N. Yu, P. Genevet, M. A. Kats, F. Aieta, J.-P. Tetienne, F. Capasso, and Z. Gaburro, *Light Propagation with Phase Discontinuities: Generalized Laws of Reflection and Refraction,* Science **334**, 333 (2011).

[102] S. Sun, K. Y. Yang, C. M. Wang, T. K. Juan, W. T. Chen, C. Y. Liao, Q. He, S. Xiao, W. T. Kung, G. Y. Guo, L. Zhou, and D. P. Tsai, *High-efficiency broadband anomalous reflection by gradient meta-surfaces,* Nano Letters **12**, 6223 (2012).

[103] X. Ni, A. V. Kildishev, and V. M. Shalaev, *Metasurface holograms for visible light,* Nature Communications **4**, 1 (2013).

[104] G. Zheng, H. Mühlenbernd, M. Kenney, G. Li, T. Zentgraf, and S. Zhang, *Metasurface holograms reaching 80% efficiency,* Nature Nanotechnology **10**, 308 (2015).

[105] N. M. Estakhri and A. Alu, *Ultra-Thin Unidirectional Carpet Cloak and Wavefront Reconstruction With Graded Metasurfaces,* IEEE Antennas and Wireless Propagation Letters **13**, 1775 (2014).

[106] X. Ni, Z. J. Wong, M. Mrejen, Y. Wang, and X. Zhang, *An ultrathin invisibility skin cloak for visible light,* Science **349**, 1310 (2015).

[107] B. Orazbayev, N. Mohammadi Estakhri, M. Beruete, and A. Alù, *Terahertz carpet cloak based on a ring resonator metasurface,* Physical Review B **91**, 195444 (2015).

[108] C. Pfeiffer and A. Grbic, *Metamaterial Huygens' Surfaces: Tailoring Wave Fronts with Reflectionless Sheets,* Physical Review Letters **110**, 197401 (2013).

[109] N. Mohammadi Estakhri and A. Alù, *Manipulating optical reflections using engineered nanoscale metasurfaces,* Physical Review B **89**, 235419 (2014).

[110] Y. Hadad, D. L. Sounas, and A. Alu, *Space-time gradient metasurfaces,* Physical Review B **92**, 100304 (2015).

[111] Y. Shi and S. Fan, *Dynamic non-reciprocal meta-surfaces with arbitrary phase reconfigurability based on photonic transition in meta-atoms,* Applied Physics Letters **108**, 021110 (2016).

[112] Z. Wei, H. Li, C. Wu, Y. Cao, J. Ren, Z. Hang, H. Chen, D. Zhang, and C. T. Chan, *Anomalous reflection from hybrid metamaterial slab,* Optics Express **18**, 12119 (2010).

[113] X. Su, Z. Wei, C. Wu, Y. Long, and H. Li, *Negative reflection from metal/graphene plasmonic gratings,* Optics Letters **41**, 348 (2016).

[114] Z. L. Deng, S. Zhang, and G. P. Wang, *A facile grating approach towards broadband, wide-angle and high-efficiency holographic metasurfaces,* Nanoscale **8**, 1588 (2016).

[115] J. Du, Z. Lin, S. T. Chui, W. Lu, H. Li, A. Wu, Z. Sheng, J. Zi, X. Wang, S. Zou, and F. Gan, *Optical Beam Steering Based on the Symmetry of Resonant Modes of Nanoparticles,* Physical Review Letters **106**, 203903 (2011).

[116] C. Wu, N. Arju, G. Kelp, J. A. Fan, J. Dominguez, E. Gonzales, E. Tutuc, I. Brener, and G. Shvets, *Spectrally selective chiral silicon metasurfaces based on infrared Fano resonances,* Nature Communications **5**, 1 (2014).

[117] M. Rumpel, M. Moeller, C. Moormann, T. Graf, and M. A. Ahmed, *Broadband pulse compression gratings with measured 99.7% diffraction efficiency,* Optics Letters **39**, 323 (2014).

[118] N. Destouches, A. V. Tishchenko, J. C. Pommier, S. Reynaud, O. Parriaux, S. Tonchev, and M. A. Ahmed, *99% efficiency measured in the -1st order of a resonant grating,* Optics Express **13**, 3230 (2005).

[119] M. Flury, A. V. Tishchenko, and O. Parriaux, *The Leaky Mode Resonance Condition Ensures 100% Diffraction Efficiency of Mirror-Based Resonant Gratings,* Journal of Lightwave Technology **25**, 1870 (2007).

[120] S. Astilean, P. Lalanne, P. Chavel, E. Cambril, and H. Launois, *High-efficiency subwavelength diffractive element patterned in a high-refractive-index material for 633 nm,* Optics Letters **23**, 552 (1998).

[121] N. Mohammadi Estakhri and A. Alù, *Wave-front Transformation with Gradient Metasurfaces,* Physical Review X **6**, 041008 (2016).

[122] V. H. Rumsey, *Reaction Concept in Electromagnetic Theory,* Physics Review **94**, 1705 (1954).

[123] G. Whitman and F. Schwering, *Reciprocity identity for periodic surface scattering,* IEEE Transactions on Antennas and Propagation **27**, 252 (1979).

[124] J. Lloyd, *The Retroreflective Equipment Manufacturers Association,* Tech. Rep. (2008).

[125] Y. Yang, W. Wang, P. Moitra, I. I. Kravchenko, D. P. Briggs, and J. Valentine, *Dielectric meta-reflectarray for broadband linear polarization conversion and optical vortex generation,* Nano Letters **14**, 1394 (2014).

[126] E. Hasman, V. Kleiner, G. Biener, and A. Niv, *Polarization dependent focusing lens by use of quantized Pancharatnam-Berry phase diffractive optics,* Applied Physics Letters **82**, 328 (2003).

[127] Z. Li, E. Palacios, S. Butun, and K. Aydin, *Visible-frequency metasurfaces for broadband anomalous reflection and high-efficiency spectrum splitting,* Nano Letters **15**, 1615 (2015).

[128] F. Aieta, M. A. Kats, P. Genevet, R. Khorasaninejad, and F. Capasso, *Multiwavelength achromatic metasurfaces by dispersive phase compensation,* Science **347**, 202 (2015).

[129] Z.-L. Deng, S. Zhang, and G. P. Wang, *Wide-angled off-axis achromatic metasurfaces for visible light,* Optics Express **24**, 23118 (2016).

[130] C. Holloway, M. Mohamed, E. Kuester, and A. Dienstfrey, *Reflection and Transmission Properties of a Metafilm: With an Application to a Controllable Surface Composed of Resonant Particles,* IEEE Transactions on Electromagnetic Compatibility **47**, 853 (2005).

[131] I. H. Malitson, *Interspecimen Comparison of the Refractive Index of Fused Silica,* Journal of the Optical Society of America **55**, 1205 (1965).

[132] A. D. Rakić, A. B. Djurišić, J. M. Elazar, and M. L. Majewski, *Optical properties of metallic films for vertical-cavity optoelectronic devices,* Applied Optics **37**, 5271 (1998).

[133] International Renewable Energy Agency, *Renewable Energy Capacity Highlights*, Tech. Rep. (2020).

[134] International Renewable Energy Agency, *Global Energy Transformation. A Roadmap to 2050*, Tech. Rep. (2019).

[135] Fraunhofer ISE, *Photovoltaics Report*, Tech. Rep. (2012).

[136] A. Al-Ashouri, E. Köhnen, B. Li, A. Magomedov, H. Hempel, P. Caprioglio, J. A. Márquez, A. B. Morales Vilches, E. Kasparavicius, J. A. Smith, N. Phung, D. Menzel, M. Grischek, L. Kegelmann, D. Skroblin, C. Gollwitzer, T. Malinauskas, M. Jošt, G. Matič, B. Rech, R. Schlatmann, M. Topič, L. Korte, A. Abate, B. Stannowski, D. Neher, M. Stolterfoht, T. Unold, V. Getautis, and S. Albrecht, *Monolithic perovskite/silicon tandem solar cell with >29% efficiency by enhanced hole extraction,* Science **370**, 1300 (2020).

[137] K. Yoshikawa, H. Kawasaki, W. Yoshida, T. Irie, K. Konishi, K. Nakano, T. Uto, D. Adachi, M. Kanematsu, H. Uzu, and K. Yamamoto, *Silicon heterojunction solar cell with interdigitated back contacts for a photoconversion efficiency over 26%,* Nature Energy **2**, 17032 (2017).

[138] Q. Xu, Y. Zhao, and X. Zhang, *Light Management in Monolithic Perovskite/Silicon Tandem Solar Cells,* Solar RRL **4**, 1 (2020).

[139] D. T. Grant, K. R. Catchpole, K. J. Weber, and T. P. White, *Design guidelines for perovskite/silicon 2-terminal tandem solar cells: an optical study,* Optics Express **24**, A1454 (2016).

[140] A. Martins, B. H. V. Borges, J. Li, T. F. Krauss, and E. R. Martins, *Photonic Intermediate Structures for Perovskite/c-Silicon Four Terminal Tandem Solar Cells,* IEEE Journal of Photovoltaics **7**, 1190 (2017).

[141] L. Mazzarella, Y. H. Lin, S. Kirner, A. B. Morales-Vilches, L. Korte, S. Albrecht, E. Crossland, B. Stannowski, C. Case, H. J. Snaith, and R. Schlatmann, *Infrared Light Management Using a Nanocrystalline Silicon Oxide Interlayer in Monolithic Perovskite/Silicon Heterojunction Tandem Solar Cells with Efficiency above 25%,* Advanced Energy Materials **9**, 1 (2019).

[142] M. Chapa, M. F. Alexandre, M. J. Mendes, H. Águas, E. Fortunato, and R. Martins, *All-Thin-Film Perovskite/C-Si Four-Terminal Tandems: Interlayer and Intermediate Contacts Optimization,* ACS Applied Energy Materials **2**, 3979 (2019).

[143] M. Schultes, T. Helder, E. Ahlswede, M. F. Aygüler, P. Jackson, S. Paetel, J. A. Schwenzer, I. M. Hossain, U. W. Paetzold, and M. Powalla, *Sputtered Transparent Electrodes (IO:H and IZO) with Low Parasitic Near-Infrared Absorption for Perovskite-Cu(In,Ga)Se_2 Tandem Solar Cells,* ACS Applied Energy Materials **2**, 7823 (2019).

[144] M. Jošt, E. Köhnen, A. B. Morales-Vilches, B. Lipovšek, K. Jäger, B. Macco, A. Al-Ashouri, J. Krč, L. Korte, B. Rech, R. Schlatmann, M. Topič, B. Stannowski, and S. Albrecht, *Textured interfaces in monolithic perovskite/silicon tandem solar cells: Advanced light management for improved efficiency and energy yield,* Energy and Environmental Science **11**, 3511 (2018).

[145] N. N. Lal, T. P. White, and K. R. Catchpole, *Optics and light trapping for tandem solar cells on silicon,* IEEE Journal of Photovoltaics **4**, 1380 (2014).

[146] J. Werner, G. Nogay, F. Sahli, T. C.-J. Yang, M. Bräuninger, G. Christmann, A. Walter, B. A. Kamino, P. Fiala, P. Löper, S. Nicolay, Q. Jeangros, B. Niesen, and C. Ballif, *Complex Refractive Indices of Cesium–Formamidinium-Based Mixed-Halide Perovskites with Optical Band Gaps from 1.5 to 1.8 eV,* ACS Energy Letters **3**, 742 (2018).

[147] A. Hoffmann, U. W. Paetzold, C. Zhang, T. Merdzhanova, A. Lambertz, C. Ulbrich, K. Bittkau, and U. Rau, *Advancing tandem solar cells by spectrally selective multilayer intermediate reflectors,* Optics Express **22**, A1270 (2014).

[148] K. Bittkau, T. Kirchartz, and U. Rau, *Optical design of spectrally selective interlayers for perovskite/silicon heterojunction tandem solar cells,* Optics Express **26**, A750 (2018).

[149] P. G. O'Brien, A. Chutinan, K. Leong, N. P. Kherani, G. A. Ozin, and S. Zukotynski, *Photonic crystal intermediate reflectors for micromorph solar cells: a comparative study,* Optics Express **18**, 4478 (2010).

[150] P. G. O'Brien, Y. Yang, A. Chutinan, P. Mahtani, K. Leong, D. P. Puzzo, L. D. Bonifacio, C.-W. Lin, G. A. Ozin, and N. P. Kherani, *Selectively transparent and conducting photonic crystal solar spectrum splitters made of alternating sputtered indium-tin oxide and spin-coated silica nanoparticle layers for enhanced photovoltaics,* Solar Energy Materials and Solar Cells **102**, 173 (2012).

[151] J. Üpping, A. Bielawny, R. B. Wehrspohn, T. Beckers, R. Carius, U. Rau, S. Fahr, C. Rockstuhl, F. Lederer, M. Kroll, T. Pertsch, L. Steidl, and R. Zentel, *Three-dimensional photonic crystal intermediate reflectors for enhanced light-trapping in tandem solar cells,* Advanced Materials **23**, 3896 (2011).

[152] A. Bielawny, J. Üpping, P. T. Miclea, R. B. Wehrspohn, C. Rockstuhl, F. Lederer, M. Peters, L. Steidl, R. Zentel, S. M. Lee, M. Knez, A. Lambertz, and R. Carius, *3D photonic crystal intermediate reflector for micromorph thin-film tandem solar cell,* Physica Status Solidi (A) Applications and Materials Science **205**, 2796 (2008).

[153] S. Fahr, C. Rockstuhl, and F. Lederer, *Sandwiching intermediate reflectors in tandem solar cells for improved photon management,* Applied Physics Letters **101** (2012), 10.1063/1.4755873.

[154] J. Jia, L. C. Seitz, J. D. Benck, Y. Huo, Y. Chen, J. W. D. Ng, T. Bilir, J. S. Harris, and T. F. Jaramillo, *Solar water splitting by photovoltaic-electrolysis with a solar-to-hydrogen efficiency over 30%,* Nature Communications **7**, 1 (2016).

[155] M. G. Walter, E. L. Warren, J. R. McKone, S. W. Boettcher, Q. Mi, E. A. Santori, and N. S. Lewis, *Solar water splitting cells,* Chemical Reviews **110**, 6446 (2010).

[156] A. D. Vos, *Detailed balance limit of the efficiency of tandem solar cells,* Journal of Physics D: Applied Physics **13**, 839 (1980).

[157] S. Rühle, *The detailed balance limit of perovskite/silicon and perovskite/CdTe tandem solar cells,* physica status solidi (a) **214**, 1600955 (2017).

[158] M. A. Green, *Lambertian light trapping in textured solar cells and light-emitting diodes: Analytical solutions,* Progress in Photovoltaics: Research and Applications **10**, 235 (2002).

[159] M. A. Green, E. D. Dunlop, J. Hohl-Ebinger, M. Yoshita, N. Kopidakis, and X. Hao, *Solar cell efficiency tables (version 56),* Progress in Photovoltaics: Research and Applications **28**, 629 (2020).

[160] C. Ulbrich, C. Zahren, A. Gerber, B. Blank, T. Merdzhanova, A. Gordijn, and U. Rau, *Matching of Silicon Thin-Film Tandem Solar Cells for Maximum Power Output,* International Journal of Photoenergy **2013**, 1 (2013).

[161] Y. Yao, H. Liu, and W. Wu, *Spectrum splitting using multi-layer dielectric metasurfaces for efficient solar energy harvesting,* Applied Physics A: Materials Science and Processing **115**, 713 (2014).

[162] S. Kim, S. Kasashima, P. Sichanugrist, T. Kobayashi, T. Nakada, and M. Konagai, *Development of thin-film solar cells using solar spectrum splitting technique,* Solar Energy Materials and Solar Cells **119**, 214 (2013).

[163] R. Sheng, A. W. Y. Ho-Baillie, S. Huang, M. Keevers, X. Hao, L. Jiang, Y.-B. Cheng, and M. A. Green, *Four-Terminal Tandem Solar Cells Using $CH_3NH_3PbBr_3$ by Spectrum Splitting,* The Journal of Physical Chemistry Letters **6**, 3931 (2015).

[164] T. Kinoshita, K. Nonomura, N. Joong Jeon, F. Giordano, A. Abate, S. Uchida, T. Kubo, S. I. Seok, M. K. Nazeeruddin, A. Hagfeldt, M. Grätzel, and H. Segawa, *Spectral splitting photovoltaics using perovskite and wideband dye-sensitized solar cells,* Nature Communications **6**, 8834 (2015).

[165] Z. J. Yu, K. C. Fisher, B. M. Wheelwright, R. P. Angel, and Z. C. Holman, *PVMirror: A New Concept for Tandem Solar Cells and Hybrid Solar Converters,* IEEE Journal of Photovoltaics **5**, 1791 (2015).

[166] T. Duong, D. Grant, S. Rahman, A. Blakers, K. J. Weber, K. R. Catchpole, and T. P. White, *Filterless Spectral Splitting Perovskite–Silicon Tandem System With >23% Calculated Efficiency,* IEEE Journal of Photovoltaics **6**, 1432 (2016).

[167] M. H. Elshorbagy, B. García-Cámara, E. López-Fraguas, and R. Vergaz, *Efficient light management in a monolithic tandem perovskite/silicon solar cell by using a hybrid metasurface,* Nanomaterials **9**, 1 (2019).

[168] A. Mellor, N. P. Hylton, S. A. Maier, and N. Ekins-Daukes, *Interstitial light-trapping design for multi-junction solar cells,* Solar Energy Materials and Solar Cells **159**, 212 (2017).

[169] M. I. Hossain, W. Qarony, S. Ma, L. Zeng, D. Knipp, and Y. H. Tsang, *Perovskite/Silicon Tandem Solar Cells: From Detailed Balance Limit Calculations to Photon Management,* Nano-Micro Letters **11**, 1 (2019).

[170] V. Neder, S. W. Tabernig, and A. Polman, *Detailed-balance efficiency limits of two-terminal perovskite/silicon tandem solar cells with planar and Lambertian spectral splitters,* preprint at https://arxiv.org/abs/2012.12636 .

List of Publications

This thesis is based on the following publications

- *Efficient colored silicon solar modules using integrated resonant dielectric nanoscatterers*, V. Neder, S. L. Luxembourg, and A. Polman, Appl. Phys. Lett. **111**, 073902 (2017). (**Chapter 2**)
- *Colored solar modules using integrated pixelated resonant dielectric nanoscatterer arrays*, V. Neder, S. L. Luxembourg, and A. Polman, Proc. 33^{rd} European Photovoltaic Solar Energy Conference and Exhibition, 34-37 (2017). (**Chapter 3**)
- *Combined metagratings for efficient broad-angle scattering metasurface*, V. Neder, Y. Ra'di, A. Alù and A. Polman, ACS Photonics **6**, 1010–1017 (2019). (**Chapter 4**)
- *Resonant metagratings for spectral and angular control of light for colored rooftop photovoltaics*, F. Uleman,V. Neder, A. Cordaro, A. Alù, and A. Polman, ACS Applied Energy Materials **3**, 3150-3156 (2020). (**Chapter 5**)
- *Visible light, wide-angle graded metasurface for back reflection*, V. Neder, E. M. Estakhri, M. W. Knight, A. Polman, and A. Alù, ACS Photonics **4**, 228-235 (2017). (**Chapter 6**)
- *Detailed-balance efficiency limits of two-terminal perovskite/silicon tandem solar cells with planar and Lambertian spectral splitters*, V. Neder, S. W. Tabernig, and A. Polman, preprint at https://arxiv.org/abs/2012.12636 (2020). (**Chapter 7**)
- *Four-terminal perovskite/silicon tandem solar cell with integrated Mie-resonant spectral splitter metagrating*, V. Neder, S. D. Zhang, S. Veenstra, and A. Polman, preprint at https://arxiv.org/abs/2012.12649 (2020). (**Chapter 8**)

Other publications by the author

- *Broadband angular colour stability of dielectric-coated pyramidal textured Si for photovoltaics*, N. Roosloot, V. Neder, H. Haug, C. C. You, A. Polman, and E. S. Marstein, in preparation

Acknowledgements

Doing a PhD is the work of a single person officially, but it would never be possible without the support of colleagues and friends. During my PhD I met a lot of people that in different ways were very helpful, and that all contributed to this thesis, maybe without even being aware of it. Here I am trying to mention all of them:

First I want to say thank you to Albert, my supervisor and promoter. Albert, you have been more than a supervisor, you are a fantastic leader, a dedicated mentor and a good friend. The German term "Doktorvater" describes really well the role that you take for your PhD students. You care about good science, but even more about the well-being of the people that are in your group. Sometimes your enthusiasm can be overwhelming, but it is part of the PhD lesson to learn how to keep up with you (or sometimes how to slow you down). I learned a lot from you about science, presenting myself and taking control about my own projects (and life). I am very grateful for everything I have learned during those 4 years.

The PhD time would not have been the same without the great group that I was part of. Photonic materials is a collection of smart, modest and a little weird people and I feel that I could count on every single person in the present and the past constellation of the group. Thanks to all of you: Tom, for being the most reliable person I have ever met and all the useful advice you gave me. Nick, for showing to me what real passion for physics means and teaching me about Dutch subculture. Nika, for bringing an amazing happy atmosphere to the group, please keep your positive attitude! Matthias, for all the candies and fun talks in the office. Kelly, for being the most funny and unexpected office mate I could have hoped for. Stefan, we share a passion for solar cells and working and talking with you was always fun. Andrea, my dear friend, for sharing your genius ideas and all the fun we had in- and outside the lab. I am sure you will be a famous professor in no time. And finally Magda, for being a real friend, helping me through all the down phases during the PhD, cheering me up with cat stories, and bringing the sun to the office every morning. Without you, I am not sure if I would have managed. Floris, thanks for teaching me that every day is a good day. Joris, for all the interesting discussions about the good and bad in the world. Benjamin Brenny, for showing me what it actually means to be social. Jorik and Toon, thanks for sharing all your knowledge with me! Mark Knight, thanks for giving me my love for physics back, and showing me that I am actually good in it. And Sophie, I cannot describe in words how happy I am that our ways crossed at Amolf. You carry an endless source of energy in you, thanks for giving me part of it. Also thanks for all the great evenings we spent together in your cozy apartment, discussing about the world and watching Harry Potter.

There are more people that I met during my time at Amolf and that I would like to mention: To all group leaders of LMPV, Bruno, Esther and Erik, I enjoyed all discussions we had and all critical questions you asked. Femius and Said, thanks for always having an open office door, even for people that are not in your group. Thanks to the complete

nanophotonic community at Amolf, all poster sessions and nanocolloquiums really were a source of inspiration. Nasim T., talking to you is like a drug that I can't get enough of, luckily we did not share the office, otherwise we would never have finished our PhDs. Julia, thanks for being my running buddy and partner in crime if it comes to sustainability topics. Kevin, thanks for all the nice dinners we had and sharing your black humor with me. Annemarie, you are a fascinating person that always is good for a surprise. Moritz, thanks for your incredible kind personality and always having an open ear to my questions. Hugo, you are a great scientist, and I admire your work and of course your style. Sander, Amolf would not have been the same without meeting you, I am sure our ways will cross again. There are more great people that I met at Amolf and that I want to thank for the discussions, the fun, the lunch runs and all entertaining chats during the coffee breaks: Evelijn, Heleen, Marnix, Lucie, Loreta, Marloes, Isabelle, Susan, Hongyu, Harmen W., Hans H., Robin, Lukas H., Mark A., Jenny, Parisa, Giorgio, Ruslan, Harshal, Rene, Yorick B., Christian D., Agustin, Marko K. and Ruben from ARCNL.

It is always mentioned and it is really true, Amolf is a great place also because of all the great support that we have there. A big thank you goes to the cleanroom staff! Dimitry, Bob, Andries, Igor and Hans! Your never ending willingness to help and fix issues is what makes working in the nanolab fun! Especially, I want to thank Bob for all the deep conversations we had during endless waiting times in the cleanroom. Dimitry, master of SCIL and captain of the Voyager. Thanks for all the great help, fun talks and occasional shoulder claps if needed. Andries, I was very sad to see you leaving, and I learned a lot from you. A big thanks goes to Floortje, who organizes everything behind the scenes. And Dion, thanks for finding a solution to every technical problem and making my life so much easier. Thanks to Brahim from the Software development department for making Angie run. And also thanks to everybody from ICT! You are incredible helpful and fast, and it is great to be able to count on your support. In general, there are so many people at Amolf that deserve to be mentioned. A big thank you goes to all other support teams that I did not mention yet!

I was lucky to work with some great collaborators during the past years: Andrea Alù, your creativity and kindness is extremely motivating. Thanks for welcoming me in your group in Austin and being my second promoter. Younes, it probably was not always easy for you, but thanks to your patience I could find the theorist in me. Also thanks to Nasim M.E. and Hoyeong for working with me on the retroreflector projects. Thanks to Sjoerd Veenstra and Dong Zhang from Solliance, the spectrum splitter project was a dream of mine and I am very happy that we could realize it with your beautiful tandem cells.

Even though I spent most time during my PhD at Amolf, there are also people outside of Amolf that I want to mention. Andrea A., thanks for your open mind and making Amsterdam feeling like home from the beginning. Philip, Angeliki and Benjamin D., living with you in the first year of the PhD was an amazing experience and I miss these times a lot! Eva, danke dass du mich in eurer Wohnung aufgenommen hast und für den Sonnenschein den du in dir trägst! I am very happy to have found a very special group of friends in Utrecht that especially during the Corona times were a big support: Martina, danke für deine unkomplizietre Art, deine unbändige und ansteckende Energie und dein unendliches Biologie Wissen. Daniele, thanks that you never stop to ask questions. André, danke für die gelegentlichen Radtouren und Spaziergänge die meist

recht philosophisch wurden. Tjebbe, dankjewel dat je mij Nederlands hebt geleerd, mijn zwempartner was en voor het vaak babysitten. Je bent al geïntegreerd in onze familie. Friedi, Aland and Ava, danke für all die schönen Ausflüge gemeinsam und das gelegentliche Kinder-Tauschen. Ronja, mit dir wird die Welt einfach ein bisschen witziger und das ist sehr wertvoll. Leonie und Matthias, danke für die gemeinsamen Lindy hop Abende und all die leckeren Abendessen und Kuchenstunden die wir zusammen verbracht haben. I want to mention also one special friend that always made me believe in myself: Danke Ann-Sophie, dass du mir Mantra-ähnlich immer wieder sagst, dass ich gut und schlau und schön genug bin.

I want to thank my parents for their endless support: Mama, Papa, danke dass ihr mich meinen Weg habt gehen lassen und im Hintergrund immer für mich da wart. My sister and her family: Julia, ich kann mich immer auf dich verlassen, danke für die endlosen Telefonate und dass du immer an mich glaubst. And finally, a big thank you goes to my own family that grew by one (and soon two) members during my PhD time: Clara, du hast mir gezeigt was wirklich wichtig ist im Leben. David, du nimmst so viele Rollen ein in meinem Leben, als Partner, Vater meiner Tochter, Motivationstrainer, mein bester Freund und im letzten Jahr sogar als mein (Corona-) Kollege. Danke für deine unendliche Unterstützung, deine Ehrlichkeit und dass du dein Leben mit mir teilst.

About the author

Verena Neder was born in Schweinfurt, Germany, on April 16, 1991. She received her high school diploma in 2010 from the Jack-Steinberger Gymnasium in Bad Kissingen. She studied Physics at the Ruprecht-Karls University in Heidelberg and at the University of Amsterdam. She graduated in 2016 with cum laude, with a thesis on a gradient metasurface back reflector at AMOLF in Amsterdam under the supervision of prof. dr. Albert Polman. After her graduation she stayed at AMOLF and continued as a PhD student in the same group, working on dielectric metasurfaces for light management in photovoltaics. The results of her research are shown in this thesis. During her PhD in 2017 Verena spent one month at the University of Texas in Austin under the supervision of prof. dr. Andrea Alù, working on a Lambertian metagrating metasurface. In 2019 she went on a 4 month maternity leave after the birth of her daughter. In her free time Verena enjoys running, biking, gardening, cooking for friends and in a volunteer-run restaurant and inventing new activities with her family.